

UNCLASSIFIED

AD NUMBER	
AD610481	
CLASSIFICATION CHANGES	
TO:	unclassified
FROM:	confidential
LIMITATION CHANGES	
TO:	Approved for public release, distribution unlimited
FROM:	Distribution authorized to U.S. Gov't. agencies and their contractors; Administrative/Operational Use; 13 JUN 1958. Other requests shall be referred to HQ Field Command, Armed Forces Special Weapons Project, Albuquerque, NM.
AUTHORITY	
30 Jun 1970, DoDD 5200.10; AFSWP, per DTIC Form 55	

THIS PAGE IS UNCLASSIFIED

UNCLASSIFIED

WT-1111

This document consists of 171

No. 215 of 220 copies, Se

# Operation TEAPOT

NEVADA TEST SITE

February - May 1955

Project 1.12

DRAW-FORCE MEASUREMENTS

Issuance Date: June 13, 1958

Original Classification of this report is

**UNCLASSIFIED**

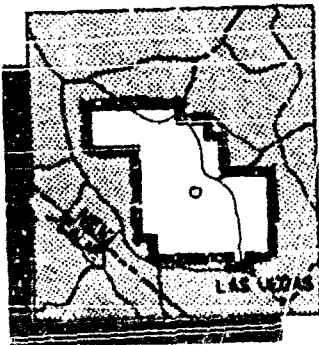
although the original classification may  
not have been removed from all pages.  
Classification changed by authority of  
TIA Change Notice No. 1182261

COPY

HARD COPY	\$ . 5.00
MICROFICHE	\$ . 1.00

**UNCLASSIFIED**

This material contains information affecting  
the national defense of the United States  
within the meaning of the espionage laws  
Title 18, U. S. C., Secs. 793 and 794, the  
transmission or revelation of which in any  
manner to an unauthorized person is pro-  
hibited by law.



HEADQUARTERS FIELD COMMAND, ARMED FORCES SPECIAL WEAPONS PROJECT  
SANDIA BASE, ALBUQUERQUE, NEW MEXICO

PROCESSING COPY  
ARCHIVE COPY

**UNCLASSIFIED**

**CONFIDENTIAL**

**Best  
Available  
Copy**

PAGES \_\_\_\_\_  
ARE  
MISSING  
IN  
ORIGINAL  
DOCUMENT

Inquiries relative to this report may be made to  
Chief, Armed Forces Special Weapons Project  
Washington, D. C.

When no longer required, this document may be  
destroyed in accordance with applicable security  
regulations.

**DO NOT RETURN THIS DOCUMENT**



# SUMMARY OF SHOT DATA, OPERATION TEAPOT

Shot	Code Name	Date	Time*	Area	Type	Latitude and Longitude of Zero Point
1	Wasp	18 February	1200	T-7-4†	762-ft Air	37° 05' 11.8856" N 116° 01' 18.7386" W
2	Moth	22 February	0545	T-3	300-ft Tower	37° 05' 52.2654" N 116° 01' 15.8967" W
3	Tesla	1 March	0530	T-9b	300-ft Tower	37° 07' 31.8737" N 116° 02' 51.0077" W
4	Turk	7 March	0520	T-2	500-ft Tower	37° 08' 18.4944" N 116° 07' 03.3678" W
5	Hornet	12 March	0520	T-3a	300-ft Tower	37° 02' 25.4043" N 116° 01' 31.3674" W
6	Bee	22 March	0505	T-7-1a	500-ft Tower	37° 05' 41.3880" N 116° 01' 25.5474" W
7	ESS	23 March	1230	T-10a	67-ft Underground	37° 10' 08.1263" N 116° 02' 37.7810" W
8	Apple	29 March	0455	T-4	500-ft Tower	37° 05' 43.8200" N 116° 06' 09.8040" W
9	Wasp†	29 March	1000	T-7-4‡	740-ft Air	37° 05' 11.8856" N 116° 01' 18.7386" W
10	HA	6 April	1000	T-5§	36,620-ft MSL Air	37° 01' 43.3642" N 116° 03' 28.2624" W
11	Post	9 April	0430	T-9c	300-ft Tower	37° 07' 19.8965" N 116° 02' 03.8860" W
12	MET	15 April	1115	FF	400-ft Tower	36° 47' 52.8887" N 115° 55' 44.1078" W
13	Apple 2	5 May	0510	T-1	500-ft Tower	36° 03' 11.1935" N 116° 06' 09.4837" W
14	Zucchini	15 May	0500	T-7-1a	500-ft Tower	37° 05' 41.3880" N 116° 01' 25.5474" W

\* Approximate local time, PST prior to 24 April, PDT after 24 April.

† Actual zero point 36 feet north, 426 feet west of T-7-4.

‡ Actual zero point 94 feet north, 62 feet west of T-7-4.

§ Actual zero point 36 feet south, 387 feet west of T-5.

## ABSTRACT

A three-component force gage suitable for measurement of transient aerodynamic drag loads on sting-mounted models was successfully developed and used on Shot 12 of Operation Teapot, using 3- and 10-inch-diameter spheres as models. Gages were positioned in three specially prepared areas: (1) a thermally absorbing, nondusty asphalt area; (2) a thermally reflecting, ideal water area; and (3) a thermally absorbing, dusty desert area. Comparison of peak forces at a 3-foot height over these surfaces indicated the highest forces in the dusty desert area, with lower forces in inconclusive order over the asphalt and water areas. These results compare favorably with the Ballistics Research Laboratory (BRL) drag-force measurements and vehicle-damage evaluation.

Due to the presence of dust and other inhomogeneities in the air stream and due to the fact that the gage readings depended upon the uncertain properties of the pressure seal between model shell and sting, it was not considered valid to calculate field drag coefficients from the force and  $q$  data. Further, the extreme variability of the laboratory drag measurements indicated that many more field readings would be required for a significant comparison of field and laboratory results. Therefore, the only comparisons of drag coefficients were made between laboratory results and previously published drag coefficients of spheres at high Reynolds numbers and subsonic and transonic Mach numbers.

Laboratory investigation revealed the high sensitivity of the sphere-sting configuration to angle of flow and, also, the difficulty of determining the actual angle of flow from the orthogonal force components. However, because the field forces recorded in the transverse (yaw) and vertical (pitch) directions were negligibly small and because dust scouring of the aluminum models was restricted to the front facing ground zero, it was concluded that on Shot 12 (at the 3-foot height) the air flow in the blast was parallel to the ground and directed radially outward from ground zero.

The spherical force gages were tested in wind tunnel and shock tubes in the range of Mach numbers from 0.2 to 0.7, with Reynolds numbers from about  $3 \times 10^5$  to  $3 \times 10^6$  (shock overpressures from about 2 to 20 psi). Fair agreement is obtained between wind-tunnel and shock-tube drag coefficients, although the considerable scatter of the laboratory results indicates the need for more extensive investigation.



## FOREWORD

This report presents the final results of one of the 56 projects comprising the Military Effects Program of Operation Teapot, which included 14 test detonations at the Nevada Test Site in 1955.

For overall Teapot military-effects information, the reader is referred to "Summary Report of the Technical Director, Military Effects Program," WT-1153, which includes the following: (1) a description of each detonation including yield, zero-point environment, type of device, ambient atmospheric conditions, etc.; (2) a discussion of project results; (3) a summary of the objectives and results of each project; and (4) a listing of project reports for the Military Effects Program.

## PREFACE

This report is presented in two parts, either of which may be read as an integral unit covering a particular phase of the NOL drag-force program. Part 1 describes the field phase of the Teapot Project 1.12 force program; the major objectives of the project, the field test design and results, and the significant conclusions of military interest are discussed in this part. Part 2 gives the details of the laboratory investigations conducted complementary to the field program; force-gage design and performance characteristics and wind-tunnel and shock-tube test conditions and data are included in this part.

Both parts of this report should be considered as "progress reports" in the field of drag studies. This initial attempt to study transient drag on scale models during full-scale tests necessitated a broad exploratory investigation for Operation Teapot. It led to the collection of a large volume of data, which at times is contradictory and contains wide scatter. With the experience gained during Operation Teapot as a guide, continuing work in this field can be conducted in a more directed and systematic way. Thus, in the light of the new data being obtained, the Teapot field and laboratory results are being reviewed continually and are being fitted into a more-comprehensible pattern. This information will be included in subsequent reports (such as that for Operation Redwing). However, no change in conclusions of military importance as presented in this report are anticipated.

The authors wish to express sincere appreciation to the operating personnel of the Armour Research Foundation 6-foot shock tube, the Ballistic Research Laboratories 24-inch shock tube, the David Taylor Model Basin 7-by-10-foot transonic wind tunnel, and the Naval Ordnance Laboratory 40-by-40 cm wind tunnel, who made their test facilities available and provided valuable technical assistance; to the members

CONFIDENTIAL

of the Explosives Research Department, the Aeroballistics Research Department, and Dr. G. K. Hartmann for help in planning this project at the Naval Ordnance Laboratory; and to L. W. Slifer, Jr., and J. F. Moulton, Jr., for their many contributions throughout the conduct of this investigation and for their critical examination of this final report.

Special appreciation is expressed to those others who served in the field operations at the Nevada Test Site for their whole-hearted cooperation in successfully completing the field experiments under adverse circumstances:

J. F. Moulton, Jr., Project Officer	
C. L. Karmel, Administration	
J. E. Berry, Group Leader	
E. E. Burk	S. Lechter
W. H. Hart	L. A. Lohr
R. A. Klaasse	L. W. Slifer, Jr.

During the field operations, the project was ably assisted by Maj. H. T. Bingham and CDR. W. M. McLellan, Directors of Programs 1 and 3, respectively, and by Lt. Col. J. J. Haley, Chief of the Field Requirements Branch. Dr. E. B. Doll, Technical Director of the Military Effects Group, provided general administrative and technical support.

This WT report also carries the Naval Ordnance Laboratory number NOIR 1219. ✓

# CONTENTS

ABSTRACT . . . . .	5
FOREWORD . . . . .	6
PREFACE . . . . .	6
 PART I FIELD TEST . . . . .	 15
CHAPTER 1 INTRODUCTION . . . . .	15
1.1 Objectives . . . . .	15
1.2 Background and Theory . . . . .	16
1.3 Operational Plan . . . . .	24
CHAPTER 2 INSTRUMENTATION AND FIELD LAYOUT . . . . .	26
2.1 Field Recording System . . . . .	26
2.2 Force Gages . . . . .	27
2.3 Field Layout . . . . .	30
CHAPTER 3 RESULTS . . . . .	35
3.1 General . . . . .	35
3.2 Interpretation of Force-Time Records . . . . .	38
3.3 Discussion of Force-Time Records . . . . .	39
3.3.1 Station D-1 . . . . .	39
3.3.2 Station D-2 . . . . .	40
3.3.3 Station D-3 . . . . .	40
3.3.4 Station A-1 . . . . .	48
3.3.5 Station A-2 . . . . .	48
3.3.6 Station W-1 . . . . .	48
3.4 Other Data . . . . .	48
3.4.1 Fitch, Yaw, and Effects of Nonhomogeneity of the Blast Medium . . . . .	48
3.4.2 Cylindrical Force Gage . . . . .	71
3.5 Drag Coefficients . . . . .	71
3.6 Summary of Results . . . . .	77
CHAPTER 4 CONCLUSIONS AND RECOMMENDATIONS . . . . .	79
4.1 Conclusions . . . . .	79
4.2 Recommendations . . . . .	80
 PART 2 LABORATORY INVESTIGATIONS . . . . .	 81
CHAPTER 5 INTRODUCTION . . . . .	81
5.1 Objectives . . . . .	81
5.2 Background . . . . .	81
5.3 Operational Plan . . . . .	82



2.3	Force Gage Layout for Shot 12 . . . . .	31
2.4	Typical Force Gage Station Layout. . . . .	32
2.5	Typical Field Installation of Spherical Force Gages. . . . .	33
2.6	Force Gages with Protective Covers . . . . .	33
2.7	Force Gages on Asphalt Line . . . . .	33
2.8	Field Installation of Cylinder Gage . . . . .	34
3.1	Post-Shot Condition of Spheres at 2,500-foot Desert Station . . . . .	36
3.2	Post-Shot Condition of Spheres at 3,000-foot Desert Station . . . . .	36
3.3	Post-Shot Condition of 3-inch Spheres at 4,500-foot Desert Station . . . . .	36
3.4	Post-Shot Condition of 10-inch Spheres at 4,500-foot Asphalt Station . . . . .	37
3.5	Post-Shot Condition of Spheres at 2,500-foot Asphalt Station . . . . .	37
3.6	Post-Shot Condition of Spheres at 3,000-foot Asphalt Station . . . . .	37
3.7	Post-Shot Condition of Spheres at 2,500-foot Water Station . . . . .	38
3.8	Force-Time Records in Z Direction for 2,500-foot Desert Station . . . . .	41
3.9	Force-Time Records in Z Direction for 3,000-foot Desert Station . . . . .	42
3.10	Force-Time Records in Z Direction for 4,500-foot Desert Station . . . . .	43
3.11	Force-Time Records in Z Direction for 4,500-foot Desert Station . . . . .	44
3.12	Force-Time Records in Z Direction for 2,500-foot Asphalt Station . . . . .	45
3.13	Force-Time Records in Z Direction for 3,000-foot Asphalt Station . . . . .	46
3.14	Force-Time Records in Z Direction for 2,500-foot Water Station . . . . .	47
3.15	Force-Time Records in Three Components for Gage D-1-P3 . . . . .	49
3.16	Force-Time Records in Three Components for Gage D-1-S3 . . . . .	50
3.17	Force-Time Records in Three Components for Gage D-1-P10 . . . . .	51
3.18	Force-Time Records in Two Components for Gage D-2-P3 . . . . .	52
3.19	Force-Time Records in Three Components for Gage D-2-S3 . . . . .	53
3.20	Force-Time Records in Three Components for Gage D-2-P10 . . . . .	54
3.21	Force-Time Records in Three Components for Gage D-3-P3 . . . . .	55
3.22	Force-Time Records in Three Components for Gage D-3-S3 . . . . .	56
3.23	Force-Time Records in Three Components for Gage D-3-P23 . . . . .	57
3.24	Force-Time Records in Three Components for Gage D-3-P10 . . . . .	58
3.25	Force-Time Records in Three Components for Gage D-3-P210 . . . . .	59
3.26	Force-Time Records in Three Components for Gage A-1-P3 . . . . .	60
3.27	Force-Time Records in Three Components for Gage A-1-S3 . . . . .	61
3.28	Force-Time Records in Two Components for Gage A-1-P10 . . . . .	62
3.29	Force-Time Records in Three Components for Gage A-2-P3 . . . . .	63
3.30	Force-Time Records in Three Components for Gage A-2-S3 . . . . .	64
3.31	Force-Time Records in Three Components for Gage A-2-P10 . . . . .	65

3.32	Force-Time Records in Two Components for Gage W-1-F3 . . . . .	64
3.33	Force-Time Records in Three Components for Gage W-1-S3 . . . . .	67
3.34	Force-Time Records in Three Components for Gage W-1-P10 . . . . .	68
3.35	Force-Time Records in Two Components for Cylinder Gage at 3,500-foot Desert Station . . . . .	69
3.36	Pressures, Forces, and Drag Coefficients at 2,500- foot Desert Station. . . . .	72
3.37	Pressures, Forces, and Drag Coefficients at 3,000- foot Desert Station. . . . .	72
3.38	Pressures, Forces, and Drag Coefficients at 4,500- foot Desert Station. . . . .	73
3.39	Pressures, Forces, and Drag Coefficients at 4,500- foot Desert Station. . . . .	73
3.40	Pressures, Forces, and Drag Coefficients at 2,500- foot Desert Station. . . . .	74
3.41	Pressures, Forces, and Drag Coefficients at 3,000- foot Asphalt Station . . . . .	74
3.42	Pressures, Forces, and Drag Coefficients at 2,500- foot Water Station . . . . .	75
3.43	Comparison of ERL with SRI Dynamic Pressure Records for Shot 12 . . . . .	77
6.1	Estimated Drag Coefficients of Spheres as Function of Mach Number and Reynolds Number. . . . .	86
6.2	Schematic Diagram of Three-Component Force Gage . . . . .	90
6.3	Prototype Model of Schaevitz Gage. . . . .	91
6.4	Convention for Direction of Force. . . . .	91
6.5	Three-inch and 10-inch Schaevitz Gages without Shells . . . . .	93
6.6	Ten-inch Schaevitz Gage with Spherical Shell . . . . .	93
6.7	Prototype Model of Bellows Gage . . . . .	93
6.8	Schematic Drawings of Bellows Gage and Diagram Gage . . . . .	94
6.9	Response of an Overdamped Schaevitz Gage to a Step Function (200 cps Timing). . . . .	96
6.10	Ten-inch Force Gage in Static Calibration Rig . . . . .	98
6.11	Quick-Release Device for Step-Function Test of Damping Characteristics of 3-inch Force Gages . . . . .	98
6.12	A Typical Static Calibration Curve . . . . .	99
6.13	Response of a Well-Damped Schaevitz Gage to a Step Function (200 cps Timing) . . . . .	99
6.14	The Force Gage in a Shock Wave . . . . .	100
6.15	Increase in Apparent Drag Coefficient Due to Effect of Static Pressure on a Perfectly Sealed Gage . . . . .	101
6.16	Mechanism for Applying Step-Function of Pressure to a Force Gage . . . . .	102
6.17	Response of a Well Sealed Gage to a Step Function of Pressure . . . . .	103
6.18	Response of a Poorly Sealed Gage to a Step Function of Pressure . . . . .	103
6.19	Response of Gage 11 to Step Function of Pressure . . . . .	104
6.20	Response of Gage 18 to Step Function of Pressure . . . . .	104
6.21	Response of Gage 10 to Step Function of Pressure . . . . .	105
6.22	Pressure Distribution on Spheres. . . . .	106

6.23	Pressure Inside Force Gages During DTMB Wind Tunnel Tests . . . . .	107	
7.1	Plan View of 3-inch Gage and Mount in BRL Shock Tube . . . . .	112	
7.2	Typical Pressure Records in BRL 24-inch Shock Tube . . . . .	112	
7.3	Force Records for Gages with High and Low Natural Frequencies in the BRL Shock Tube . . . . .	114	
7.4	Effect of Damping on Force Records of Gage 18 . . . . .	115	
7.5	Effect of Damping on Force Records of Gage 10 . . . . .	116	
7.6	Effect of Damping on Force Records of Gage 11 . . . . .	117	
7.7	Force Records for Sealed and Leaking Gages in BRL Shock Tube . . . . .	118	
7.8	Frequencies of Oscillation on Force Records, BRL Shock Tube . . . . .	120	
7.9	Drag Coefficients for Gage 18 in BRL Shock Tube . . . . .	121	
7.10	Drag Coefficients for Gage 11 in BRL Shock Tube . . . . .	122	
7.11	Drag Coefficients for Gage 10 in BRL Shock Tube . . . . .	123	
7.12	Effect of Leakage Area on $C_D$ -Time or $C_D$ - $F_S$ Curves . . . . .	125	
7.13	Summary of Initial Drag Coefficient in BRL Shock Tube . . . . .	125	
7.14	Pressure-Time Signatures in the ARF Shock Tube . . . . .	126	
7.15	NOL Recording Instrumentation, ARF Shock Tube Tests . . . . .	127	
7.16	Three-inch Force Gage and SRI q Gage in ARF Shock Tube . . . . .	128	
7.17	Ten-inch Force Gage in ARF Shock Tube . . . . .	128	
7.18	View of Gage Mount Anchored to Floor outside of ARF Shock Tube . . . . .	129	
7.19	Force Records from Gage 11 Before and After Shock Isolation of Gage Mount . . . . .	129	.....
7.20	Force Records from Gage 7 in ARF Shock Tube . . . . .	131	.....
7.21	Force Records from Gage 4 in ARF Shock Tube . . . . .	132	.....
7.22	Force Records from Gage 11 in ARF Shock Tube . . . . .	132	.....
7.23	P and q Records from SRI Gage in ARF Shock Tube . . . . .	133	.....
7.24	Frequencies of Oscillations on Force Records, ARF Shock Tube . . . . .	134	.....
7.25	Drag Coefficients in ARF Shock Tube . . . . .	134	.....
7.26	Comparison of Side-on Overpressures Recorded by Several Methods in ARF Shock Tube . . . . .	135	.....
7.27	Estimated Curves for Initial Drag Coefficients and Standard Deviation of the Data in ARF Shock Tube . . . . .	135	.....
7.28	Three-inch Force Gage in NOL 40-by-40-cm Wind Tunnel . . . . .	137	.....
7.29	Instrumentation for NOL Wind Tunnel Test . . . . .	137	
7.30	Tape Recordings of Force During Blow in NOL Wind Tunnel . . . . .	138	
7.31	Vibration of 3-inch Sphere in Steady Air Stream NOL Wind Tunnel . . . . .	139	
7.32	Comparison of SRI q Gage Readings with Wind Tunnel Instrumentation . . . . .	140	
7.33	Frequencies of Vibration on Drag Force Records, NOL Wind Tunnel . . . . .	141	
7.34	Amplitudes of Vibrations on Drag Force Records, NOL Wind Tunnel . . . . .	141	
7.35	Drag Coefficients in NOL Wind Tunnel . . . . .	142	

7.36	Three-inch Spherical Force Gage in DTMB 7-by-10-foot Transonic Wind Tunnel . . . . .	143
7.37	Ten-inch Spherical Force Gage in DTMB 7-by-10-foot Transonic Wind Tunnel . . . . .	143
7.38	Sand-Blasting of Shell of 3-inch Sphere Due to Dust in DTMB Transonic Wind Tunnel. . . . .	145
7.39	NOL Instrumentation, Force Gage Test at DTMB Transonic Wind Tunnel . . . . .	145
7.40	Vibrations of Spheres in Steady Flow at DTMB Transonic Wind Tunnel . . . . .	146
7.41	Frequencies of Vibrations on Drag Force Records, DTMB Transonic Wind Tunnel . . . . .	147
7.42	Amplitudes of Vibrations on Drag Force Records DTMB Transonic Wind Tunnel . . . . .	147
7.43	Drag Coefficients in DTMB 7-by-10-foot Transonic Wind Tunnel . . . . .	148
7.44	Relationships between $R$ and $P_g$ with Mach Number for Shock Tube and Wind Tunnel Flows . . . . .	152
7.45	Frequencies of Vibrations on Drag Force Records in Shock Tube and Wind Tunnel . . . . .	152
7.46	Comparison of Drag Coefficients Obtained in DTMB and NOL Wind Tunnels . . . . .	153
7.47	Comparison of Drag Coefficients Obtained in ARF and ERL Shock Tubes . . . . .	153
7.48	Comparison of Wind Tunnel and Shock Tube Drag Coefficients for Spheres . . . . .	154
A.1	Gage Locations on Structure 3.2t . . . . .	157
B.1	Idealized Loading History for Low-Frequency Structure . . . . .	161
B.2	Damped Single-Degree System Loaded by an Impulse and a Step Function ( $n/w = 0.6$ , $V_o/y_o = 3$ ) . . . . .	161
B.3	Response of a Damped Single-Degree-of-Freedom System to a step Function . . . . .	162
B.4	Maximum Amplitude of a Damped Single-Degree System Loaded by an Impulse and a Step Function . . . . .	163
B.5	Effect of Shock Overpressure on Relative Amplitude of Diffraction Spike and Drag Flat-Top . . . . .	164

#### TABLES

3.1	Summary of Force Data for Shot 12 . . . . .	40
3.2	Comparison of Peak Values of $q$ Measured by Several Agencies . . . . .	76
3.3	Comparison of Effects at Equal Range for Three Areas (3-foot height) . . . . .	78



# CONFIDENTIAL

## *Part 1 Field Test*

### Chapter 1 INTRODUCTION

#### 1.1 OBJECTIVES

The specific objectives for Project 1.12 on Operation Teapot were designed to fit within the framework of test conditions set up for Shot 12, (a 22-kt yield detonation fired on a 400 foot tower), while keeping in mind the wind-tunnel and shock-tube facilities available for laboratory experimentation. The project objectives were to:

1. Develop a three-component force gage suitable for measurement of transient loads on simple geometric bodies exposed to air flow in an atomic blast, shock tube, or wind tunnel.
2. Obtain drag force-time measurements on simple geometric targets exposed to atomic blast in three different areas---a thermally absorbing, nondusty asphalt area; a thermally-reflecting, clean, ideal water area; and a thermally-absorbing dusty desert area---these measurements to be compared one with the other to establish the significance of changes of ambient medium on force loading of structures.
3. Correlate the NOL-measured forces with the dynamic pressures (q) measured by the Stanford Research Institute (SRI) in order to obtain correct values of drag coefficient for specific geometric shapes in the three regions.
4. Conduct such shock-tube and wind-tunnel tests as may be necessary for correlation of laboratory forces and drag coefficients with those obtained in the field.
5. Reduce the force-component data to determine the direction of flow behind the shock front for the full duration of the blast.
6. Instrument a 6-by-6-by-12-foot reinforced-concrete structure (3.2 t) with 24 pressure-time gages distributed over the front, back, side, and top surfaces of the structure in order to assist Program 3.

Objective 1 was a necessary step toward the practical procurement of blast loading data. No suitable instrument existed prior to the Teapot program. Objective 2 was of prime immediate importance to the

cognizant military and civilian agencies for determining the significance of the precursor and associated phenomena as a force or damage-increasing mechanism. The third objective was of practical importance in reducing the basic field measurements to such nondimensional form as is customarily employed in aerodynamic nomenclature. This step was necessary if scientific correlation was to be attempted. Objective 4 was of theoretical and practical significance in understanding more fully the individual parameters that influence blast loading in the clean shock and complex precursor regions. Attainment of this fourth objective presumably would lead to the increased use of laboratory facilities as tools for the establishment of damage criteria, obviating the need for extensive full-scale tests. Objective 5, really an extension of Objective 2, was to provide information supplementary to the pitch and yaw measurements of the Sandia Corporation (Project 1.10), which information fits into the body of free-field data on the precursor phenomenon. The realization of Objective 6 was of importance to Program 3 for the determination of pressure distribution and consequent force loading of larger structures in the precursor region. In effect, this experiment was conducted so that the results could be compared with an identical experiment conducted on Operation Upshot-Knothole on the same structure. (The data obtained for this objective were analyzed by a Program 3 agency. See Appendix A for details of test conditions.)

## 1.2 BACKGROUND AND THEORY

During recent years there has existed considerable interest in the subject of air-blast loading of structures and the resulting response due to such transient loading. Much experimental and theoretical work has been done in this field, and considerable progress has been made in answering the military questions on structural damage due to air blast; but there remain many unsolved problems in prediction of the damaging effects of kiloton-range and multimegaton weapons, both from the standpoint of improvement of military estimates and from the standpoint of basic scientific knowledge. The scientific areas of interest include the details of transmission and propagation of the blast wave through the existing medium or media, the transient aerodynamic interaction between blast wave and structure, the behavior of the structure in response to the loading, and the modes of failure or collapse of the structure. Military requirements are less detailed and consist principally of the predictions of free-field phenomena (static pressure, temperature, etc.) and their correlation in terms of damage to structures.

Regardless of whether one has the military or the scientific outlook, the common simplifying step in handling the blast situation is to separate it into a blast-loading problem and a structural-response problem. This approach avoids the complications introduced by the variations in structural strength for similar external shapes. (Two structures may have equal surface areas and shapes and, therefore, almost identical loading histories, but their responses may be quite different due to different structural details.) In some cases this simplification cannot be justified, because of the interaction of air

**CONFIDENTIAL**

blast and target. For example, when windows and wall coverings are blown off early enough in the loading history, the loading on the remaining structural elements may change significantly. Also, there is still some question of whether the transient motion of the structural surface has an aerodynamic interaction with the blast (although preliminary investigation in wind tunnels and shock tubes does not indicate any change in loading due solely to vibratory motion of the target). However, in most cases, one may separate the loading and response problems for individual study.

Structural design is an old, well-established field. It has recently been extended by N. M. Newmark of the University of Illinois, and others, to include the effects of transient loads occasioned by nuclear detonations. The present state of the analytical techniques is such that, knowing the time history of the forces on the structure, one may predict response or failure with sufficient accuracy for military needs (References 1 to 3). For this reason, although research is continued on the modes of response and failure of structures, the present emphasis has been placed on improvement of estimates of the loading function.

Enough information has been accumulated through field tests, shock-tube studies, and wind-tunnel experiments to enable one to present a generalized picture of the loading for any structure. Without considering, for the moment, the characteristics of blast and target which may affect the loading pattern, the usual loading history (see Figure 1.1) may be described as consisting of three phases: (1) diffraction, (2) transition, and (3) pseudo-steady drag.

1. The diffraction phase of the loading history has been found experimentally to be of relatively short duration: of the order of two or three transit times (where the transit time is the time for the shock front to engulf the target). However, in spite of the short duration of the load, diffraction loading may be significant because of the extremely high amplitude of the forces (relatively). The pressures experienced on the surface of the target are initially equal to shock-wave-reflected pressure, which is at least double the side-on overpressure.

Consider a 6-foot-diameter smokestack being loaded (flow normal to axis of cylinder) by a clean shock (no inhomogeneities in the air) of 10 psi overpressure. For ambient conditions of 14.7 psi and 1,130 fps sound speed, ideal-shock-front velocity and reflected pressure are calculated as 1,420 fps and 25.3 psi, respectively. The load in the direction of the blast builds up from 0 to 21,800 pounds for each foot of stack height ( $25.3 \times 144 \times 6$ ) in about one-half transit time (transit time =  $6/1420 = 4.22$  msec) and decays within about three transit times (12.66 msec) to the relatively low load values of the transition phase indicated in Figure 1.1. (Note that these durations and peak loads are based on shock-tube studies on circular cylinders.)

2. The transition phase represents the period between the high load-diffraction phase and the low-amplitude drag phase. In the

transition zone, load is not proportional to the reflected pressure, nor is it proportional to the dynamic pressure of the drag phase. The duration of this period is the subject of some discussion (for example, see Reference 4) and may run from about 20 to more than 100 transit times.

3. During the pseudo-steady-drag period of the loading history, the blast wind (motion of the fluid particles behind the shock front)

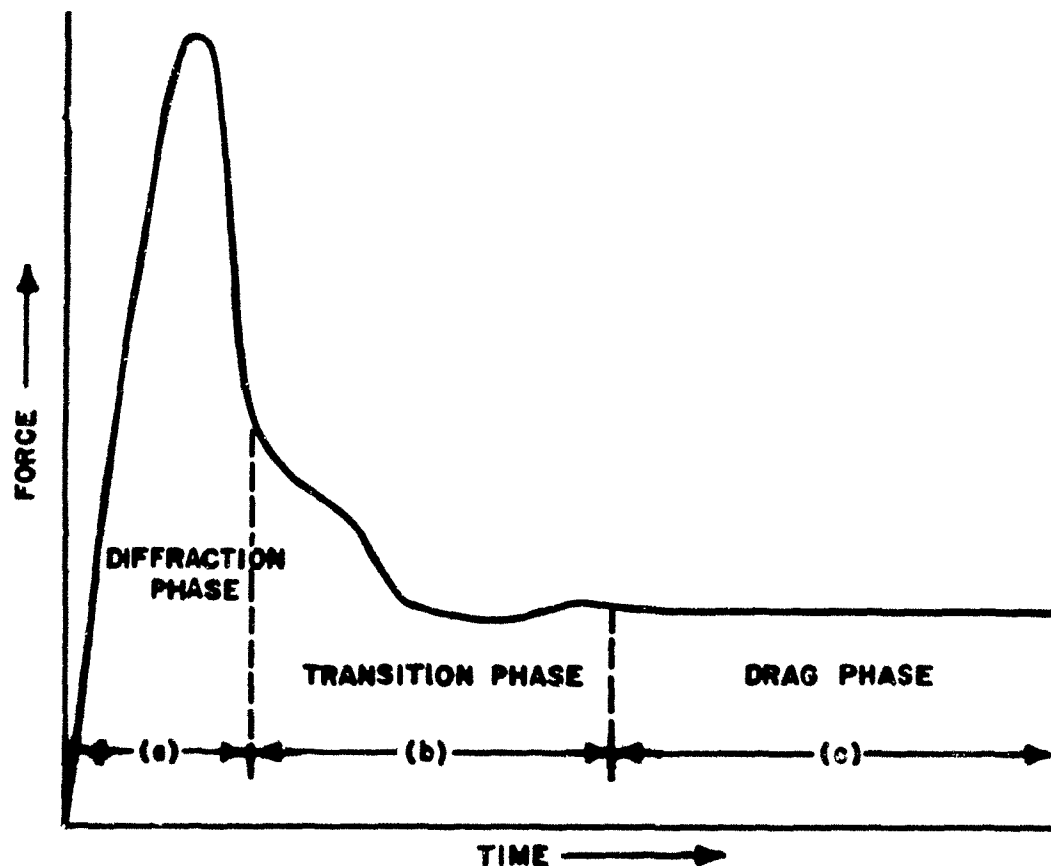


Figure 1.1 Loading History of a Structure.

is considered to have the same loading effect as the flow in a wind tunnel (force equal to the product of dynamic pressure, an empirically determined drag coefficient, and the projected area of the target). The "pseudo-steady" nomenclature is used because of the decaying nature of the blast wave, although the flow changes in the decaying wave are not fast enough to constitute a transient aerodynamic situation. (How gradual these flow changes must be to permit the pseudo-steady condition to obtain has not been established.) For those bodies (such as circular cylinders) which have irregular loading histories in a steady stream due to self-induced vortex effects, the criterion of steadiness is whether the fluctuations of load are periodic and

whether an average load can be determined easily by drawing a line through the oscillations.

For the example of the 6-foot-diameter smokestack considered above, the drag load would be 1,920 pounds per foot of stack height (dynamic pressure of 2.22 psi times drag coefficient assumed equal to  $1.0 \times 6 \text{ ft} \times 144$ ). Although the peak drag load is less than 10 percent of the peak diffraction load, the drag phase lasts for the remainder of the incident blast wave and can be of major structural significance.

To summarize the loading history of the 6-foot-diameter smokestack (Figure 1.1), the load builds up in about 2 msec to about 22,000 pounds per foot of stack height, drops rapidly (within about 13 msec) to some unsteady load in the neighborhood of 2,000 pounds per foot and then follows a slower and more steady decay rate in 100 to 400 msec, following the blast decay to zero in a second or two (depending on bomb size).

The question of which phase of the loading history has most significance depends on the structural and aerodynamic characteristics of the target. To illustrate, consider the same smokestack. It would be called a diffraction target if it failed within about 15 or 20 msec, since the major loading contribution would have come from the diffraction phase. If the stack collapsed after 100 or 200 msec, one would be compelled to consider it a drag target, since the effects of the diffraction phase were long past when failure occurred. Exactly when the stack collapses is mostly a function of the natural period of the stack in its mode of failure (including effects of plasticity, etc.). The natural period would have to be less than about 50 msec (20 cps nat. freq.) for the stack to be a diffraction target, and several hundred milliseconds (about 2 or 3 cps) for it to be a drag target. Since the natural period of a smokestack of 6-foot diameter depends on its height, its wall thickness, and its materials of construction, it is not justifiable to classify all 6-foot-diameter smoke stacks as either drag targets or diffraction targets.

Some generalizations may be made with respect to target classification, however, since most structures in common use have design features that are relatively fixed, depending upon the function of the structure. For example, structural materials are usually steel, concrete, or wood; the periods of most factory-type structures vary between 100 to 500 msec, etc. Based on such engineering experience, N. M. Newmark (Reference 5) has considered all factories to be diffraction targets if their window area is less than 20 percent of the wall frontal area and drag targets if the window area exceeds 60 percent. Bridges are conceded to be drag targets, since the diffraction phase for each individual beam and girder is of negligibly short duration. Aside from such few obvious cases which can be classified readily, there are many structural types of importance which cannot be distinctly categorized, and for this reason continued research efforts in all phases of blast loading are warranted.

To date, the greater part of the progress in understanding blast loading has been made on the diffraction phase of the loading,

000000 0000

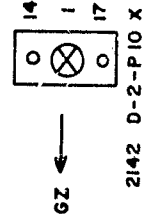
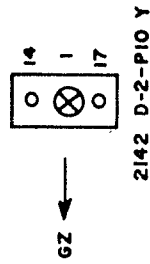
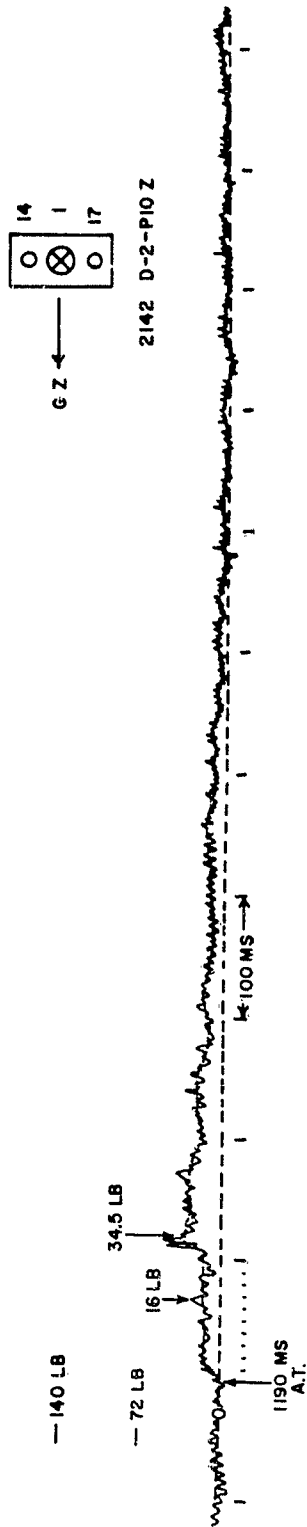


Figure 3.20 Force-Time Records in Three Components for  
Case D-2-F10.

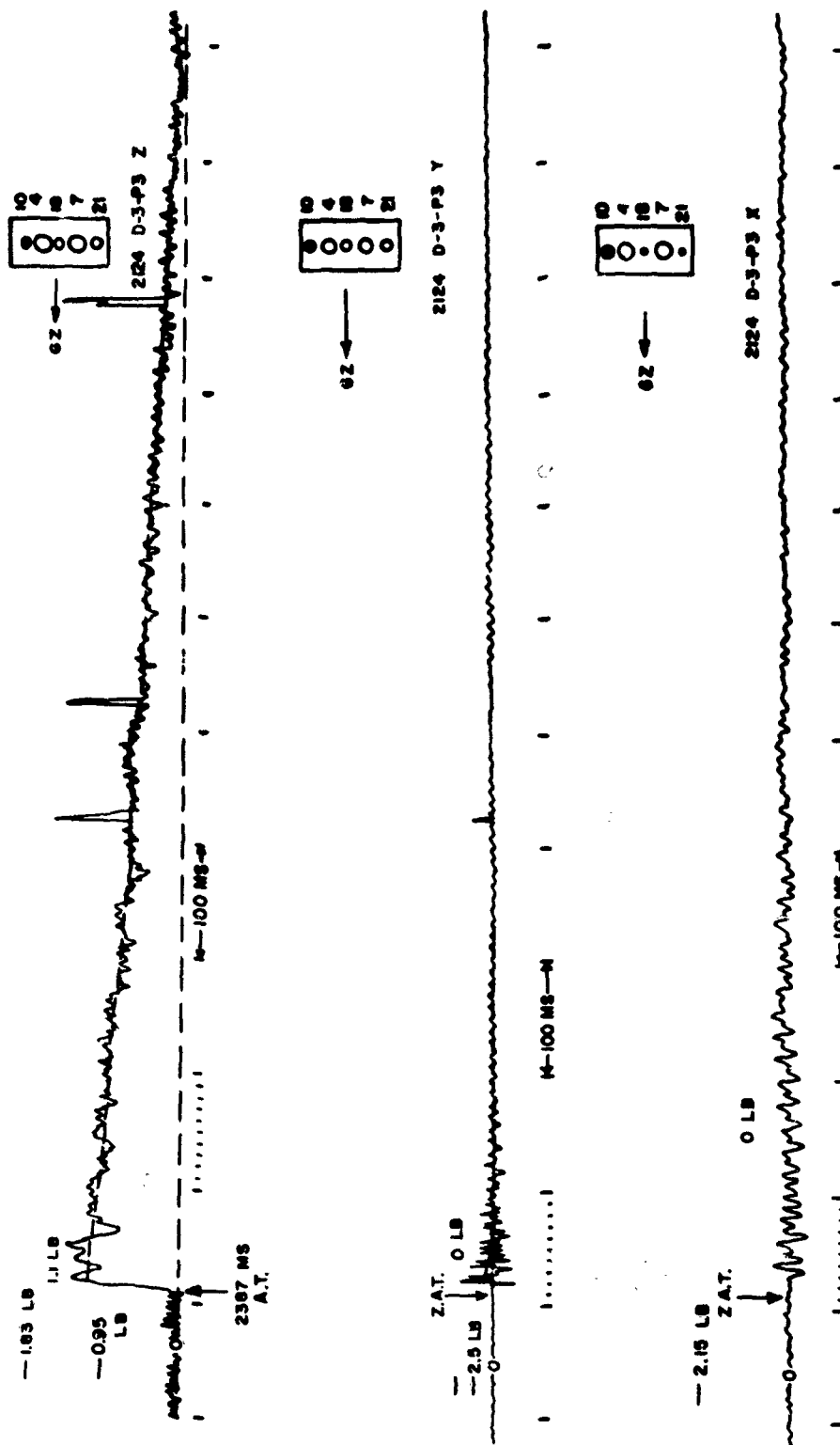


Figure 3.21 Force-Time Records in Three Components for Gage D-3-P3.

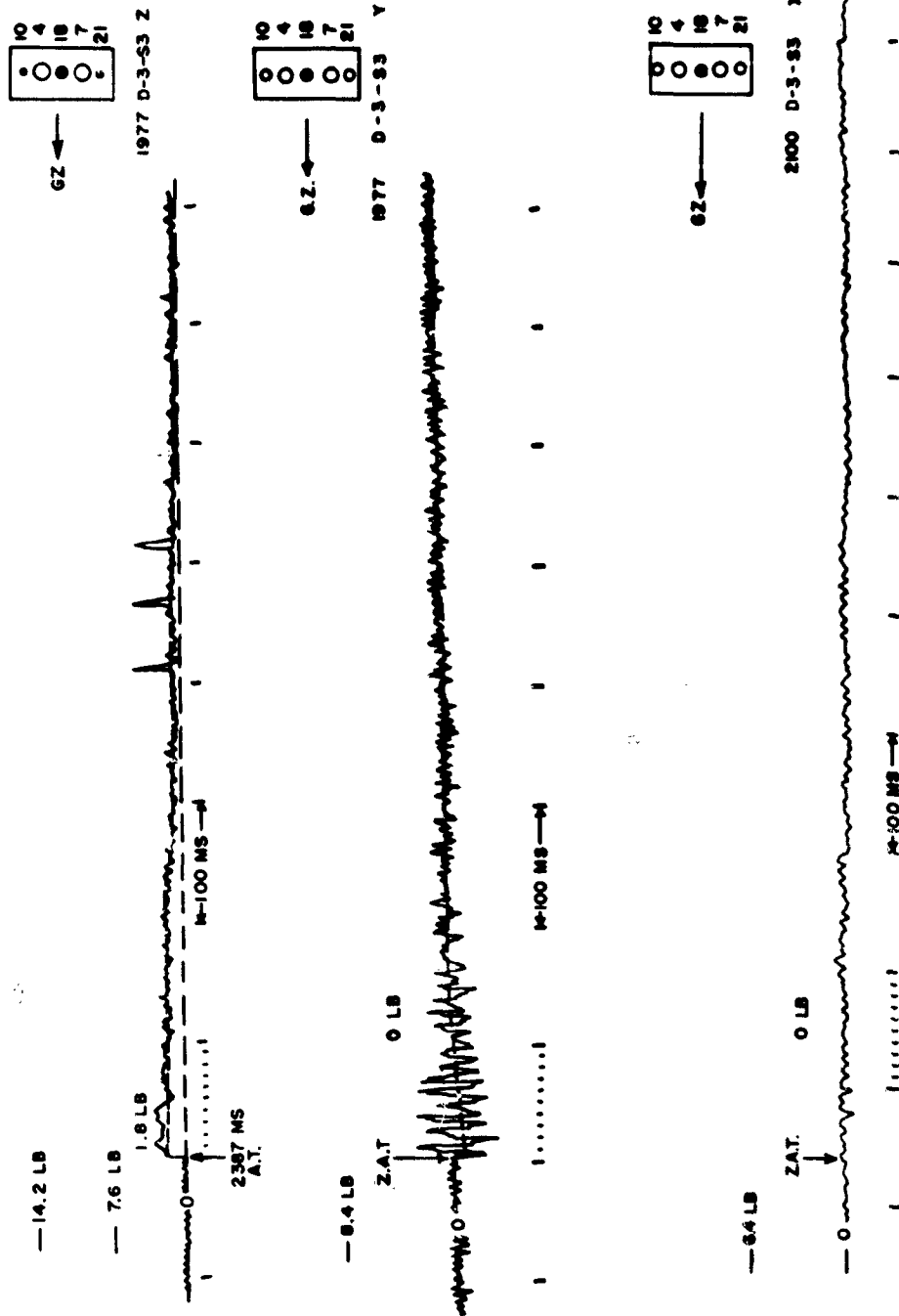


Figure 3.22 Force-Time Records in Three Components for  
Gage D-3-S3.



CONFIDENTIAL

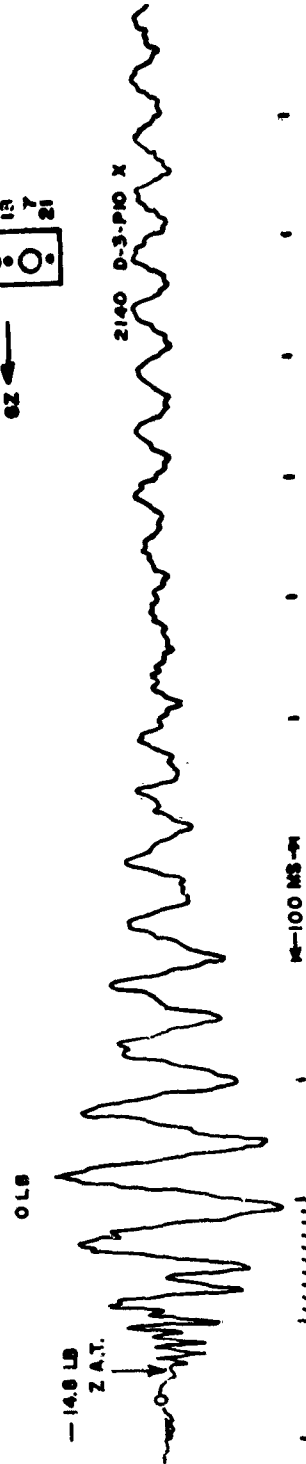
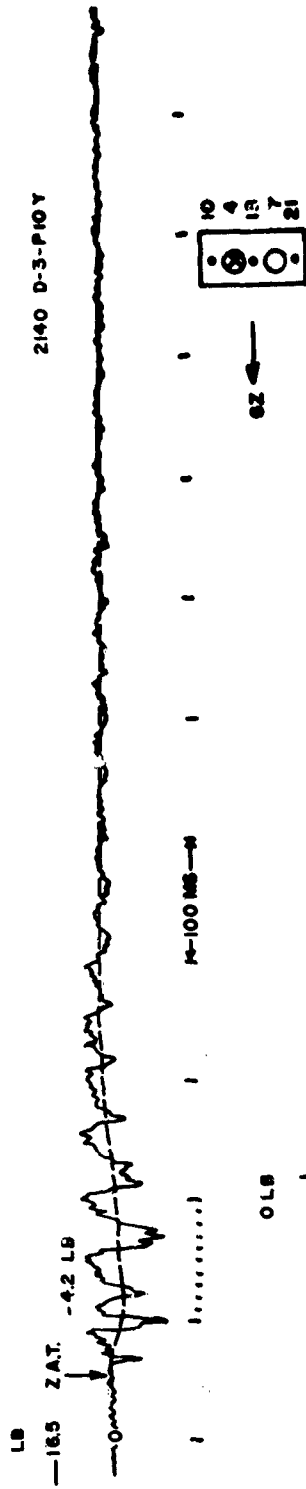
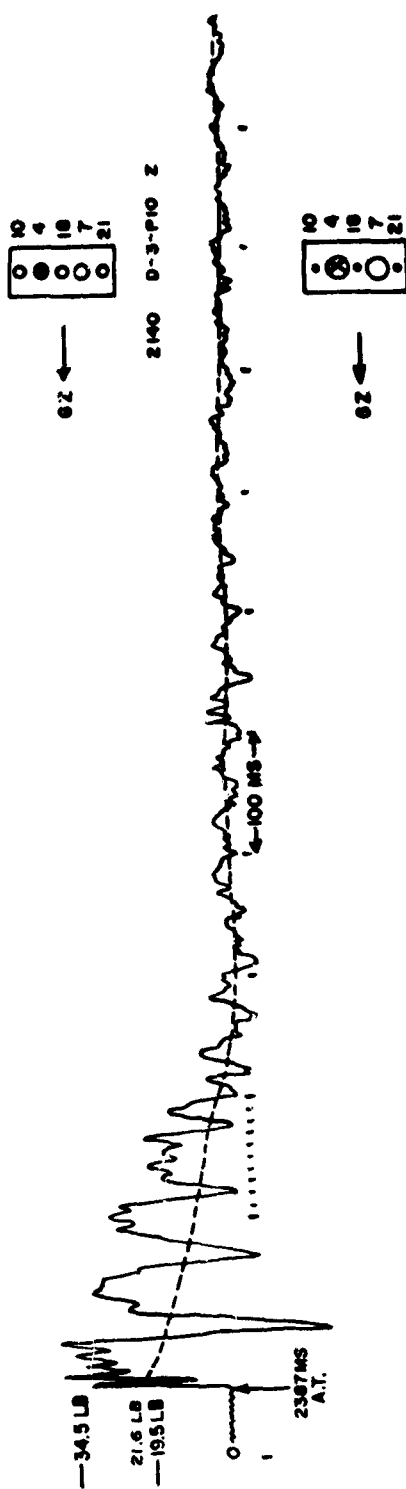


Figure 3.24 Force-Time Records in Three Components for Gage D-3-P10.

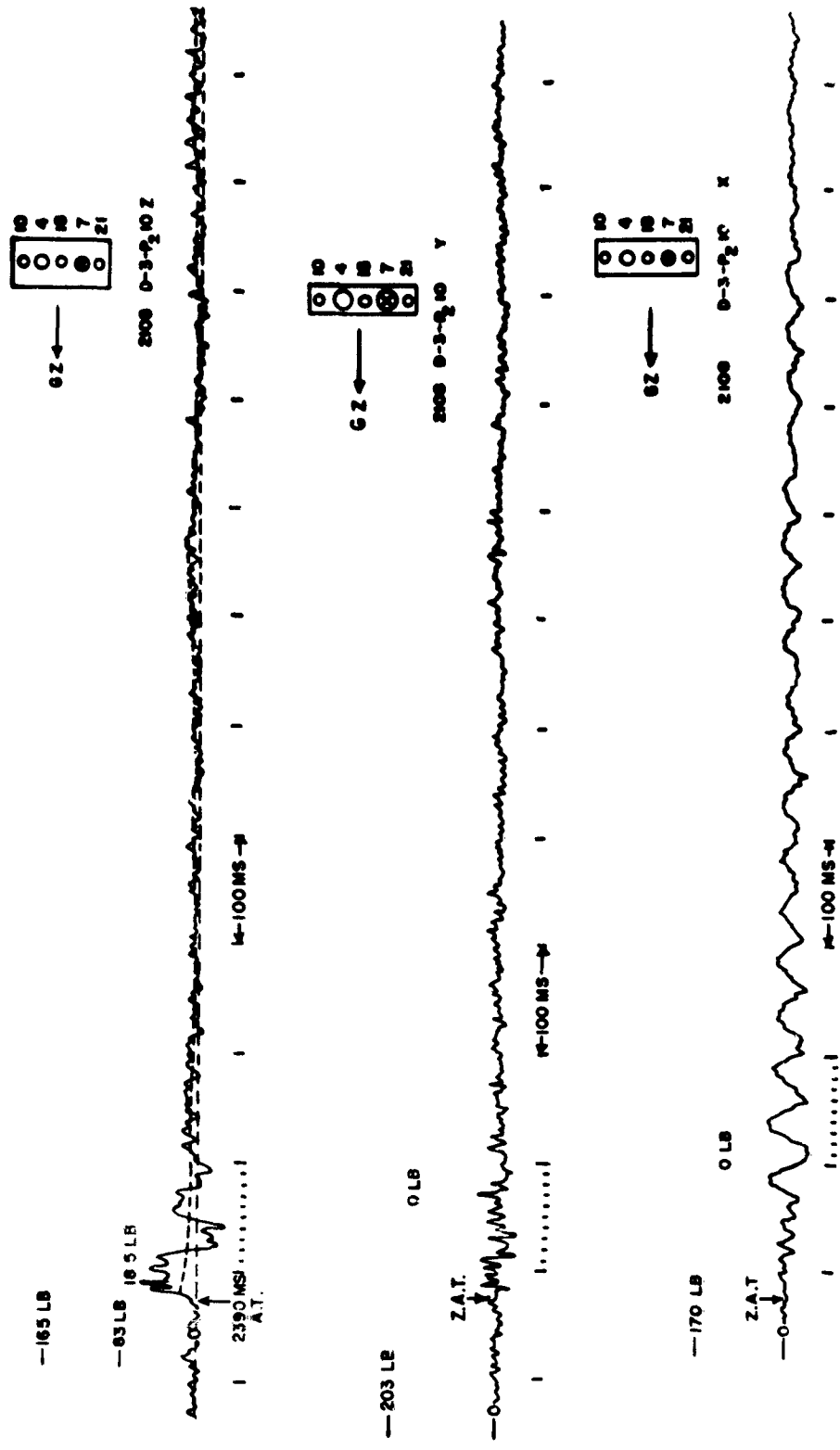


Figure 3.25 Force-Time Records in Three Components for Gage D-3-P<sub>2</sub>10.

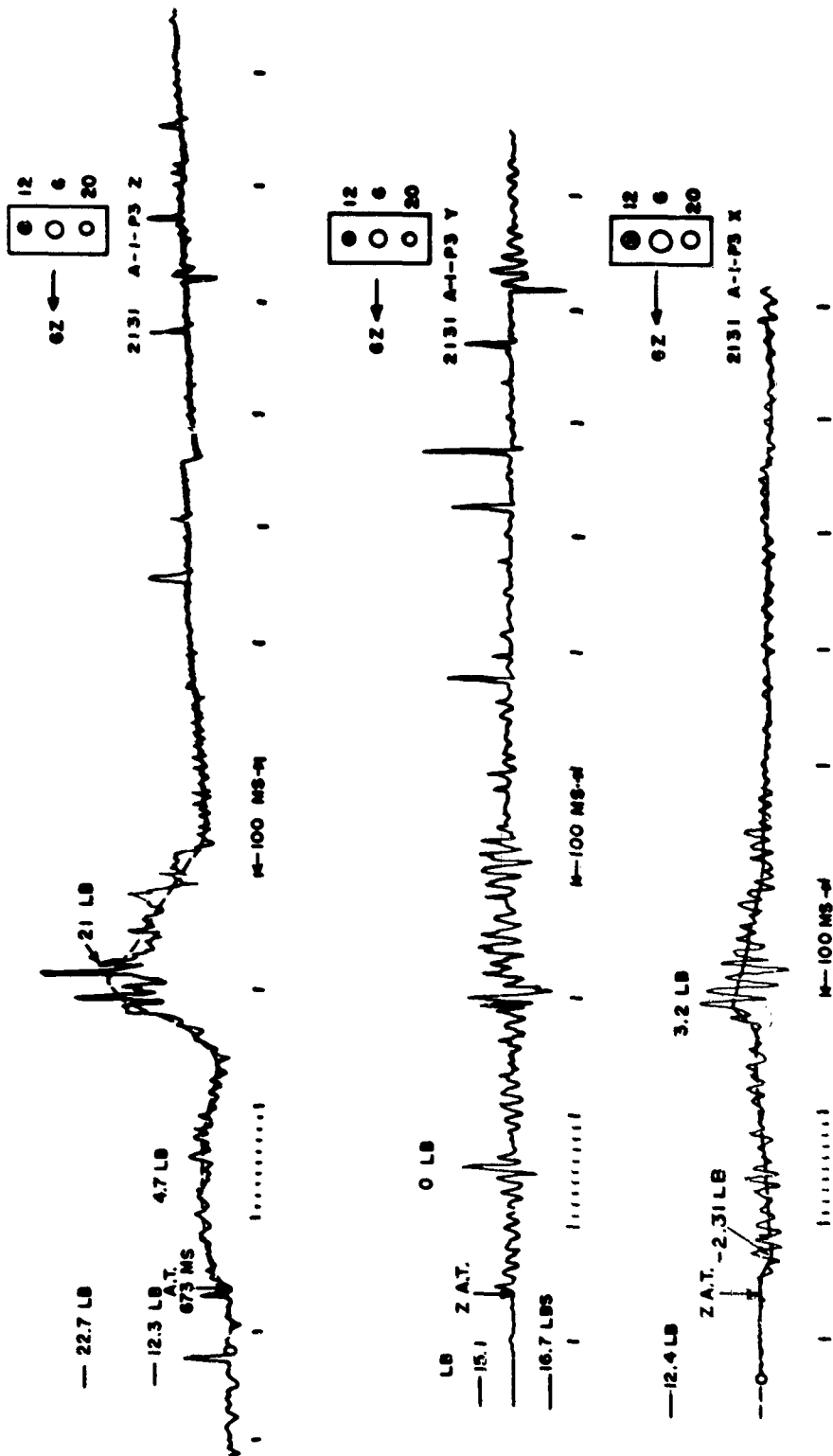


Figure 3.26 Force-Time Records in Three Components for Gage A-1-P3.

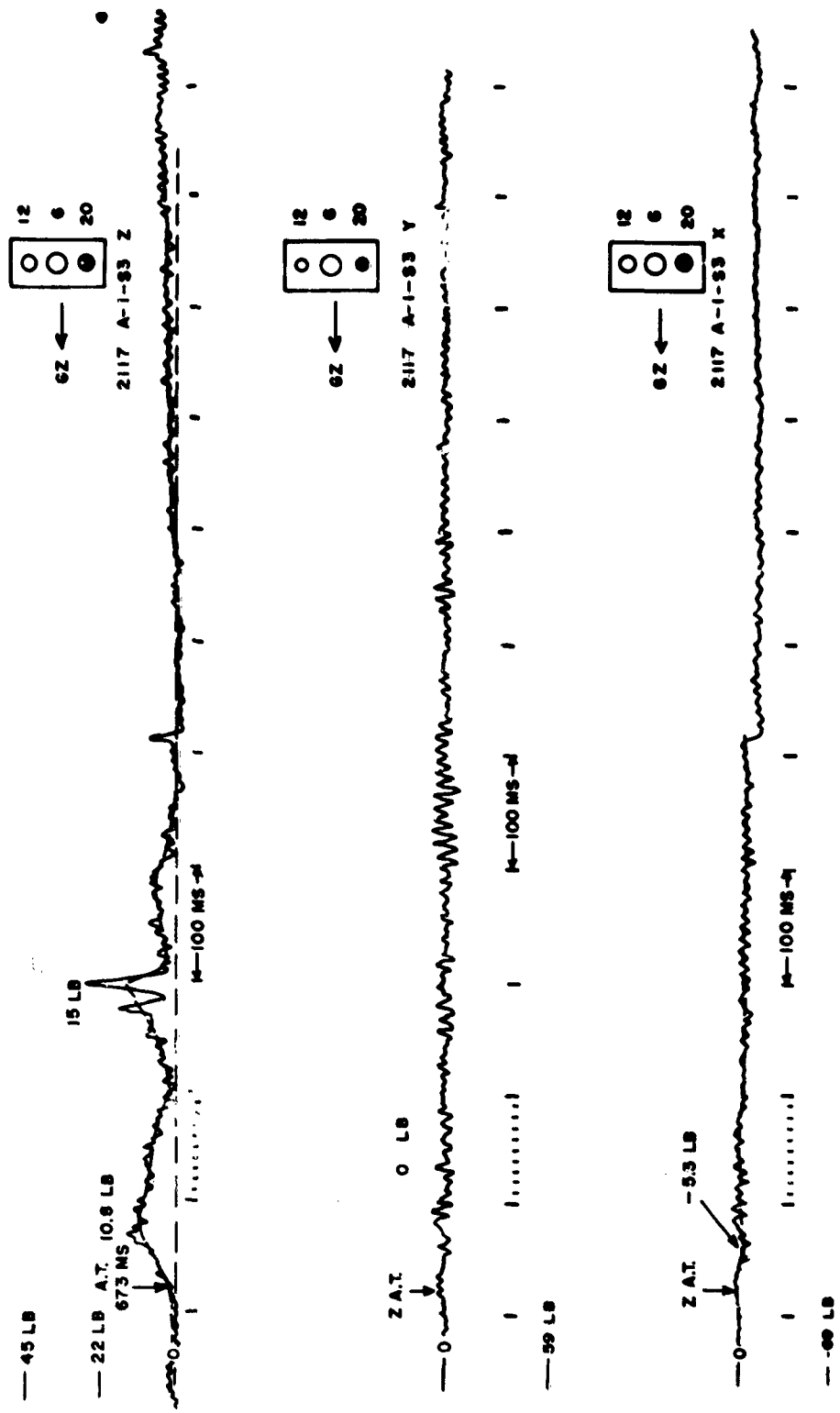


Figure 3.27 Force-Time Records in Three Components for Gage A-1-S3.



Figure 3.28 Force-Time Records in Two Components for Gage A-1-P10.

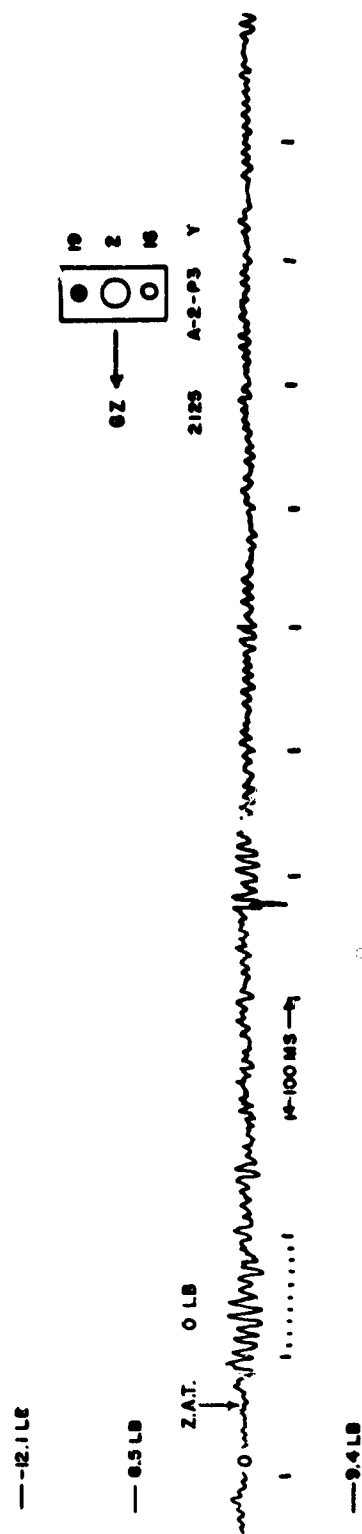
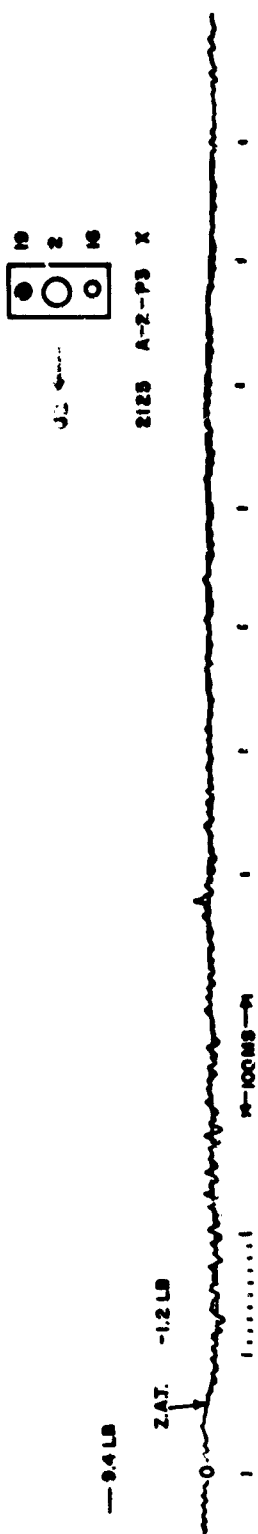
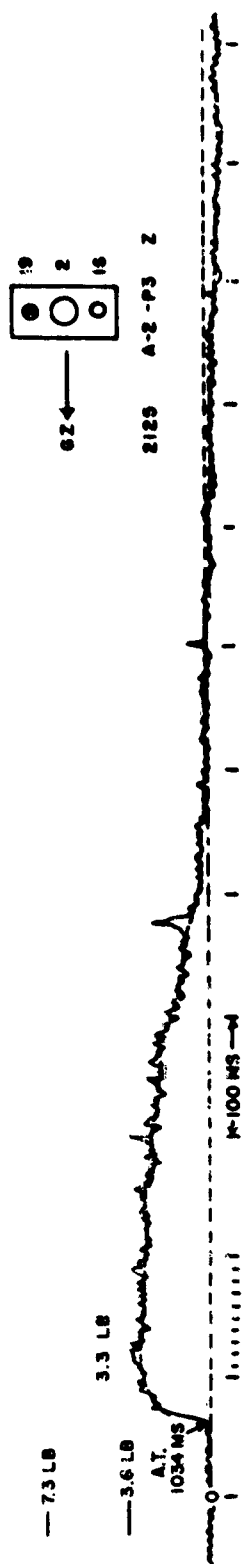


Figure 3.29 Force-Time Records in Three Components for  
Gage A-2-P3.

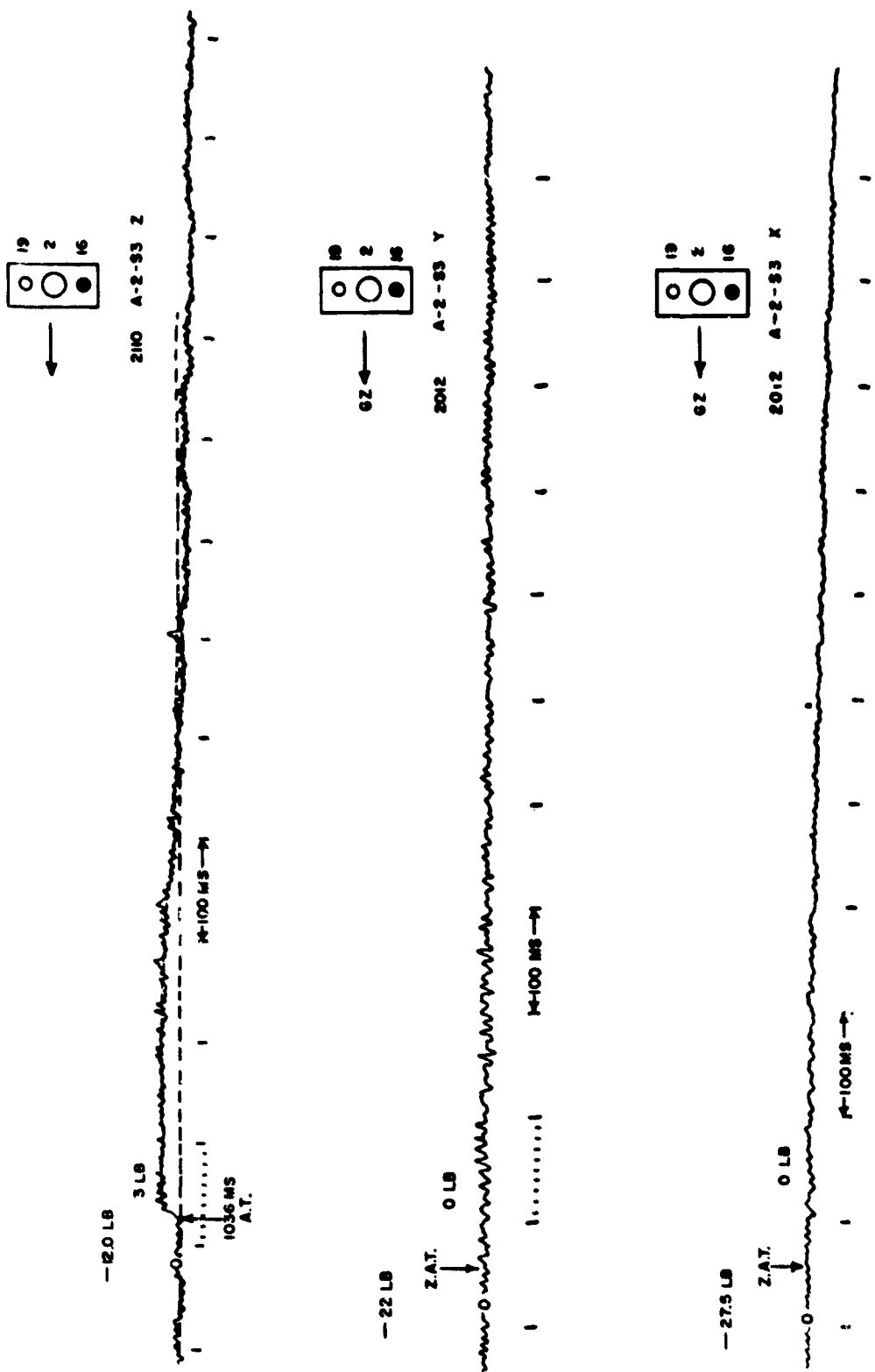


Figure 3.30 Force-Time Records in Three Components for  
Gage A-2-S3.

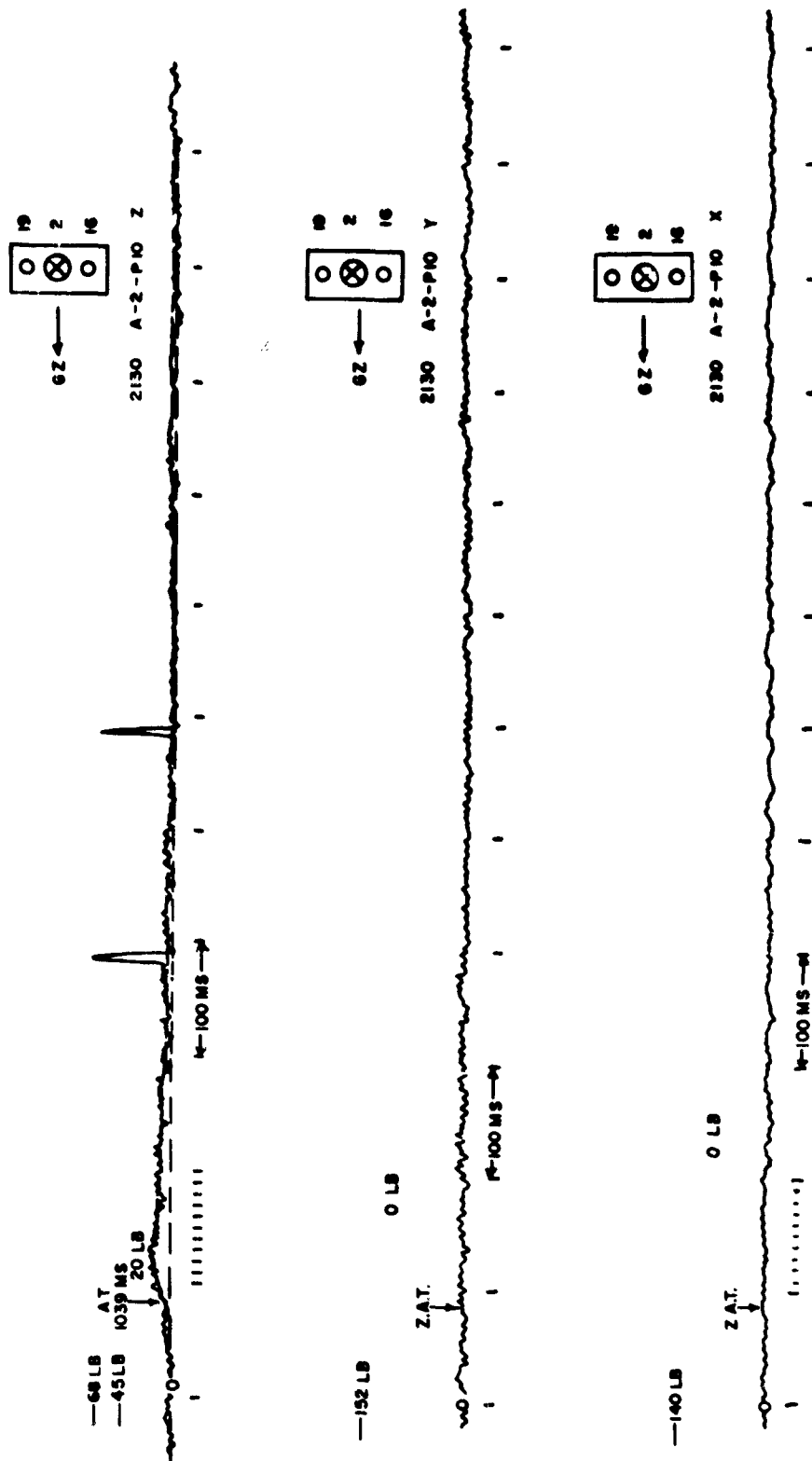


Figure 3.31 Force-Time Records in Three Components for Gage A-2-P10.



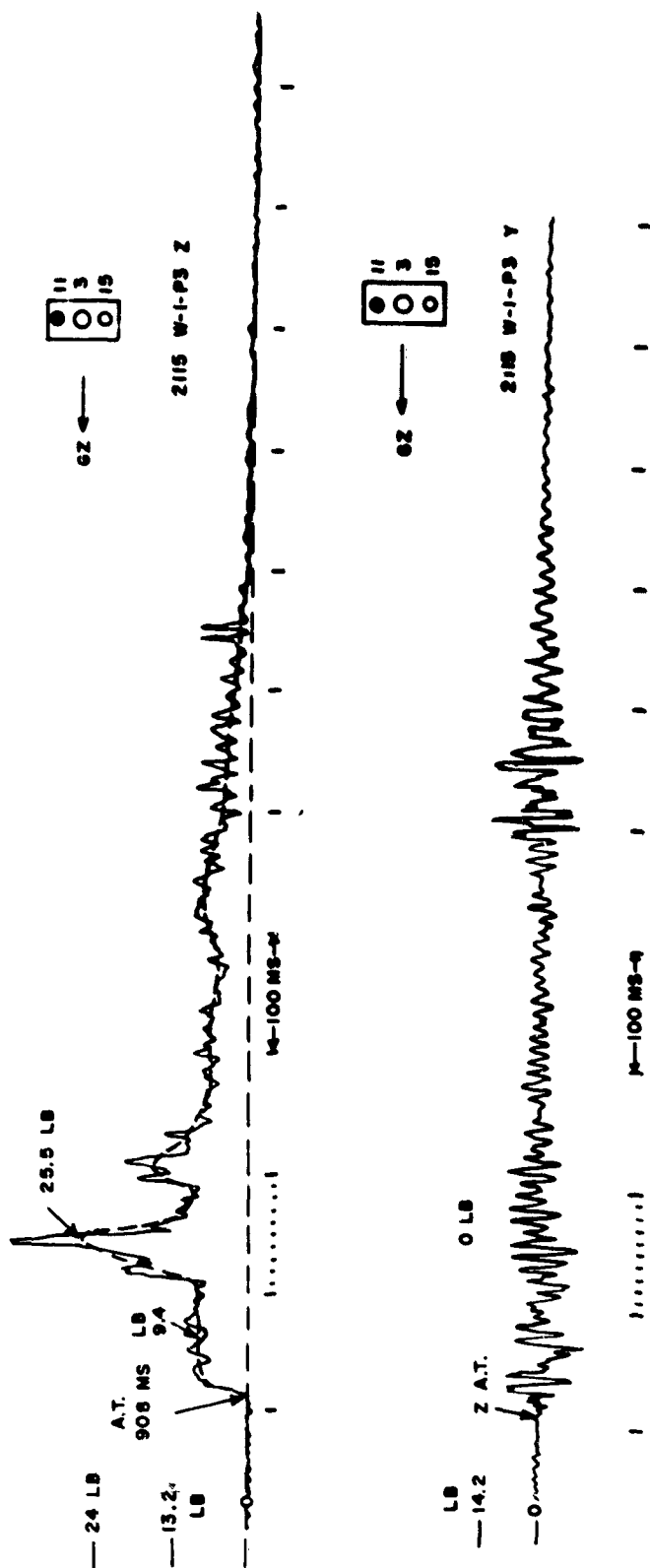
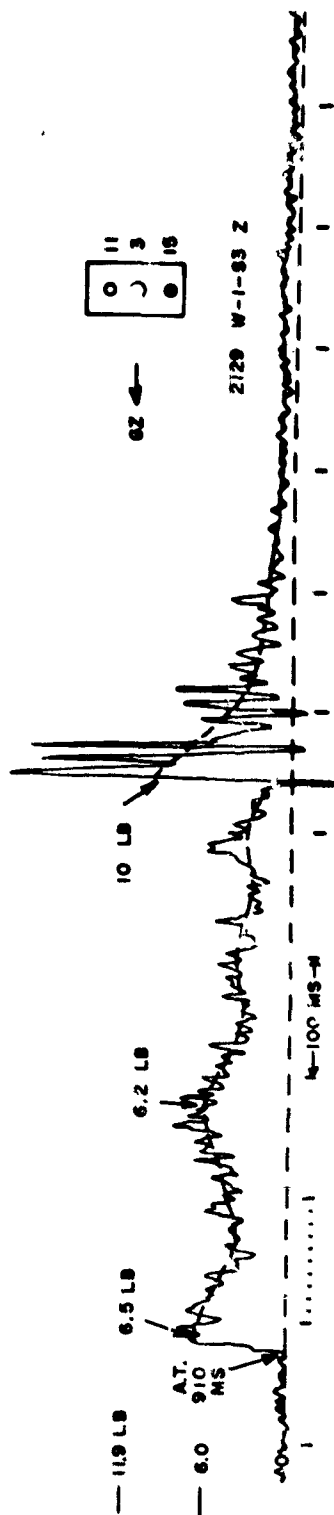


Figure 3.32 Force-Time Records in Two Components for Gage W-1-P3.



Box: 11, 3, 15

2129 W-1-S3 Y



Box: 11, 3, 15

2129 W-1-S3 X



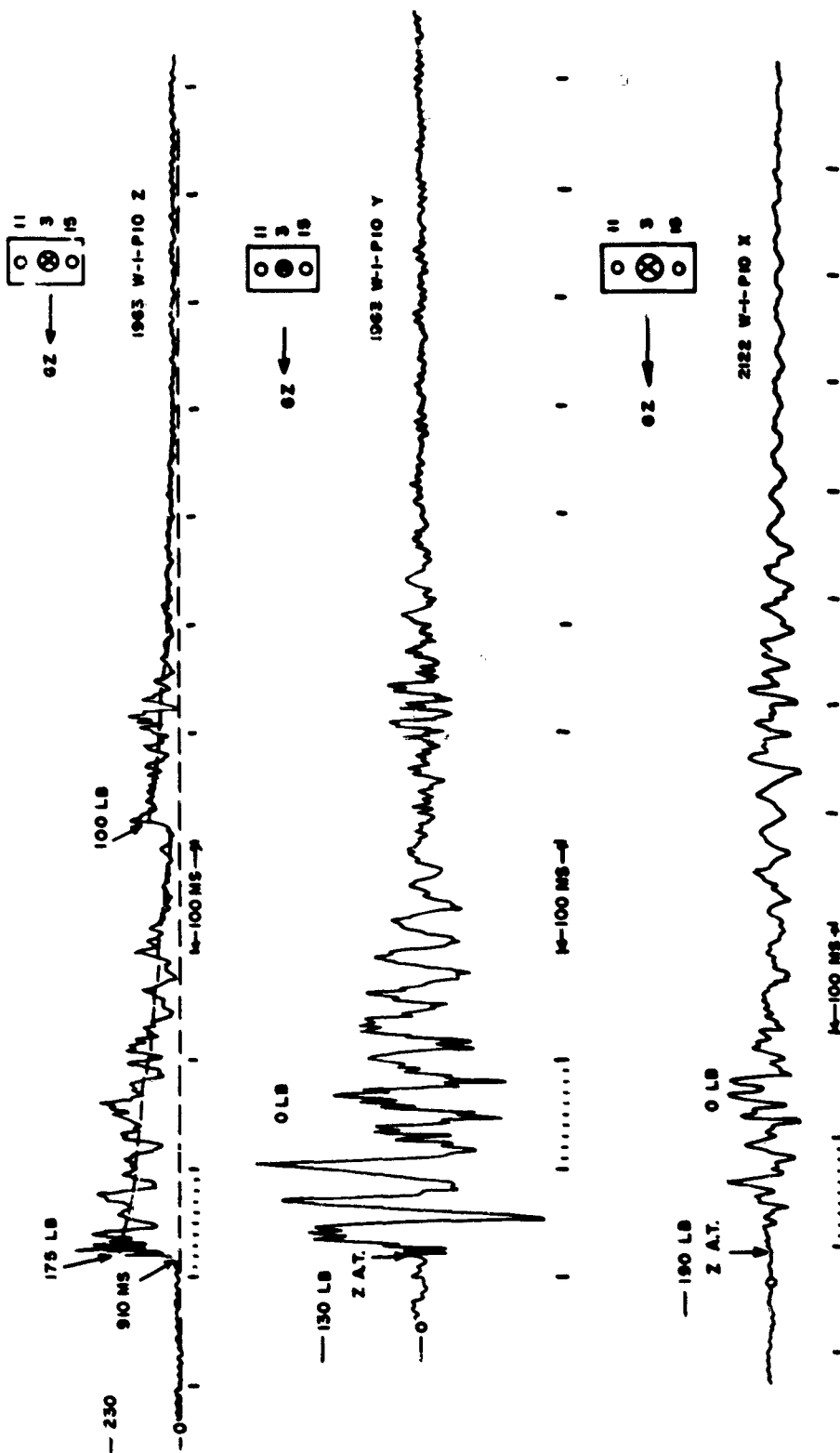


Figure 3.3<sup>1</sup> Force-Time Records in Three Components for Gage W-1-P10.



Figure 3.35 Force-Time Records in Two Components for  
Cylinder Gage at 3,500-foot Desert Station.

there appears to be more oscillation on the X and Y records than on the Z component, the net force on most records is either negligibly small or zero. These oscillations are probably due to sting "ring." If a pitch or yaw component of force as little as 5 to 10 degrees was present in the forcing function, the gages should have responded with adequate signal, since the three sensors of each gage had approximately the same sensitivity (especially since the laboratory tests produced a much higher indicated pitch angle, measured from the force components, than that actually existing between flow and sting axis). Some records, however, show what appear to be abnormally high X and Y signals; possibly due to local flow inhomogeneities. It should be stated again that scouring, dents, and holes are generally distributed symmetrically around the Z axis on the front hemispherical shell. Some dents and scratches on the top back half of the spheres are possibly due to the downward phase of missile trajectories.

The relative degree of denting and scouring of the sphere shells has been noted, since it may thus be possible to deduce some information as to the heterogeneity of the blast-propagating medium. The similar gages at the 2,500-foot radial distance in the dusty desert region (D-1) and the asphalt region (A-1) were equally and severely abraded, dented, and punctured; the number and size of dents and degree of scouring are essentially the same.

An experimental 1/4-inch-thick Fiberglas plastic covering was used on the D-1-P10 sphere. This covering showed good impact resistance with no shell punctures, although the aluminum shell under the plastic cover was dented and the plastic cover suffered a few deep gouges and considerable skin abrasions.

For the same radial distance in the water area (W-1), only a few isolated dents appear on the sphere shells, and only the 3/16-inch deep dent on W-1-S3 is of any significance. There was no appreciable scouring of the spheres in this water area.

At the two stations at 3,000 feet on the asphalt (A-2) and desert (D-2) areas, the sphere shells suffered considerably less denting and abrasion than did those at 2,500 feet in these same areas. Although there were a few more dents in gages in the asphalt area (A-2) than in the desert area (D-2), the degree of abrasion was about the same.

Outside of a few insignificant scratches, there was no damage sustained by the gages at the 4,500-foot D-3 station. It should be noted that all gages in the asphalt area were completely coated with a thin, black layer of asphalt during the shot.

The arrival times of the force functions at the different gages and stations are listed in Table 3.1. It is evident that over the thermally-absorbing asphalt area the shock-front velocity was considerably greater than over the water surface and the desert surface,

the velocity being lowest over the water. The average arrival times at each station are in excellent agreement with the SRI arrival-time data for corresponding stations.

3.4.2 Cylindrical Force Gage. The experimental cylinder gage, placed at 3,500 feet along the desert line, produced clean records (Figure 3.35) devoid of extraneous oscillations and irregularities. The magnitude of the force in the head-on Z component (70 pounds) is in the expected range, although somewhat high. The Y component appears large for a station located in what should be a clean Mach region. No conclusions are drawn regarding the significance or validity of this one record, since practical design difficulties prevented an effective field calibration of the gage. Arrival time of the force signal at this station agrees well with SRI date.

### 3.5 DRAG COEFFICIENTS

Up to this point the force records have been presented more or less as obtained, with no attempt made to correct for pressure effects on gage performance and with no attempt to calculate and compare drag coefficients. The main reason for not trying a more-refined approach was that the condition of each gage was unknown as regards pressure leakage to the interior of the shell (see Section 2.3). Prior to the field test the necessity of knowing the leakage characteristics of each gage was not realized, and no laboratory tests were made to check this performance feature. Most of the gages were damaged during the test; therefore, only three 3-inch gages were checked for leakage in the laboratory after the field test. Two of these gages were effectively sealed, but the third gage leaked badly. The 10-inch gages had been vented deliberately (approximately 1 inch of the annular Pliobond seal left off at the top of the sting) for field use, and it was assumed that base pressure leaked in through this opening. No evaluation was made, however, of the dynamics of the leakage process, and no "time constant" was estimated for the 10-inch-gage leakage. Although the punctured shells permitted rapid leakage, the force records do not conclusively indicate the time of occurrence of the punctures. In light of the above remarks, the conclusion to be reached appears to be that some of the gages were well sealed for long durations (in which case Equation 2.1 is applicable), others were sealed for only a short part of the shock-wave duration (because of slow leakage through the seal or because of puncturing the shell during the blast), and still others leaked rapidly enough to be considered unsealed (in which case Equation 2.2 is applicable).

The force-time records themselves provide some information on the conditions of the gages in the field as regards leakage. Figures 3.36 through 3.42 consist of smoothed records of force-time, with corresponding curves of  $C_p$ -time, based on SRI  $q$ -time and  $P_s$ -time values. Wherever there are two force-time curves on one plot, the upper curve represents the raw force data (smoothed from Figures 3.8 through 3.14) and the lower curve represents the corrected force values for a sealed

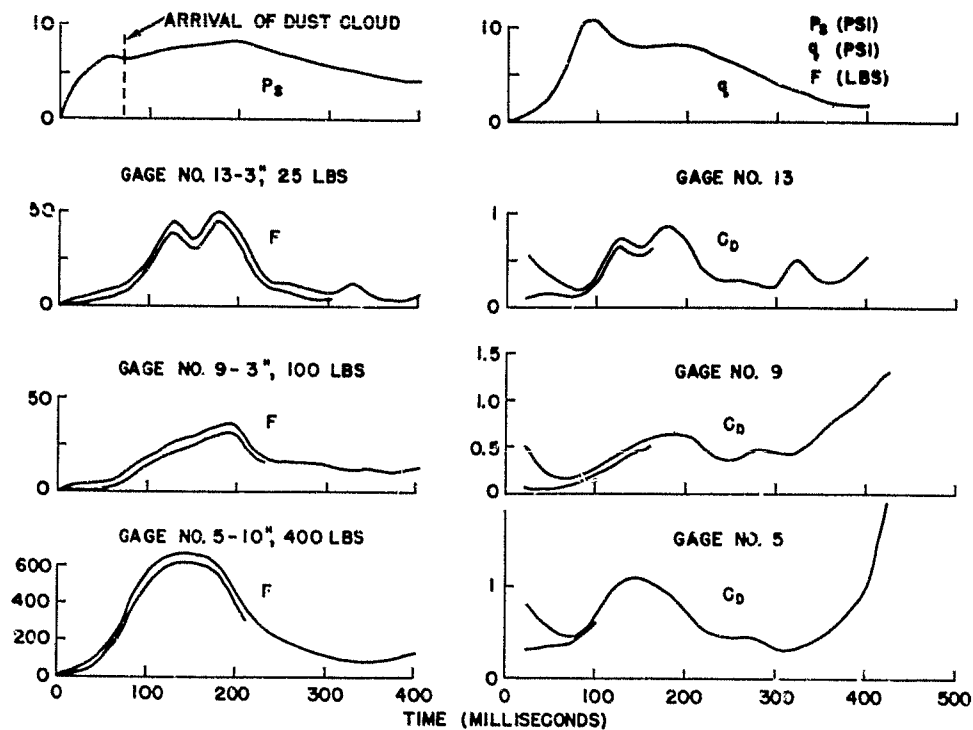


Figure 3.36 Pressures, Forces, and Drag Coefficients at 2,500-foot Desert Station.

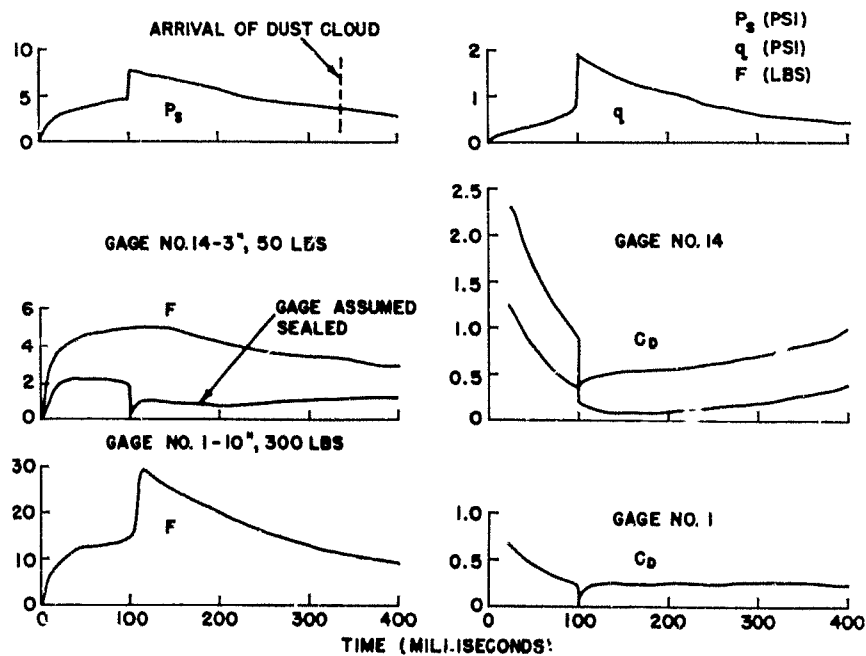


Figure 3.37 Pressures, Forces, and Drag Coefficients at 3,000-foot Desert Station.

CONFIDENTIAL

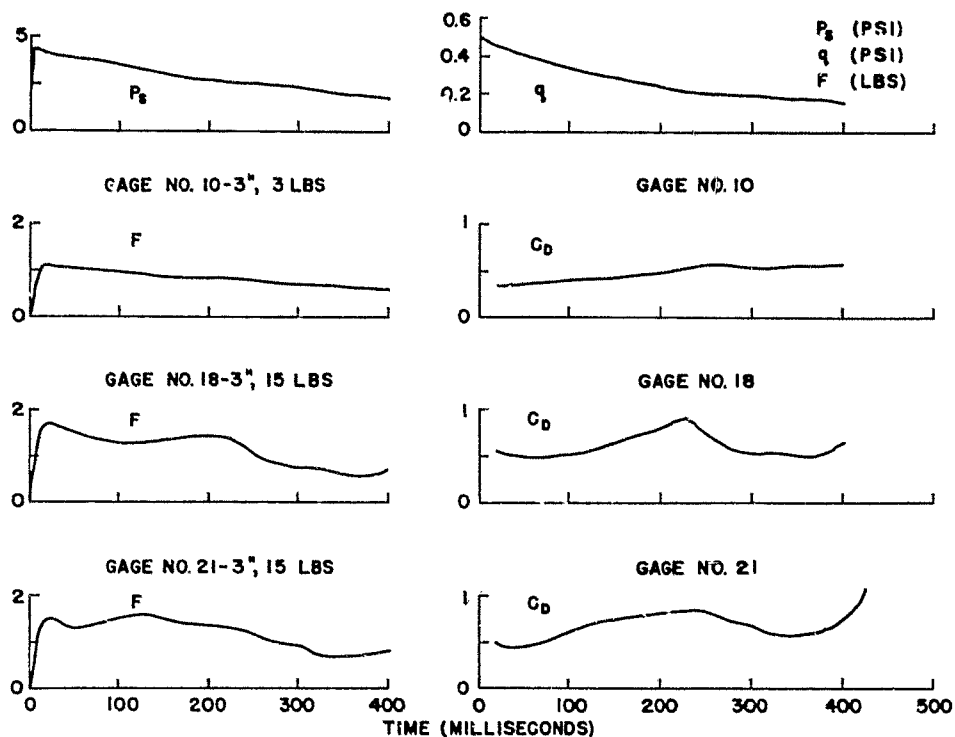


Figure 3.38 Pressures, Forces, and Drag Coefficients at 4,500-foot Desert Station (3-inch Gages).

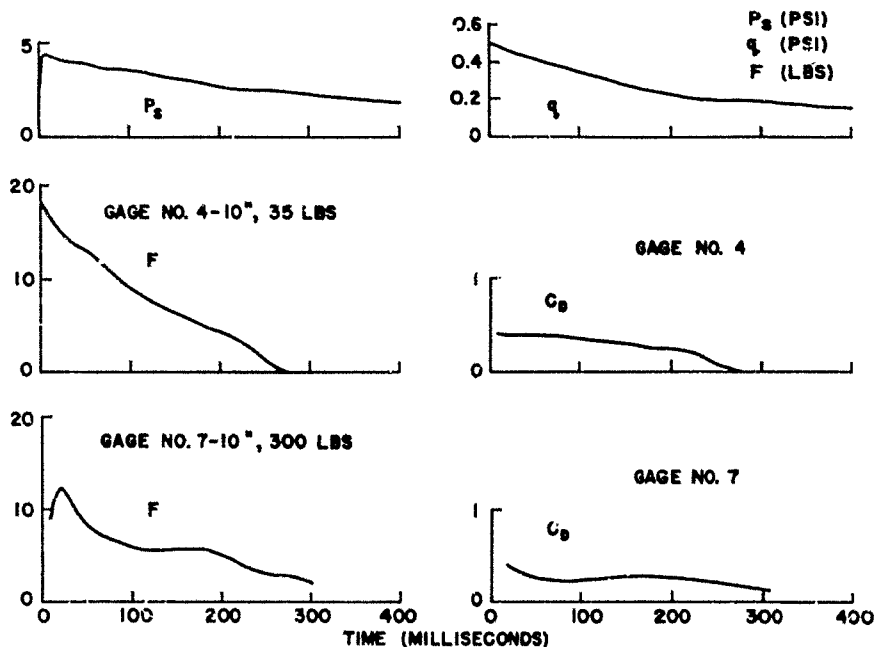


Figure 3.39 Pressures, Forces, and Drag Coefficients at 4,500-foot Desert Station (10-inch Gages).

CONFIDENTIAL



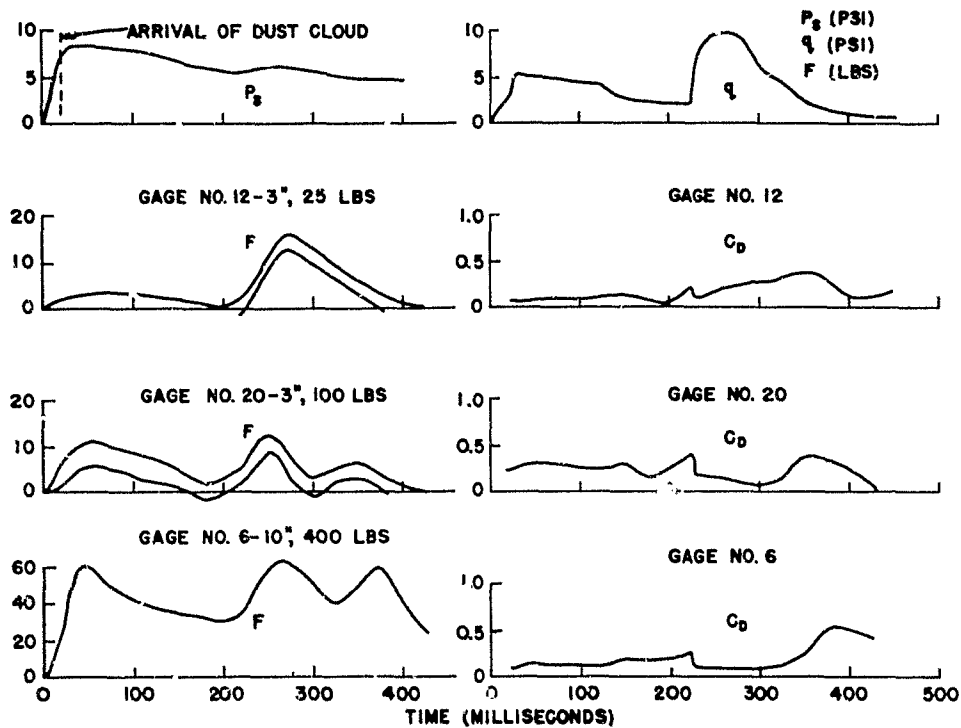


Figure 3.40 Pressures, Forces, and Drag Coefficients at 2,500-foot Desert Station.

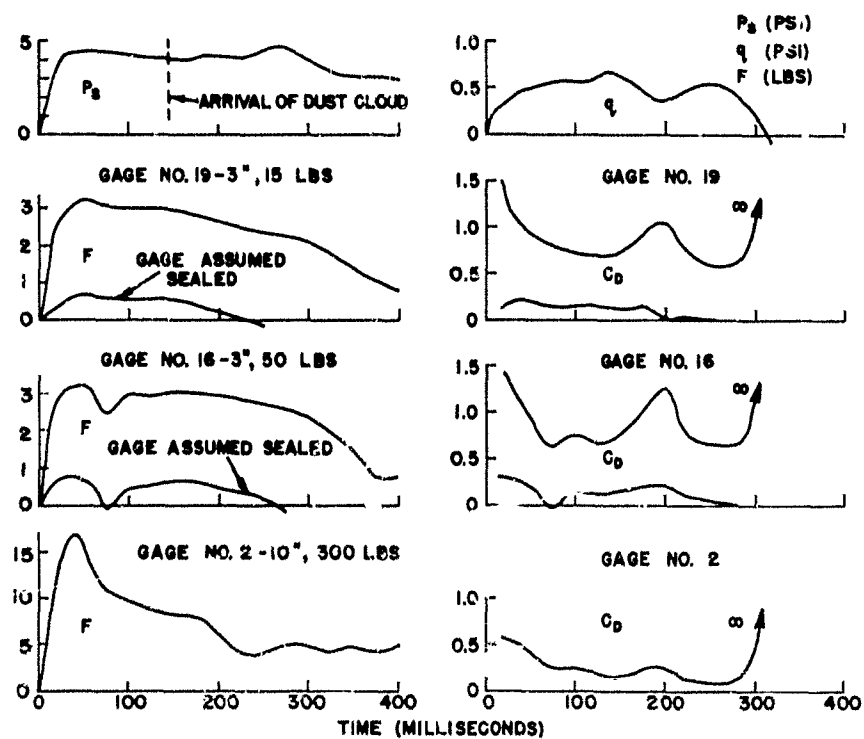


Figure 3.41 Pressures, Forces, and Drag Coefficients at 3,000-foot Asphalt Station.

gage. The lower curve was omitted wherever the pressure correction resulted in negative values.

Some 75 percent of the 3-inch-gage records could be adjusted with positive force curves resulting, but this does not necessarily mean that 75 percent were perfectly sealed. On the contrary, since all 3-inch gages were prepared alike, the fact that 25 percent were leaking excessively could lead to the conclusion that all were leaking somewhat. For this reason it was concluded that the best one could do was

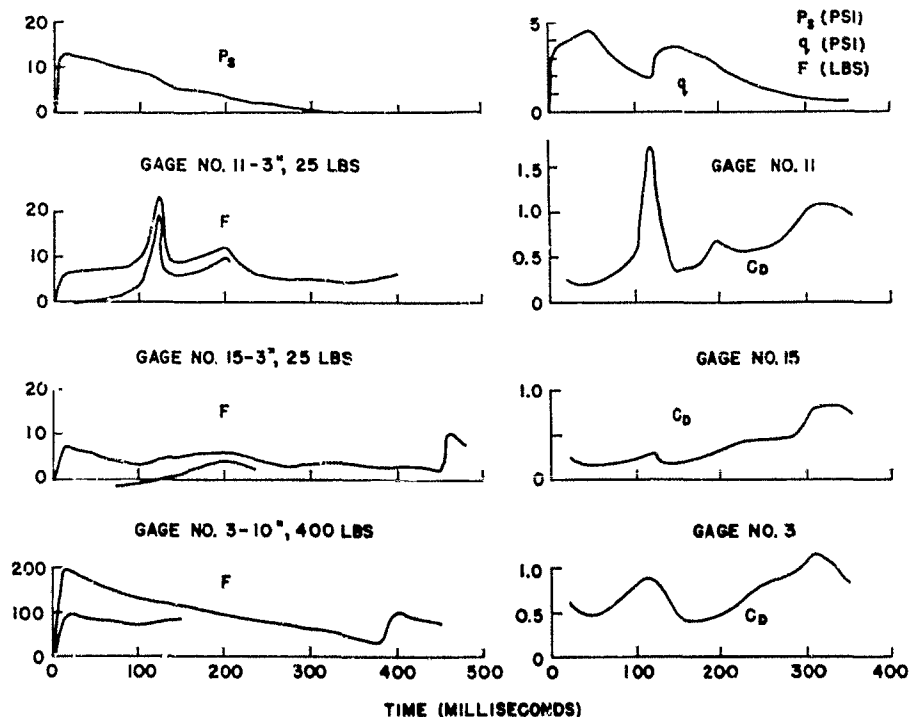


Figure 3.42 Pressures, Forces, and Drag Coefficients at 2,500-foot Water Station.

use the values between the raw force data and the corrected data, even though the spread may be too large for anything but order-of-magnitude estimates.

Since the 10-inch gages were intentionally left open to external pressure, one could apply the pressure correction for a rapidly leaking gage and use the results for  $C_D$  with a maximum error of  $\pm 0.1$ . The curves of  $C_D$ -time for gages with gage numbers of 8 or lower (10-inch gages) are thus believed to indicate  $C_D$  values correct to within  $\pm 0.1$ . Since it was not expected that correspondence of  $C_D$  with  $P_s$  would be likely for a nonhomogeneous shock wave (due to differences in dust particle size, density, and velocity), an attempt was made to correlate  $C_D$  for the 10-inch gages with pressure level; all  $P_s$  and  $C_D$  values were taken at 20 msec after shock arrival which is prior to the arrival of the dust cloud. The  $C_D$  values ranged between 0.1 and 0.8 with no obvious correlation between  $C_D$  and  $P_s$ .

The lack of correlation could be due to: (1) nonuniform gage leakage in 20 msec, (2) overdamped gages (several of the gages later checked in the laboratory were found to be overdamped) creeping back from a diffraction spike (see Chapter 6), (3) the unsteady nature of the transition phase and "pseudo-steady" drag phases (20 msec represents about 35 transit times for the 10-inch sphere in a blast at moderate overpressures), or (4) other reasons discussed below.

Another compelling reason for discounting the significance of the  $C_D$  values obtained on the field test is based on the fact that the  $q$  data obtained appear to be questionable, and calculations of  $C_D$

TABLE 3.2 - Comparison of Peak Values of  $q$  Measured by Several Agencies\*

Location Agency	Water			Asphalt			Desert		
	2000 ft	2500 ft	3000 ft	2000 ft	2500 ft	3000 ft	2000 ft	2500 ft	3000 ft
Project 1.10 SRI (Pitot Gage)	35	**4.6	2.9	17	10	0.68	43	10.7	1.8
Project 1.11 Sandia (Snob Gage)	6.5	4.0	---	9.5	~4.0	---	21	~4.0	---
Project 1.14 BRL (Diaphragm Gage)	35	---	2.9	16	8.5	1.7	45	12.5	1.7
Average	25.5	4.3	2.9	14.2	7.5	1.2	36.3	10.7	1.75

\*All measurements at 3-ft height

\*\*7.4 psi spike smoothed to 4.6 psi

Data taken from preliminary reports listed below; also from final figures where available:

SRI - "Operation TEAPOT Preliminary Report - Project 1.10 - Air Blast Overpressure and Dynamic Pressure Over Various Surfaces" ITR - 1109, L. M. Swift, D. C. Sachs, May 1955

Sandia - "Operation TEAPOT Preliminary Report - Project 1.11 - Special Measurements of Dynamic Pressure vs Time and Distance" ITR - 1110, J. R. Banister, F. H. Shelton, May 1955

BRL - "Operation TEAPOT Preliminary Report - Basic Blast Measurements for Projects 1.14a, 3.1 and 3.10" ITR - 1155, E. J. Bryant, M. H. Mithridge, J. H. Keefer, May 1955

depend upon them directly, as indicated in the formula  $C_D = F/qA$ . Table 3.2 presents a comparison of peak values of  $q$  measured by Projects 1.10, 1.11, and 1.14, the peaks not necessarily occurring at the same time for any one location. The spread in these values tends to confirm the a priori assumption that each design of  $q$  gage reads differently in an inhomogeneous medium. Figure 3.43 provides the comparison in wave shape between BRL and SRI  $q$ -time records. The discrepancies between the 3,000-foot asphalt records of Figure 3.43 occur before the dust cloud arrives at the gage station. There is little point in computing  $C_D$  with such inconsistent  $q$  data, unless one  $q$  gage were selected as the "Standard Gage", in which case the academic  $C_D$  values thus computed would still have no significance for any other applications.

The final reason for not reporting singular values of  $C_D$  is that the force gage with a spherical model has poor repeatability when used for determination of  $C_D$  (as has been discussed theoretically and

found experimentally in the laboratory). The need for statistics is found to be imperative under controlled laboratory conditions, and it becomes even more necessary when  $q$  measurements show a great spread from instrument to instrument. The answers obtained by averaging two readings at a station can hardly be regarded with a high level of confidence, particularly when a shock-tube experiment representing many repeated shots with one gage may show one standard deviation greater than the average reading.

Although the above reasoning leads one to avoid the calculation and reporting of drag coefficients in other than graphic form

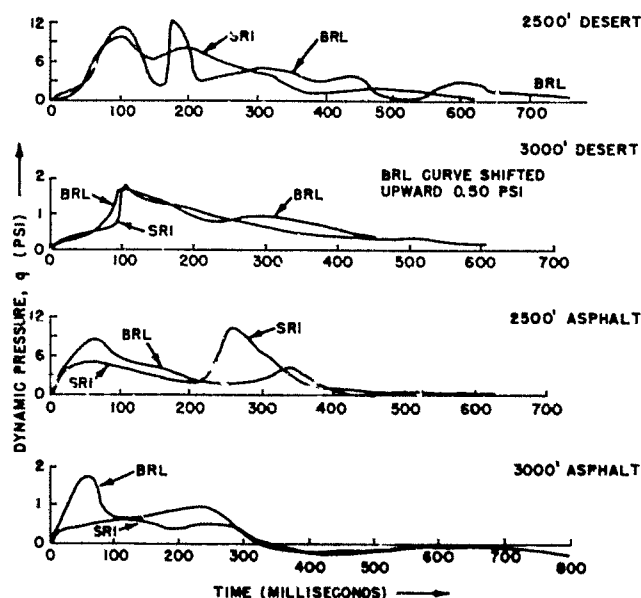


Figure 3.43 Comparison of BRL with SRI Dynamic Pressure Records for Shot 12.

(Figures 3.36 through 3.42), the experimental data collected on Shot 12 may be used validly for comparing the relative effectiveness of blast loading over the three areas. That is, the results shown in Table 3.1 still have the same relative order, regardless of whether or not the gages were leaking. Thus it is still possible to compare the military effectiveness of the blast over the areas, despite the lack of knowledge of what factors contributed most significantly to these effects.

### 3.6 SUMMARY OF RESULTS

In view of the previous discussion of the significance of the absolute values measured, the results are summarized only with the purpose of making comparisons of the peak forces measured over the water, asphalt, and desert areas at equal distances from ground zero. Table 3.1 presents the numerical results; Table 3.3 presents the results in order of amplitude of force and pressure. For example, D-A-W

means that the peak force was highest in the desert area, next in the asphalt area, and lowest in the water area.

For correlation with damage to drag-type targets, one would expect to use either force values or  $q$  values; the  $P_s$  values are presented for comparison only. At 2,500 feet the force and  $q$  values agree in that they both indicate the desert area to be most conducive to damage, with an inconclusive order for asphalt versus water areas. At 3,000 feet, however, the  $q$  gages have their highest reading in the water area, while the force gages read highest in the desert area. On the basis that the force readings are one step closer than the  $q$  readings to the desired indication of damage to structures, plus the fact that the  $q$  values obtained to date are decidedly sensitive to gage design and are to be questioned as to their reliability, the conclusion is reached

TABLE 3.3 - Comparison of Effects at Equal Range  
for Three Areas (3-foot height)

Quantity Range	Force on 3-in. Gages (NOL)	Force on 10-in. Gages (NOL)	Dynamic Pressure, $q$ (BRI)	$P_s$ (BRI)
2500 ft	D-A-W	D-W-A	D-A-W	W-D-A
3000 ft	D-A	D-A	W-D-A	W-D-A

that the desert area is most conducive to damage as compared to the other two areas. The asphalt and water areas, on the basis of existing data, cannot be ordered one above the other conclusively.

Agreement between BRL and NOL force records at the 2,500-foot desert station is good with regard to peak force (BRL reports 39 pounds for the 3-inch gage compared with the 40-pound NOL average, and 740 pounds for the 10-inch gage, compared with the 650 pound NOL approximation), but there is poor agreement in wave shape, i.e., time coincidence of peaks. At the other check points at the 4,500-foot desert station and the 2,500-foot asphalt station, the BRL recorded peak forces were much higher than the NOL recorded peaks. At station D-3, BRL had peak readings of 6.9 pounds for the 3-inch gage and NOL had as an average for three 3-inch gages 1.5 pounds; at A-1, BRL computed 195 pounds peak force for its 10-inch gage and NOL, for a similar size gage, recorded only 62 pounds. (The high peak force readings of the BRL gages may have resulted from BRL gages being sealed better than the NOL gages.) The BRL preliminary report (ITR-1155) lists the highest drag pressures on the desert line, followed in descending order by the asphalt line and the water line. However, greater vehicle damage was sustained on the water line than on the asphalt line, with maximum damage on the desert line (BRL Project 3.1). These inconclusive results for asphalt versus water areas, with dusty desert area always producing highest loads, are in general agreement with NOL results. One is compelled to admit, however, that absolute, quantitative values of drag forces and drag coefficients as a function of time are yet to be obtained with convincing reliability.

## Chapter 4

# CONCLUSIONS AND RECOMMENDATIONS

### 4.1 CONCLUSIONS

The major objectives of the Teapot field test were attained with the exception of that objective dealing with the correlation of drag coefficients. A three-component force gage suitable for measurement of transient aerodynamic loads on sting-mounted models was successfully developed and used on Shot 12. Drag force-time measurements on spheres exposed to a nuclear detonation in three different areas---a thermally absorbing asphalt area, a thermally reflecting water area, and a thermally absorbing desert area---were obtained successfully (59 records out of a possible 61).

The military effectiveness of these three different areas was arrived at by a comparison of peak forces at a 3-foot height. This comparison indicated the highest forces in the dusty desert area, with lower forces in inconclusive order in the asphalt and water areas. In all three areas the flow of air and solid particles was found to be horizontal and in radial lines from ground zero.

The general conclusion is reached that the force on a model as a function of time represents a physically meaningful property of the blast wave. Whether force is a parameter of greater significance than dynamic pressure in the establishment of damage criteria for structures, etc., it is yet too early to say. Neither the force gages nor the  $q$  gages respond to a dust-laden blast with readings which may be used readily at this time for prediction of full-scale loading (the force gage because of size effects, size of model relative to particle size, and variable drag coefficient and the  $q$  gage because of the size of its housing and the size of the sampling hole). Both types of gages indicated the same order of damage effectiveness of the three areas of Shot 12, although the force gage showed a much greater percentage difference between readings in the different areas. Pending further investigation of the relative merits of force and  $q$  measurements, it is concluded that both parameters have more or less equal physical significance with regard to the damage process.

Drag coefficients obtained in the field could not be compared legitimately with the shock-tube and wind-tunnel drag coefficients for the following reasons: (1) The condition of each gage, in regard to the leakage of pressure into the model, was unknown at the time of test. (2) The effect of dust loading could not be subtracted from the total recorded force to show the net aerodynamic force. (3) The dynamic pressure readings were considered unreliable. (4) The variability in aerodynamic loading of spheres, as indicated by extensive laboratory

tests, is so high as to render the results obtained by two or three gages at a station of poor statistical significance.

#### 4.2 RECOMMENDATIONS

Research into the behavior of force gages and q gages in clean and dust-laden blast is recommended, starting with the more-obvious parameters of size and shape of the gage and the usually significant flow properties, such as dust particle size and density, Reynolds number, and Mach number. Part 2 of this report represents a limited investigation of this type, and it resulted in preliminary information on the transient aerodynamics of spheres. Much more laboratory effort of a similar nature is required before the spherical force gage may be considered a reliable field instrument. Likewise, it is recommended that considerable laboratory evaluation of force gages and q gages of various shapes be performed prior to use in the field.

It is recommended that the force gage models for use with a sting support be improved mechanically so that the effect of static pressure on the force reading may be compensated. Of the alternative approaches of either sealing the gage completely and subtracting the reading due to the external pressure from the total reading or allowing a known pressure to leak into the gage and thus perform an automatic subtraction, the latter is recommended. The basis for this recommendation is that greater accuracy is expected when the net reading is recorded than when two separate readings are recorded and then subtracted.

Based on the laboratory experiments, which indicated an extremely high variability of drag loading on spheres, it is recommended that the spherical force gages be used on field tests only when a statistical number of models (of the order of ten) may be mounted at each station. Use of two or three sphere models at a station is expected to result in unreliable average values of drag force. No recommendation is made with regard to models of other shape, although the published data on circular cylinders indicates that this shape also has great variability in its drag-coefficient data. Operation Redwing is expected to provide information on the variability of drag forces on spheres, cubes, circular cylinders, and cylinders of square cross section.

## *Part 2 Laboratory Investigations*

### Chapter 5 INTRODUCTION

#### 5.1 OBJECTIVES

The general objectives of the program were to: (1) obtain drag coefficient vs time for spheres exposed to clean shock waves with various pressure-time histories at overpressures up to about 25 psi; (2) obtain drag coefficients for spheres in steady wind tunnel flow at various Mach and Reynolds numbers; (3) determine the time required for the drag coefficient to attain a pseudo-steady value in clean shock flow; and (4) compare the pseudo-steady drag coefficients obtained in the shock tube with those obtained in the wind tunnel, with the previously published data on drag coefficients of spheres, and with the Teapot field tests results.

These general objectives could be made more specific by listing the individual parameters that may be expected to be important. One could list for purposes of investigation such items as Reynolds number, Mach number, shape of pressure-time loading function, turbulence, surface roughness, etc. In most cases, however, it was not considered likely that definitive answers would be obtained as to the influence of each of these parameters, due to limitations on the extent of the program. For this reason, the objectives were defined more broadly, leaving the extent of emphasis to be placed on each parameter to the discretion of the investigators. As a result of this method of cursory investigation of many problems, the results of this program should be considered of a preliminary nature pending further substantiation and elaboration.

#### 5.2 BACKGROUND

The background and theory of the Teapot drag force program, Project 1.12, has been presented in Part 1 of this report, and only the salient features of that discussion which bear upon the laboratory program will be repeated. Section 1.2 of Part 1 is therefore recommended for a more general background of the drag-loading problem.

It has been shown in Part 1 that there are some general problems in prediction of drag loading which must be solved, experimentally or theoretically, before one may intelligently use the steady-state wind-tunnel drag coefficients for the dynamic-blast situation. The general parameters of amplitude of force and time of occurrence of the force are both significant in the dynamic damage process, unless one can make the simplifying assumption that the pseudo-steady drag force is the only important factor for the structure under consideration. Since this



assumption depends on the unsteady aerodynamics and, also, on the structural frequency response, one cannot decide that each specific loading history may be considered as a steady drag load from the structural point of view. For example, for a loading pattern consisting of 50 transit times for the diffraction and transition phases (see Figure 1.1) followed by the pseudo-steady drag phase, the diffraction and transition phases would have structural significance to the structure with a 10 transit time natural period, while the drag phase would be the important part of the pattern to a structure with a 200 transit time natural period. Thus we note that the drag-loading problem consists of two main features: amplitude of drag force and length of time to attain the pseudo-steady drag phase.

The problems of amplitude and time must be studied for bodies of many geometric shapes, loaded by blast waves of varied time histories, before one may hope to attain an engineering "feel" for the blast-loading problem. The Teapot drag-force program constituted a step in this direction.

### 5.3 OPERATIONAL PLAN

Having selected the sphere as the Teapot model for use with the net-force gage, a survey was made of the published information on the drag coefficients of spheres. This preliminary survey provided background information needed for intelligent design of the force gage and, also, served as a basis for comparison with the shock-tube and wind-tunnel drag data obtained on the Teapot laboratory program. This body of data indicated that the 3-inch and 10-inch diameters selected for the Teapot sizes---3 inches as a small size which could still conveniently envelop a three component force balance and 10 inches as a convenient large size for purposes of scaling---would be used in flows which would result in Reynolds numbers above the critical values, which was desirable from the standpoint of expecting (hopefully) stable flow and reproducible results.

This choice of sphere sizes resulted in definite limitations on which facilities could be employed for aerodynamic evaluation of the spheres. For example, the 40-by-40-cm wind tunnel at NOL was considered suitable for the 3-inch but too small for the 10-inch spheres. Besides differences in size, the available facilities offered differences in flow characteristics which were considered significant.

As a result, the operational plan involved tests in two shock tubes and two wind tunnels as follows: (1) Ballistic Research Laboratories (BRL) 24-inch diameter shock tube for 3-inch spheres, shock with flat-top of about 15-msec followed by a decaying wave; (2) Armour Research Foundation (ARF) 6-foot diameter shock tube for 3-inch and 10-inch spheres, peaked shock of about 25-msec duration; (3) Naval Ordnance Laboratory (NOL) 40-by-40-cm wind tunnel for 3-inch gages, blow-down tunnel with several minutes duration of flow; and (4) David Taylor Model Basin (DTMB) 7-by-10-foot transonic wind tunnel for 3-inch and 10-inch spheres, continuous flow.

## Chapter 6

# INSTRUMENTATION

The main features of the force-gage sensing and recording system are the following:

1. The load on the force gage produces a deflection of a flexible member of the gage structure, which changes the gap, (nominally 0.010 to 0.015 inches) between a mu-metal disc and an E-core inductance coil, thus changing the inductance of the circuit.
2. The inductance variations modulate the center frequency of a Hartley oscillator.
3. This frequency-modulated signal is transmitted to a magnetic-tape recorder or through a discriminator circuit to an oscilloscope for photographic recording.

Further details of the electrical design features are available in Part 1 of this report and in References 29 and 30.

The use of inductance pickups and the associated recording equipment had been well established on previous operations, and the major development problems centered about the mechanical performance of the force gage. The following sections are devoted to the design of the force gages, considering the mechanical problems of damping and frequency response, and the environmental problems due to the effect of the diffraction phase of the loading, the effect of the static overpressure in the shock wave, and the effects of dust in the shock wave.

### 6.1 DESIGN FOR AERODYNAMIC PERFORMANCE

6.1.1 The Loading Picture. One does not expect the loading picture from an ideal blast as shown in Figure 1.1 to be recorded faithfully by the force gage, because certain physical limitations of the system are introduced as a result of its mass, inertia, natural frequency, damping, etc. If the natural frequency of the force gage (and recording instrumentation) is sufficiently high, all details of the loading history will be recorded. Unfortunately, the short duration of the diffraction spike dictates a very high frequency for such a gage---much higher than that frequency permitted by the use of inductance elements. For example, one may expect a 3-inch inductance force gage to have a natural frequency of several hundred cycles per second, whereas a 7,500-cps natural frequency would be required to record the 0.4-msec (about two transit times) diffraction spike faithfully. Thus, through selection of the inductance

pickup as the net-force sensor, the force gage was made incapable of recording the diffraction phase of the loading.

Fortunately, however, the inductance force gage was intended for reading the drag phase only, and the interest in the diffraction loading was limited to its effect on the relatively low-frequency drag gage. That is, even though the drag gage is of too low a frequency to properly record the diffraction phase, this diffraction loading generally exerts a considerable and undesirable effect on the response of the drag gage. Consider, for example, a 3-inch gage with a natural frequency of 200 cps and 1-pound weight of moving parts loaded by a flat-topped shock wave of 4 psi overpressure. An idealized loading picture (see Figure B.1 in Appendix B) would typically consist of a diffraction spike with a peak load of 56.5 pounds (reflected pressure of about 8 psi multiplied by cross section of 7.07 in.<sup>2</sup>), lasting about 0.4 msec (two transit times); followed by a constant drag force of 0.53 pounds (drag coefficient of 0.2 multiplied by q of 0.375 psi multiplied by 7.07 in.<sup>2</sup> area). The analysis of Appendix B considers the diffraction spike so short in duration that the low-frequency force gage sees it as an initial impulse; in this example, the value of the impulse would be about 0.0113 lb-sec (56.5 pounds multiplied by 0.0004 seconds multiplied by a form factor of about 0.5 for the pulse shape), or equal to an initial velocity of 0.364 ft/sec (0.0113 lb-sec divided by a weight of 1 pound multiplied by 32.2 ft/sec<sup>2</sup>). Entering Figure B.4 of Appendix B with

$$\omega V_0 / \bar{y}_0 = (2\pi)(200)(0.364) / (0.53)(32.2) = 26.8$$

and with  $n/\omega = 0.7$  for a well-damped gage,  $\text{read } \omega y_m / V_0 \approx 0.48$ . The peak response of this drag gage would then be 6.8 pounds (peak force  $\omega y_m = \omega y_m / V_0$  multiplied by

$$\omega V_0 = 0.43 \times 2\pi \times 200 \times 0.364 / 32.2),$$

compared with the constant drag load of 0.53 pounds. The drag gage, in this case, would record a spike of 6.8 pounds amplitude which would last about half of the natural period of the gage (for this example, the spike would be over in about 2.5 msec), then several oscillations about a 0.53-pound centerline, and finally a constant reading of 0.53 pound for the rest of the duration of the 4-psi flat top.

Appendix B presents the analysis of the low-frequency system loaded by a short-duration impulse and then a step function. This analysis would appear to indicate that the approach to be followed in order to eliminate the high diffraction spike and subsequent oscillations would be to use a very-low-frequency gage, since this would sharply reduce the amplitude of the diffraction spike. Unfortunately, however, such a gage would not be suitable for use in the available shock tubes, due to the limited duration of flow, and the oscillations following the diffraction spike would last much longer (since each oscillation is about at gage frequency), thus tending to obscure the transition phase for a longer time. As a result of these and other

considerations, the force-gage frequencies were kept as high as was permitted by the inductance pickup design, and all loading effects were studied with a selection of gages of various frequencies.

Several constructive conclusions were reached as a result of the analysis of Appendix B. First, it was deduced that spuriously high drag records would result from an overdamped gage, since the flat-top portion of the record would be obtained while the gage was creeping back from its diffraction spike. Second, it was decided to provide mechanical stops to prevent excessive deflection in response to the diffraction phase. As to the possibility of using drag gages for obtaining information on the diffraction phase, it appears that the only significant data readable is the impulse of this phase. Since this reading depends heavily on the degree of damping, this type of data cannot be expected to be accurate, and it appears desirable to use other gages or other methods for obtaining diffraction data.

6.1.2 The Drag Phase. After the effects of the diffraction phase of the loading have been suppressed through the use of mechanical stops and damping, the force gage may be expected to attain some steady deflection due to drag loading. Both for purposes of gage design and, also, in order to correlate the results of the Teapot effort with previous aerodynamic data, a thorough literature search was made for information on drag coefficients of spheres, on the unproved assumption that those steady-state drag coefficients would be applicable to the pseudo-steady drag phase.

Drag coefficient is a dimensionless number, defined as follows:

$$C_D = F/qA \quad (6.1)$$

where F is the total force exerted by the airstream on the body in the direction of the flow, A is the maximum cross-sectional area presented to the flow, and q is the dynamic pressure equal to  $1/2 \rho u^2$ . It should be noted that for subsonic flow (the Teapot laboratory experiments extend up to about  $M = 0.7$ ) the stagnation pressure  $P_{st}$ , the static pressure  $P_s$ , the dynamic pressure q, and the local Mach number M are related by the following expression valid for an ideal gas with  $\gamma = 1.4$ :

$$P_{st} - P_s = q \left( 1 + M^2/4 + M^4/40 + M^6/1600 + \dots \right) \quad (6.2)$$

The percentage difference between q and  $P_{st} - P_s$  is equal to

$$M^2/4 + M^4/40 + M^6/1600 + \dots$$

Shock Wave Overpressure, $P_s$	M	Difference between q and $P_{st} - P_s$
10 psi	0.36	3.2 %
20 psi	0.58	8.3 %
30 psi	0.74	13.5 %

Since the tests extended only up to about  $M = 0.74$ , the error introduced

into the calculation for  $C_D$  by using uncorrected Rankine-Eugoniot  $q$  was considered acceptable.

Without going into the mathematical and physical background of compressible flow past a sphere, one may search the literature and simply list the significant physical parameters of flow and model which affect the drag coefficient. Although the older literature on wind-tunnel and free-flight performance of spheres indicated that the single flow parameter defining the drag coefficient was Reynolds number, May and Witt (Reference 32) recently recognized the dependence of  $C_D$  on

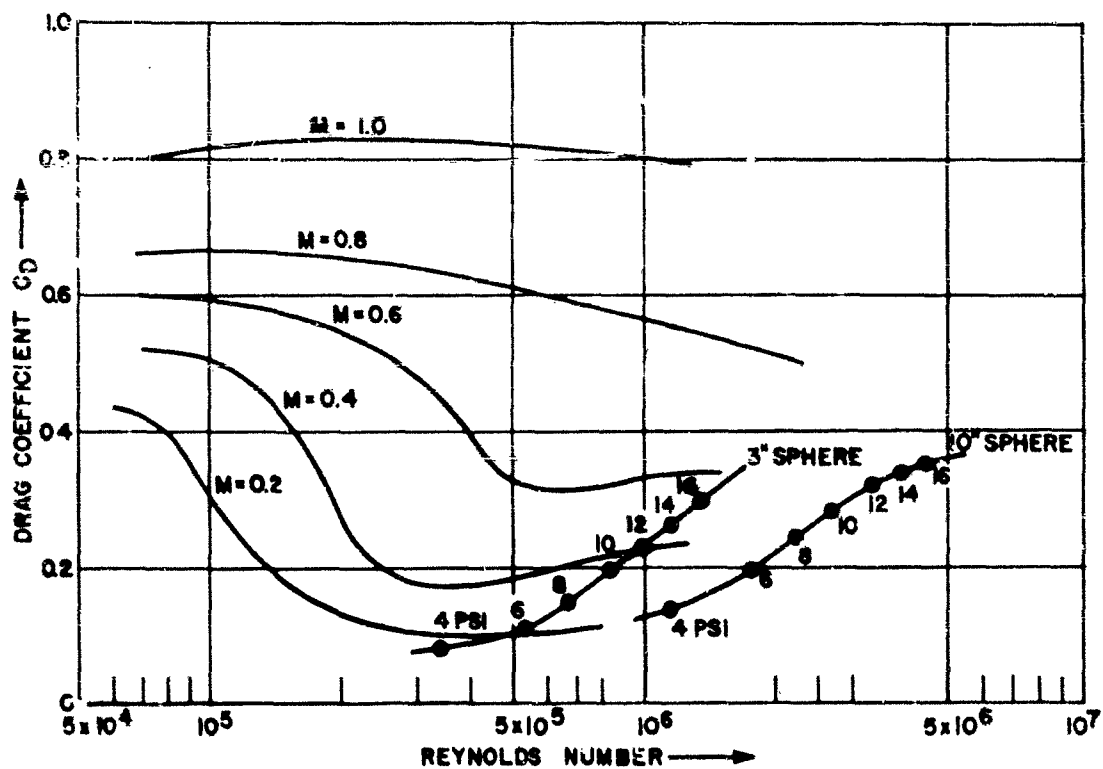


Figure 6.1 Estimated Drag Coefficients of Spheres as Function of Mach Number and Reynolds Number.

Mach number as well as Reynolds number. This additional parameter, however, still fails to remove the tremendous amount of scatter of the wind-tunnel and free-flight data, which is believed due to the sensitivity of the sphere to turbulence in the flow and to miscellaneous influences such as model-surface conditions, sting-size effects and method of support, and even the possibility of effects due to rotation of the free-flight spheres.

Figure 6.1 is a rough summary of the available data on drag coefficient of spheres, lumping together information on sting-supported spheres, free-flight spheres, etc. The superimposed curves represent the shock-wave predictions for the 3-inch and 10-inch spheres, the number on these curves being the side-on overpressures of the shock

wave. Since the published data on drag coefficients of spheres proved to be so scattered and nonreproducible and did not include systematic studies of the effects of such parameters as sting size, surface roughness, etc., it was decided that all effects would be related to the particular models used during Operation Teapot. In other words, comparisons of wind-tunnel, shock-tube, and field data would relate to the identical models of uniform surface conditions, uniform ratio of sting diameter to sphere diameter, and uniform scaled sting length; therefore, Figure 6.1 is of value only for orders of magnitude and for indications of the qualitative effects of Mach number and Reynolds number.

Note the rather sudden drop in the drag coefficients in Figure 6.1 (for the lower Mach numbers) in the range from  $R = 10^5$  to  $R = 3 \times 10^5$ . This region is termed the critical Reynolds-number region, and it marks the transition from laminar flow to turbulent flow in the boundary layer about the sphere. The instability of the flow in this region is such that many parameters of the flow and the model exert a considerable influence on the drag coefficient. For example, increasing the turbulence in the flow or roughening the surface of the model have the effect of shifting the entire curve of drag coefficient versus Reynolds number in the critical region to the left. Since any small shift on this steep curve results in a large change in drag coefficient at a fixed Reynolds number, it is apparent that any small change in test conditions can cause a large change in the drag coefficient measured. Thus, the test setup with apparently well-controlled test parameters may easily yield a large scatter of drag-coefficient data. These remarks apply to the critical Reynolds number region, but they may also be applicable to the region under investigation in the Teapot laboratory program.

6.1.3 Effects of Dust. Theoretical attempts to predict the flow patterns of particle-laden air around obstacles have been made by Langmuir and Blodgett (Reference 33), Dussourd and Shapiro (References 34 and 35), and Hartmann (Reference 36). Langmuir and Blodgett assumed a flow pattern for the air around cylinders, spheres, and ribbons. Then they calculated the particle trajectories by assuming Stokes' drag law for spherical particles. Their results indicate dependence of loading on particle size and density, air density, viscosity and velocity, and obstacle size. Hartmann's novel approach is based on the response of particles to sound waves of different frequencies---the frequency here depending on the time for a particle to displace itself laterally in order to get past the obstacle. His results depend on the above-mentioned properties of air, particles, and model. The work of Dussourd and Shapiro is applied to the problem of an instrument for measuring stagnation pressure and velocity of a particle-laden gas stream.

Hartmann points out that the dusty air may be taken as a homogeneous fluid of uniform density (somewhat greater than clean-air density) if the particles are small enough and follow the air stream-lines closely enough. His estimates indicate that particles 5 microns or less in radius would fulfill these requirements (for the Teapot model sizes).

For such a situation, one would record the increased density on the q gage as an increase in dynamic pressure, and the drag coefficients should be the same as clean-air drag coefficients at corresponding Mach and Reynolds numbers.

However, if the dust particles do not follow the air-stream lines, some of them impinging on the model surface, there exists the serious problem of how to separate the effect of the dust from the total-force reading. The problem is further complicated by the fact that the effect of dust on the reading of the q gage (analyzed by Dussourd and Shapiro) is far from a simple matter; it depends not only on properties of air and dust but also on tube diameter and size of sampling hole. For example, Dussourd and Shapiro find that the measured overpressure increases as probe size increases and as the ratio of inside to outside diameter decreases, no account having been taken of possible impingement effects of those solid particles actually entering the hole.

This formidable dust problem has been investigated experimentally by the Sandia Corporation and others (Reference 31), but no simple solution has resulted. For this reason, the Teapot planning on the dust problem was not predicated on the solution of the problem but was based, rather, on the philosophy of obtaining field data under reproducible conditions. SRI gages were used as the standard q gage to read dusty q as best they could (other activities investigated other q-gage designs, such as Greg and Snot), and dust density was measured. In this way it was hoped that the entire dust question could later be studied under controlled laboratory conditions. And if no consistent theory could be found for the flow behavior of dust, at least one would have the gross loading effects on 3-inch and 10-inch spheres to serve as a measure of the damaging effects of the precursor.

## 6.2 MECHANICAL DESIGN

Early in the laboratory phase of the program, it was determined that the objectives of the project could be met only if a suitable force gage could be developed. Gages available commercially and laboratory designed force gages were found unsuitable for the task. They were either incompatible for use with the desired recording system, too delicate for field use, or too limited in performance characteristics. An initial study of the force-measuring problem indicated that it would be desirable to have a gage that would: (1) measure force in three mutually perpendicular directions with negligible interaction between axes; (2) be rugged enough for field work, yet be suitable for wind-tunnel and shock-tube tests; (3) have a frequency response adequate for measuring faithfully the complete force-time history during the blast; (4) employ a variable-inductance sensing element so that the gage could fit directly into the existing recording system; and (5) be adaptable for use with model targets of different sizes and shapes.

The gages finally developed for Operation Teapot did not completely fulfill the above requirements; however, they were deemed satisfactory for the task imposed.

6.2.1 Schaevitz Gages. The Teapot force gage was designed and developed by the Schaevitz Engineering Company of Camden, N. J., with the aid of NOL. The principal feature of the gage is a mechanical system that provides three independent and orthogonal axes, each of which restrains the model motion to translational displacements only. The restraining force of each axis is provided by a pair of folded cantilever springs that can deflect only in a direction perpendicular to the plane of the spring when a force or a component of force is in that direction. Because of the great stiffness of the spring in response to forces in other directions, the springs themselves are used as rigid supports for the structural members of the other two axes. In this way, the orthogonal components of a vector force acting on the gage influence only the respective rectilinear axes of the gage. This action may be illustrated by reference to the schematic gage diagram in Figure 6.2 (see also Figure 6.3).

Consider a model target, be it sphere or cylinder or jeep, rigidly mounted on the enclosing Frame 1 (Figure 6.2). Apply a force to this model in the Z-direction. The rigidity of Springs 2' and 3' to edgewise forces prevents motion of Frames 2 and 3 with respect to reference Frame 4. However, with the application of this Z force, Springs 1' flex around the now fixed adjacent Frame 2. Therefore Frame 1 moves with respect to Frame 2 and, hence, reference Frame 4. Now consider a force in the X direction. The force on the model is transmitted to Frame 1. Springs 1' are rigid for forces applied in this direction; therefore, the force is transmitted through supporting members to Frame 2, which (along with Frame 1) can now move in the X direction because Springs 2' flex around the fixed Frame 3 (which is restrained from moving with respect to the fixed reference Frame 4 by Springs 3'). Thus, when forces are applied in the X direction, two frames, moving as one, are displaced with respect to the fixed reference frame. Forces in the Y direction produce results similar to those above. A Y force applied to Frame 1 is transmitted through rigid Springs 1' to Frame 2, from whence the force is further transmitted to Frame 3 through rigid Springs 2'. Frame 3 can move in the Y direction because of the deflection of Springs 3' around the fixed reference Frame 4. Thus, for forces in the Y direction all three frames move as one with respect to the fixed reference frame.

Summarizing, this mechanical arrangement of springs and frames produces a gage system which responds to force and the vector components of force in terms of translational displacements along three orthogonal axes. These displacements, which are proportional to the magnitude of the applied force, are converted into electrical signals by the variable-inductance sensing elements of the gage. Affixed to each of the movable frames is a mu-metal disc in close proximity (0.010-0.015 inch, this distance being a function of the inductance-distance characteristic curve of the particular type of disc and coil combination, selected on the basis of minimizing the nonlinearity of the force-frequency curve) to an E-core inductance coil mounted on the fixed reference frame. Variations in the gap spacing between disc and coil produce variations in the inductance of the coil. (Lateral motion between disc



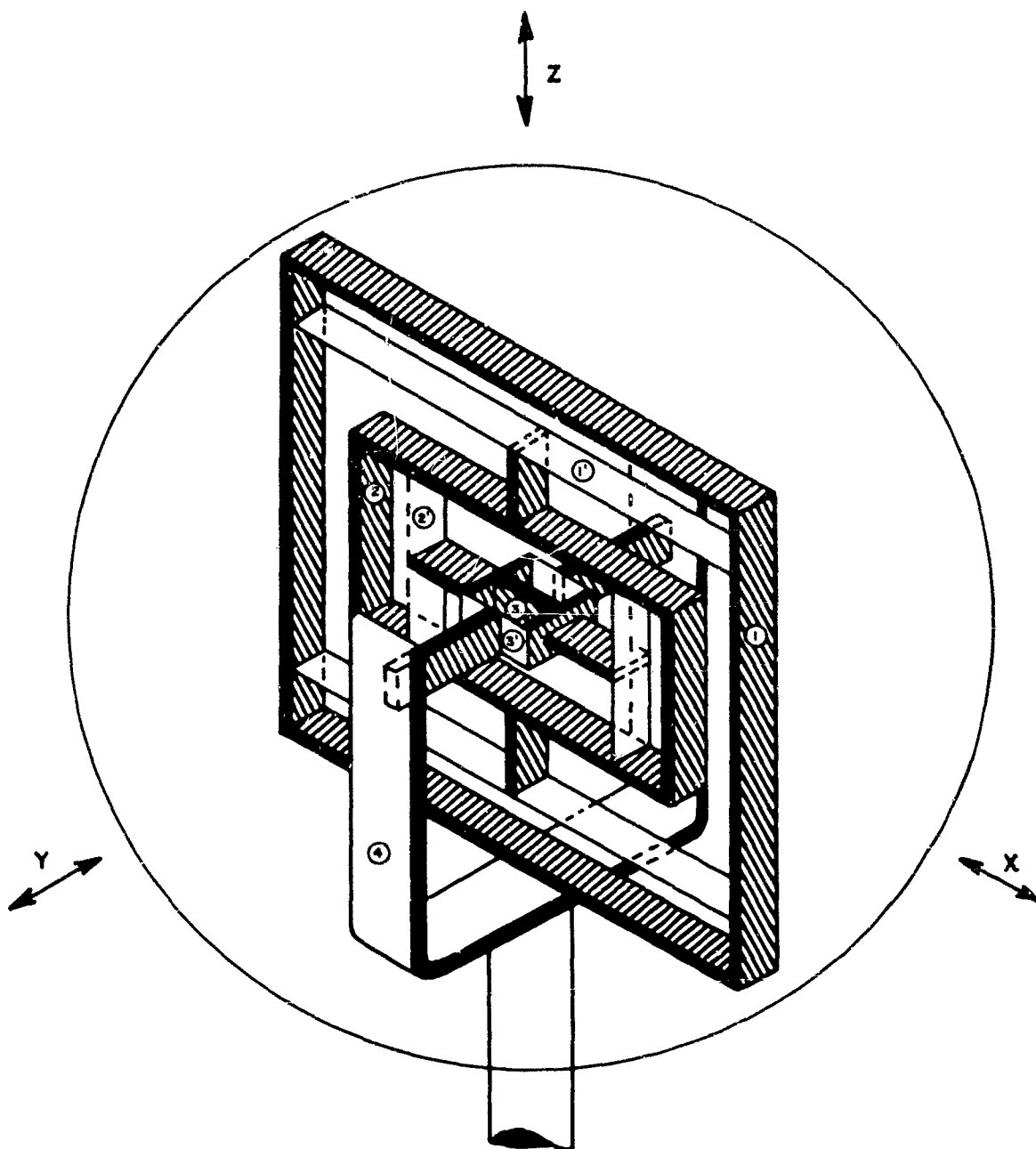


Figure 6.2 Schematic Diagram of Three-Component Force Gage.

and coil produces negligible inductance change, since the gap spacing remains constant and the disc is of larger diameter than the E-core.) The inductance variations modulate the center frequency of a Hartley oscillator. This electrical signal is then transmitted and recorded as the gage signal for a particular axis. Each of the three axes has its independent disc and inductance-coil sensing unit.

The convention adopted for signal identification was X axis on the 7.35 kc band, Y axis on the 10.7 kc band, and Z axis on the 15.4 kc

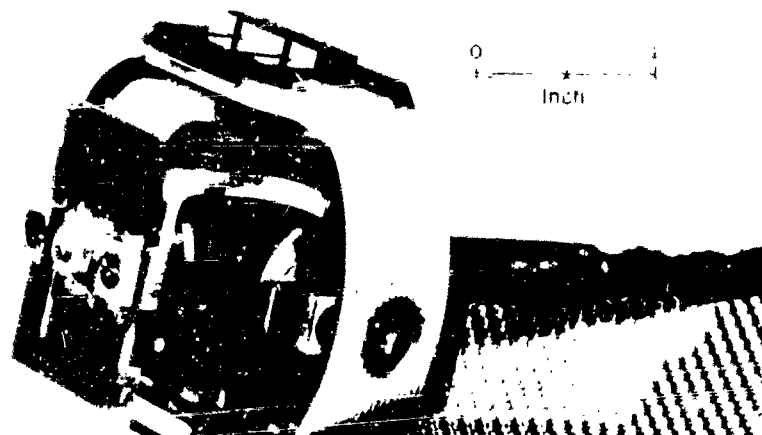


Figure 6.3 Prototype Model of Schaevitz Gage.

band. A force in the positive direction (see Figure 6.4) produces a decrease in frequency below the above center frequencies, while a force in the negative direction produces an increase in frequency.

Associated with the problem of a force-gage design was the problem of designing a support for the gage. The wind-tunnel type of horizontal sting was adopted for this purpose. Conventionally, for proper evaluation of the aerodynamic properties of a model without sting interference, the supporting sting should be approximately 10 times as long as the model diameter, and its diameter should be only a tenth of the model diameter. Unfortunately, these conservative sting dimensions could not be used for the conditions anticipated in the field. In the dusty precursor region, it was estimated that the force on a given target would be about four times greater than on a similar target in a clean

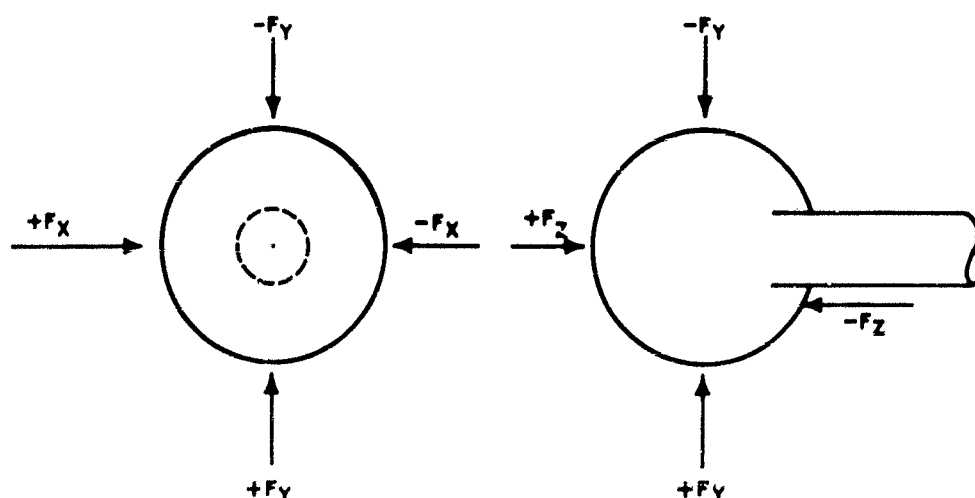


Figure 6.4 Convention for Direction of Force.

area at an equal static-overpressure level. The latter wind-tunnel-like conditions permit slender stings; the former situation dictates, on a structural strength basis, the use of relatively short, stubby stings. As a consequence, stings with the following dimensions were used:

3-inch diameter spheres - sting length 9 inches,  
sting diameter  $7/8$  inches; 10-inch diameter spheres -  
sting length 30 inches, sting diameter 3 inches.

Shock-tube tests indicated the adequacy of this design without the need for bracing. The fixed reference frame of the gage is rigidly attached to the sting, and of course, the spherical model encasing the gage is free to move with respect to the sting (see Figures 6.5 and 6.6).

6.2.2 Bellows Gage. During the course of the gage-development program, several other designs were considered besides the one finally adopted. One particularly promising design, initiated by the Aeroballistics Research Department of the Naval Ordnance Laboratory, employed metal bellows (one pair for each orthogonal axis) to support the model target from within (see Figures 6.7 and 6.8). One end of each bellows is rigidly attached to the model sphere, while the other end is fixed to a central reference block mounted on the sting. The bellows are designed to operate in compression, tension, and in bending. Their cylindrical cross section is essentially rigid in torsion. In this way, forces on the sphere produce only translational motions of the sphere. Interactions between axes are intended to be minimized by selection of bellows elements to be as identical as possible, thus avoiding any sideways motion of a pair of bellows when placed in bending. The variable-inductance sensing elements of the gage respond to displacements in the same manner as for the Schaevitz gage. The performance characteristics of this gage are similar to those of the Schaevitz gage. The chief drawback of the bellows gage is difficulty of manufacture and adjustment. A prototype model of the gage was used on Shot 12 at the same location where four Schaevitz gages were placed.

6.2.3 Diaphragm Gage. Another design, which was carried partly through the development state, was a diaphragm gage. Figure 6.8 shows that the diaphragm has its outer rim fixed to the sting. Axial forces on the spherical shell produce deflection of the diaphragm; this motion is detected by the coil mounted in the sting. Transverse loading (in the plane of the paper) produces a twisting moment on the diaphragm, which induces an angular deflection at the center of the diaphragm (with no net axial motion); this, in turn, is translated into an angular deflection of the stem between model and diaphragm. Motion of the stem is detected by the fixed coil mounted adjacent to the stem. Transverse loading in the third orthogonal direction, normal to the plane of the paper, is similarly detected by a third coil mounted adjacent to the stem. Development of this scheme was abandoned when it was realized that the accuracy of the transverse readings depends on the load being applied through the center of the sphere (since the torque produced by

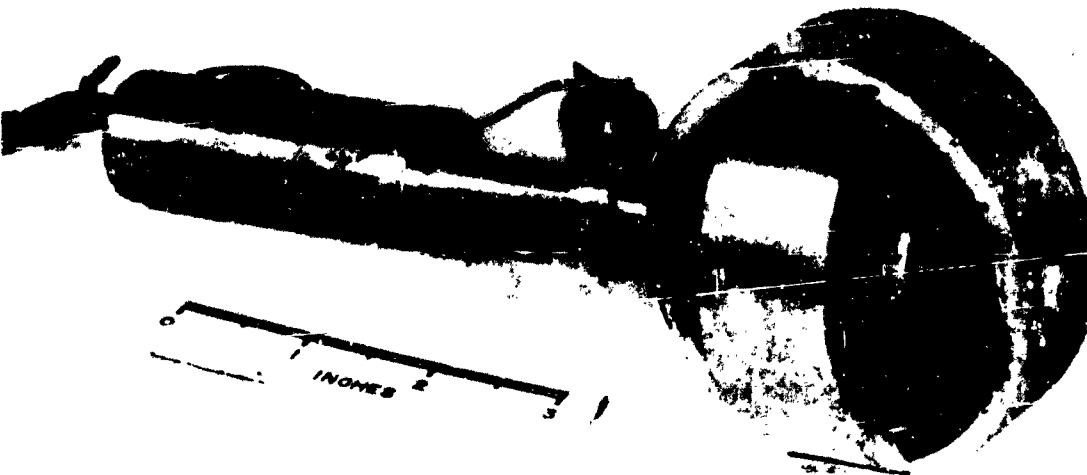


Figure 6.5 Three-inch and  
10-inch Schaevitz Gages  
Without Shells.



Figure 6.6 Ten-inch Schaevitz  
Gage with Spherical Shell.

Figure 6.7 Prototype Model  
of Bellows Gage.



the load depends on the moment between diaphragm and line of action of load) and that, due to the presence of a sting, one could not expect the aerodynamic net load to always pass through the geometric center of the sphere.

**6.2.4 Cylinder Gage.** Another prototype model used on the field test was selected with a view toward circumventing the problem of sting effect on the aerodynamic performance of the model and making more-direct use of available wind-tunnel and shock-tube data on the aerodynamics of simple bodies. The general scheme, proposed by H. H. Kurzweg of NOL, is to include a movable test section as an aerodynamic part of a much-longer cylinder. Two advantages are achieved: no sting interference and practical use of a two-dimensional

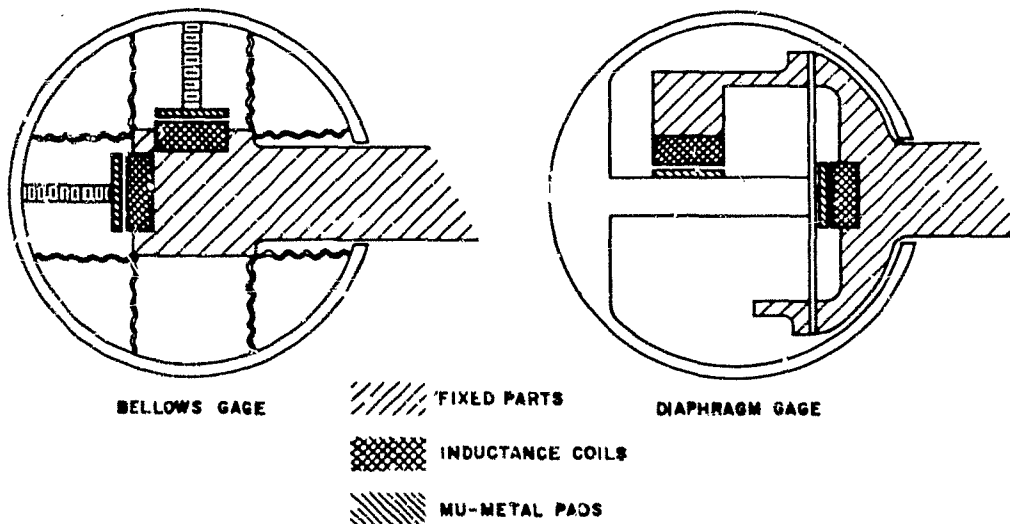


Figure 6.8 Schematic Drawings of Bellows Gage and Diaphragm Gage.

model without end interference. Aerodynamic considerations require that the fixed cylinder be about 10 times as long as the test section, which, because of its inherent mechanical weakness, imposes the limitation that this type of gage be used in relatively low-pressure regions. However, just as in the case of the stings for the spherical models, some compromise in this conservative length-ratio criterion could be made, with appropriate empirical corrections to the data when necessary. The prototype used on Shot 12 was of circular cross section, 6 5/8 inches in diameter; the model section was 6 inches long, the fixed pipe 12 feet long. The pipe had its axis horizontal and at right angles to ground zero, 3 feet above the ground. The test section contained a Schaevitz gage modified to read vertical components and components along a radius from ground zero (see Figure 2.8).

### 6.3 MECHANICAL PERFORMANCE OF THE FORCE GAGE

**6.3.1 Gage Frequency, Damping, and Calibration.** Consideration of the loading picture and its effect upon the physical gage and sensing

system resulted in the following design aims: (1) maximum mechanical frequency to best "read" the forcing function; (2) mechanical stops to prevent excessive deflection during the diffraction phase; and (3) damping, sufficient to suppress undesirable oscillations but not enough to prevent the smoothed record from having followed the forcing function. (About 60 percent of critical damping is optimum for the second order system with damping force proportional to velocity.)

As has been mentioned in the introduction, the natural frequency of the gage-model combination has automatically been limited through the selection of the induction-type pickup, since this induction-coil design calls for a large deflection to produce the desired frequency shift along the most-linear portion of its calibration curve (inductance, or frequency shift, versus deflection). To illustrate this effect, consider a 3-inch model sphere of nominal force range 25 pounds, the moving parts weighing 1 pound, the inductance gage calling for 0.005-inch deflection. Spring constant,  $k$ , is defined as:

$$k = \frac{\text{force}}{\text{deflection}} = \frac{25}{0.005} = 5000 \text{ lb/in.}$$

Natural frequency,  $f$ :

$$f = \frac{1}{2\pi} \sqrt{\frac{k}{M}} \quad (6.3)$$

for  $W = Mg = 1 \text{ lb}$

$$f = \frac{1}{2\pi} \sqrt{\frac{5000}{1}} \quad (386) = \underline{221 \text{ cps}}$$

This analysis predicts, for models of equal mass, that the higher the force range the higher the natural frequency, and this has been found true for the Teapot gages. For the 3-inch gages, with nominal force ranges extending from 3 to 100 pounds, the gage frequencies ranged from about 150 to 600 cps, respectively. The 10-inch gages, with rated force ranges from 35 to 400 pounds, had frequencies extending from 100 to 400 cps, respectively. These frequencies proved adequate for the long-duration field blast and for shock-tube wave durations of 30 msec or longer (with well-damped gages).

Fluid damping was used to limit the magnitude and duration of the gage "ringing" induced by the application of a shock pulse. Silicone fluids, with viscosities from 1,000 to 1 million centistokes were used inside the spherical shell and were prevented from leaking out by the sealing of the space between moving shell and fixed stinger with Pliobond, a flexible sealing agent. The models were only partially filled, to avoid the differential expansion problem. This technique of filling the shells with silicone fluids proved to be a messy affair, since a change of fluid viscosity, to achieve empirically a better damping coefficient, called for thorough cleaning of the close-fitting gage parts. A much simpler and more-controllable technique of filling only the space between the mu-metal pad and coil was used under laboratory conditions. This technique could not be used in the field because the fluid could not be

expected to remain in place for the long periods required (several days, usually).

No special design provisions had been made for damping the Teapot gages, with the result that the damping characteristics were not of the viscous shear type, proportional only to velocity. Instead, due to the action of squeezing the fluid out laterally from between close clearances, the damping turned out to be dependent on displacement and velocity, as may be seen in Figure 6.9. Note that some small oscillations persist even when the "smoothed" centerline exhibits creep or overdamping; whereas, the viscously overdamped gage would have no oscillations.

This behavior had two consequences: First, it was not legitimate to calculate damping from the decay of the small oscillations, which made

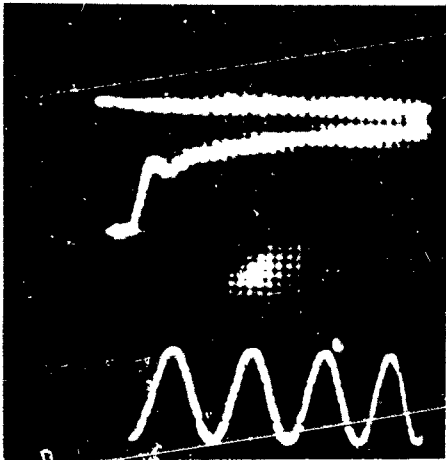


Figure 6.9 Response of an Overdamped Schaevitz Gage to a Step Function (200 cps Timing).

the tap test (or impulse test) useless for determination of damping coefficient and led to the need for the more-difficult step-function test. Second, and more serious, this deviation from viscous damping made any attempt to use the drag gages for some measure of diffraction loading practically hopeless. It is apparent, at any rate, that the design of the Teapot gages left room for much improvement in damping characteristics.

Consideration had been given to the possibility of and need for damping of the sting support of the gage should this vibration prove to be a source of "noise" on the force records. Fortunately, it was found (through shock-tube tests) that the stings were of sufficient rigidity to contribute little to the hash, amplitude-wise. Further, the distinctive sting frequencies\* were relatively easy to identify and

---

\* The 7/8-inch-diameter sting with the mass of the 3-inch gage had an average frequency of about 100 cps; the 3-inch diameter sting with the mass of the 10-inch gage vibrated at approximately 160 cps; and the entire mounting structure with the mass of the 10-inch gage was found to have a natural frequency of 20 to 30 cps.

interpret. Record smoothing proved to be a more satisfactory method than attempts to damp each possible source of vibration.

Static gage calibrations (and dynamic gage characteristics) were observed and recorded. The static force-frequency curve was determined by the use of a calibration rig (see Figure 6.10). The step force function used for the determination of dynamic damping characteristics was achieved by sudden release of a known force. Figure 6.11 is a photograph of the setup for the force gages rated at 25 lb or less in range, the sudden release occurring when a pencil lead under tension is snapped. The rig for the higher force gages employed a quick-release mechanism that was manually tripped. Figure 6.12 represents a typical static calibration curve, and Figure 6.13 is a picture of a gage with optimum damping.

6.3.2 Reproducibility and Accuracy. The static and dynamic calibration of the gages, determined by applying known forces to the gage and observing its output, gave a fair indication of the total static and dynamic accuracy of the gages. Wind-tunnel and shock-tube tests with reproducible forcing functions gave an indication of the degree of reproducibility of the gages to dynamic and transient loading conditions. (It should be understood that wind tunnel and shock tube tests were not used to provide basic gage calibration data. Rather, they were used to determine gage behavior under steady state and transient aerodynamic loading conditions.)

In the static calibration procedure, the reproducibility and hysteresis of each axis was observed, as was the interaction amongst axes. It was found, at the nominal range of the gage, that the discrepancy in response due to hysteresis and nonreproducibility averaged approximately 10 percent of the nominal range, i.e., a gage with 100-lb range read  $100 \pm 10$  pounds when a known 100-lb force was applied to it. This same uncertainty occurred on the average at all force readings of the particular gage. A variation of about  $\pm 5$  percent occurred also in the results produced by the transient loading of the gage in shock tube tests. A much-greater spread occurred in wind-tunnel tests; however, this was believed due to aerodynamic conditions, rather than force-gage performance.

Some interaction occurred between sets of gage axes; for instance, when the gage was loaded along the Z axis only, the X and Y axes gave indications that the Z applied force had X and Y components. These interactions and spurious readings amounted to approximately 10 percent of the applied load in some gages and axes and less than 5 percent in others. Since interactions were noted in the gage-calibration procedure, corrections to the data could be applied had they not been negligible.

Based on the static and dynamic calibration data (including hysteresis effects, reproducibility checks, calibration technique, and equipment accuracy), it is estimated that the force gage is capable of producing force readings on the three orthogonal axes within  $\pm 15$  percent of the applied vectorial force. Error in prediction of the angle of flow by means of an analysis of static vectorial forces depends on the aerodynamic effect of the sting.

6.3.3 Performance of the Gage in a Pressure Field. Instead of acting as sensor only for the net force due to flow past the model, the



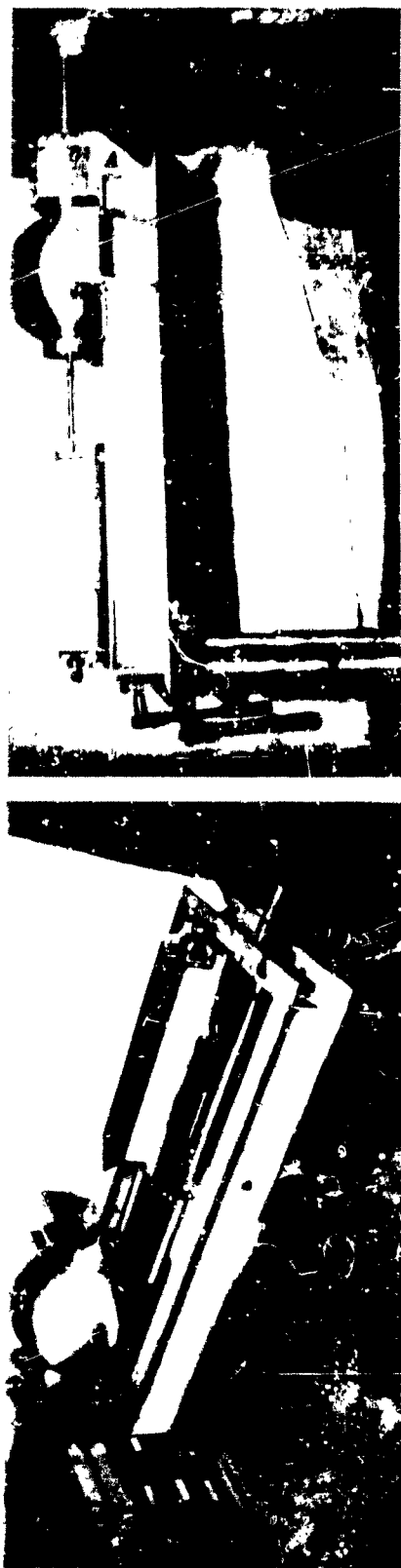


Figure 6.10 Ten-inch Force Gage in Static Calibration Rig.



Figure 6.11 Quick-Release Device for Step-Function Test  
on 24-in. Characteristics of 3-inch Force Gage.

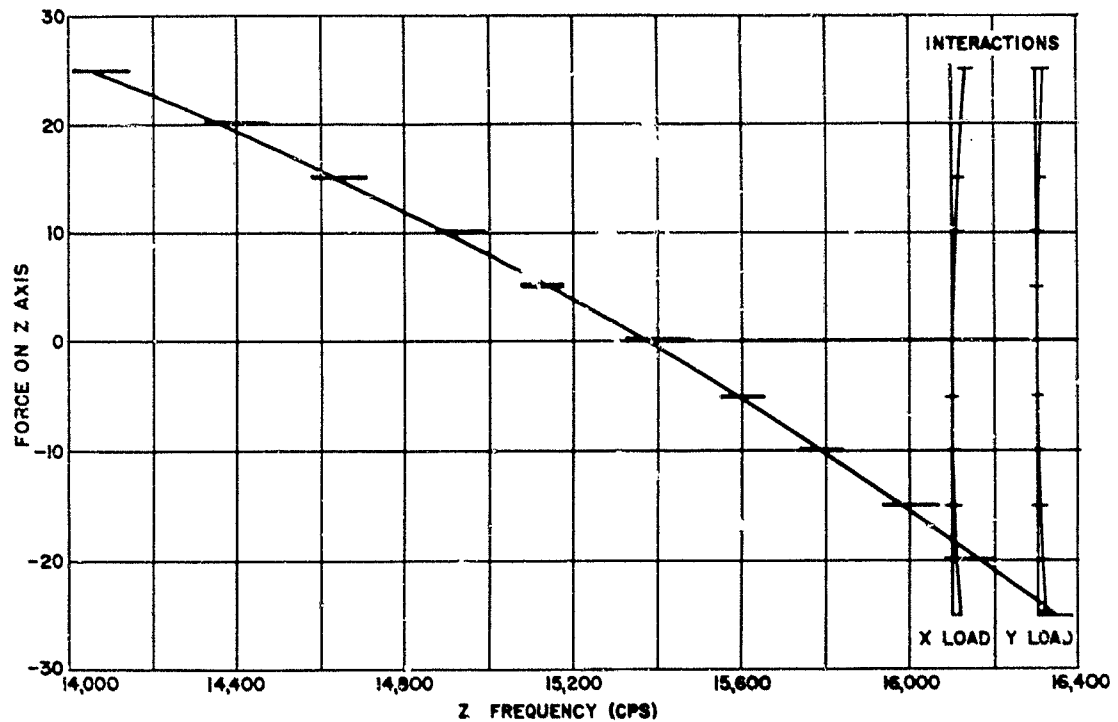
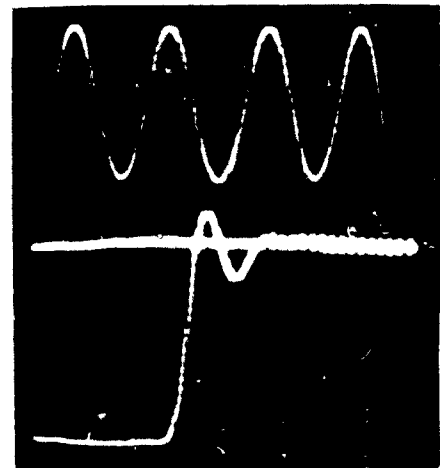


Figure 6.12 A Typical Static Calibration Curve.

Figure 6.13 Response of a Well-Damped Schaevitz Gage to a Step Function (200 cps Timing).



Teapot configuration of a force gage inside a sting-supported model proved to be sensitive also to the static pressure in the free stream of fluid. That is, for the same flow property of dynamic pressure and for the same drag coefficient, the Teapot force gage responds to shock-tube flow with its static overpressure in a manner quite different from its response to wind-tunnel flow with its static pressure below atmospheric. The reason for this behavior is as follows:

Consider the forces on the shell of Figure 6.14, where the shock wave is broken down into a static field of side-on pressure and a dynamic field resulting from the presence of the obstacle in the flow,

the loading on the obstacle being proportional to  $q$  and depending on its geometry (drag coefficient and area). In calculating the axial forces on the shell due to static pressure, it becomes apparent that there is a net force of  $P_i a$  caused by the internal pressure,  $P_i$ , and a net force of  $(P_o + P_s)a$  due to external pressure (ambient pressure,  $P_o$ , plus shock overpressure,  $P_s$ ). These net forces are due to the fact that the sting area,  $a$ , occupies some of the shell area which would otherwise be exposed to static pressures. The summation of these net forces in

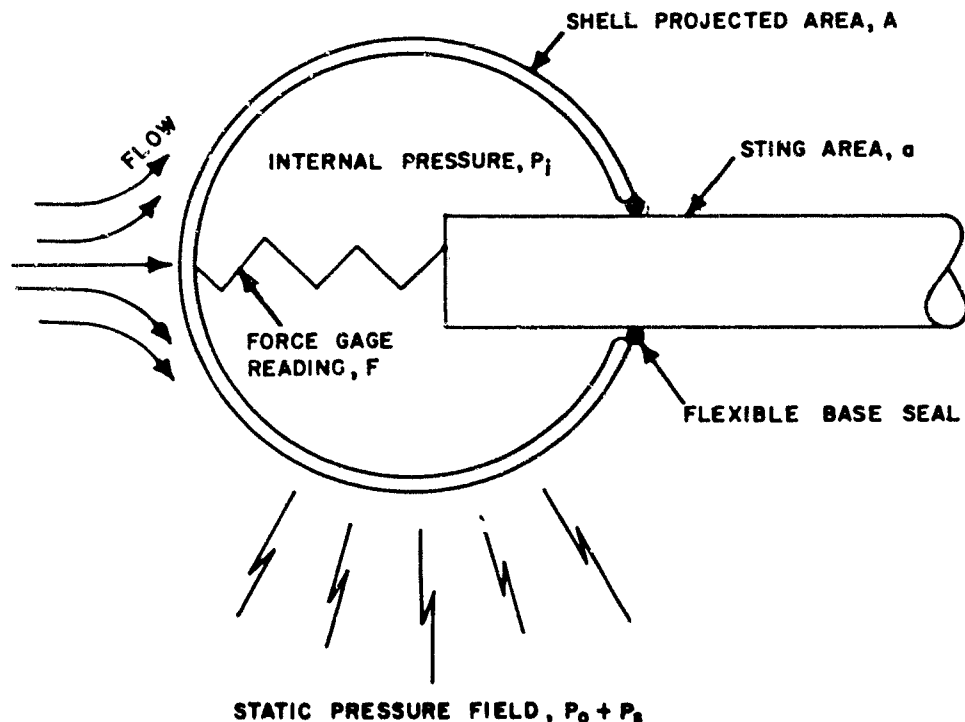


Figure 6.14 The Force Gage in a Shock Wave.

opposition leads to a force of  $(P_o + P_s - P_i)a$  directed toward the sting. The equation for force, including the effects of flow and of static pressures, is thus:

$$(P_o + P_s - P_i)a + qC_D A = F \quad (6.4)$$

If the internal pressure,  $P_i$ , remains constant during the loading period and is different from  $P_o$ , there is an initial load of  $(P_o - P_i)a$ . The dynamic reading would be  $F - F_o = \Delta F$

$$\Delta F = F - (P_o - P_i)a$$

$$\Delta F = qC_D A + P_s a$$

Thus it appears that the magnitude of the internal pressure is of no importance, providing that it does not change from its initial value. If it did change, one would have to know the initial value and its

variation with time, in order to interpret a record for force-gage reading versus time. Rewriting Equation 6.5:

$$C_D = \frac{\Delta F}{qA} - \frac{P_s}{q} \frac{a}{A} \quad (6.6)$$

The correction to the usual equation for drag coefficient  $\left(\frac{P_s}{q}\right)\left(\frac{a}{A}\right)$ , may appear insignificant at first glance, because  $A \gg a$ . For the 3-inch spheres,  $\frac{a}{A} = \left(\frac{0.875}{3.00}\right)^2 = 0.085$ , and for the 10-inch spheres

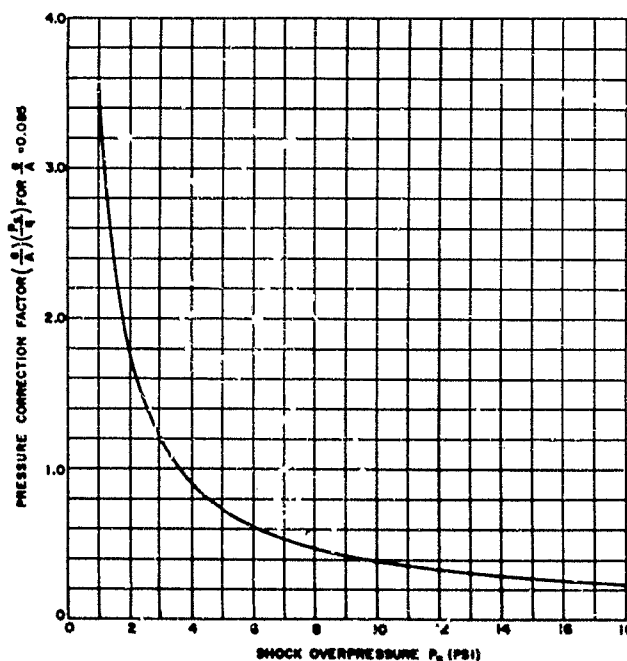


Figure 6.15 Increase in Apparent Drag Coefficient Due to Effect of Static Pressure on a Perfectly Sealed Gage.

$\frac{a}{A} = \left(\frac{3}{10}\right)^2 = 0.090$ . Unfortunately, however, the ratio  $P_s/q$  attains very-high values at low overpressures, and the factor  $\left(\frac{P_s}{q}\right)\left(\frac{a}{A}\right)$  becomes

of the same order as  $\Delta F/qA$  at low pressures. Force readings in the shock tube at low overpressures resulted in drag coefficients as high as 10 when used without correction in the formula  $C_D = F/qA$ .

Figure 6.15 consists of a plot of  $\left(\frac{P_s}{q}\right)\left(\frac{a}{A}\right)$  for  $\frac{a}{A} = 0.085$  where  $p$  and

$q$  are related by Rankine-Hugoniot conditions. Note the magnitude of the correction compared with the expected drag coefficients of about 0.3. Since this correction appeared so large, it was necessary to obtain experimental verification of the effects of static pressure.

In order to study the static-pressure effects, the pressure-step device illustrated in Figure 6.16 was employed. Air was admitted to

the compression chamber until the desired pressure was reached, and then the diaphragm was punctured. Thus, pressure was suddenly applied to the chamber containing the force gage, at a level of about half the original compression chamber overpressure, and remained essentially constant for a long enough duration to be considered a step function. The force gage oscillated violently until the flow stopped and the pressure equalized, a matter of some 20 to 30 msec, and then indicated a more or less constant force (ideally  $F = aP_s$ ), depending on the rate of leakage of pressure into the gage shell.

Figure 6.17 consists of two force gage records of a well-sealed gage, and Figure 6.18 shows the force decay of a poorly sealed gage.

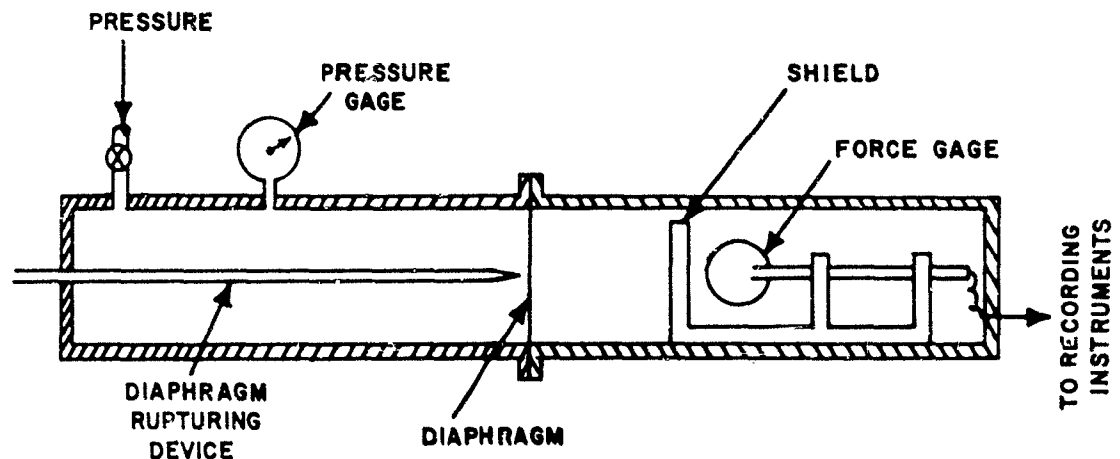


Figure 6.16 Mechanism for Applying Step-Function of Pressure to a Force Gage.

The information obtained from these pressure-step tests was the effective sting area to be used in Equation 6.6 and the rate of leakage of pressure into the shell of the gage.

Figures 6.19 and 6.20 represent the performance of two well-sealed gages loaded by the pressure step. Effective sting area shows some scatter (due to experimental error, method of sealing, etc.), but remains close to the actual sting area of 0.60 in<sup>2</sup>. Force appears to decay slowly, relative to short duration shock tube flows, such that less than 15 percent decay occurs in 200 msec. These well-sealed gages appear amenable to correction in accordance with Equation 6.6.

Figure 6.21 indicates the difficulty of dealing with a poorly sealed gage, which was sealed using the same method as for the well-sealed gages. Force decay, obtained from records such as Figure 6.21, extrapolated to zero time through the initial oscillations, seems to be about 50 percent in 200 msec. Note, however, that the effective area appears to be much smaller than the actual sting area. This phenomenon is probably due to a rapid leakage during the first 20 to 30 msec of violent pressure changes. Such a gage would not be reliable even for shock-tube flows as short as

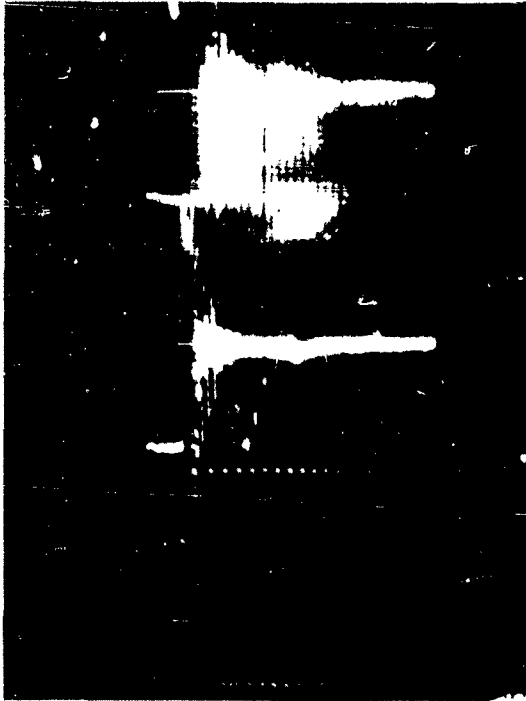


Figure 6.17 Response of a Well-Sealed Gage to a Step Function of Pressure. Shot 6, 7; Gage No. 18; 60-cycle Timing;  $P_s = 6.0, 6.1$  psi;  $F = 3.6, 3.8$  Pounds.

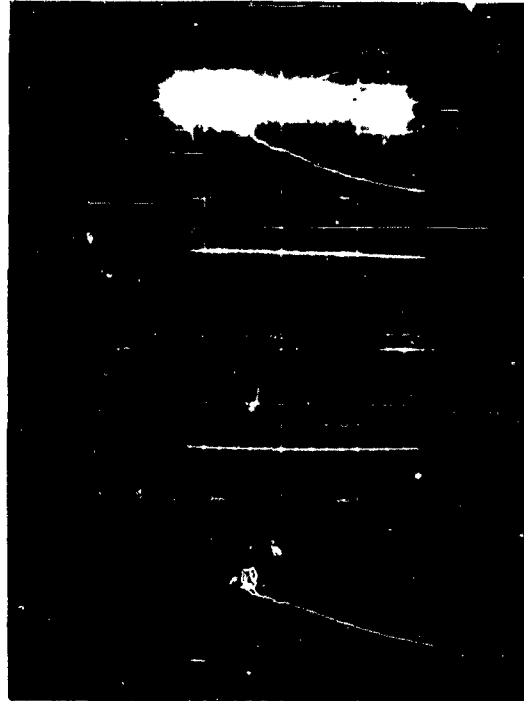


Figure 6.18 Response of a Poorly Sealed Gage to a Step Function of Pressure. Shot 16, 17; Gage No. 10; 60-cycle Timing, At Zero Time:  $P_s = 3.70, 3.80$  psi;  $F = 0.2, 0.2$  Pounds. At 200 msec:  $P_s = 3.5, 3.4$  psi;  $F = 0.1, 0.1$  Pounds.

30 msec, since there could be considerable leakage even in the 5 msec while the gage is settling down to the approximately flat-topped drag phase.

Experiments with the pressure-step device of Figure 6.16 were confined to the three 3-inch-diameter force gages that were used for the laboratory phase of the Teapot force program. Many of the other 3-inch gages used on Shot 12 had been damaged by solid particles in the blast and were not suitable for a check on their pressure characteristics, while the 10-inch-diameter spheres had been deliberately vented (approximately 1 inch of the circular Pliobond seal left off at the top of the sting) for field use. Thus it was not possible to check the leakage characteristics of each gage as used in the field. The conclusions to be reached in regard to gage condition in the field appear to be that some of the gages were well sealed for long durations (in which case Equation 6.6 is applicable), others were sealed for only a short part of the shock wave duration (due to leakage at the sting and also puncture of the shell by solid particles), and still others leaked rapidly enough to be considered unsealed.

Interpretation of the force records of a rapidly leaking gage is possible, since information is available on the pressure distribution

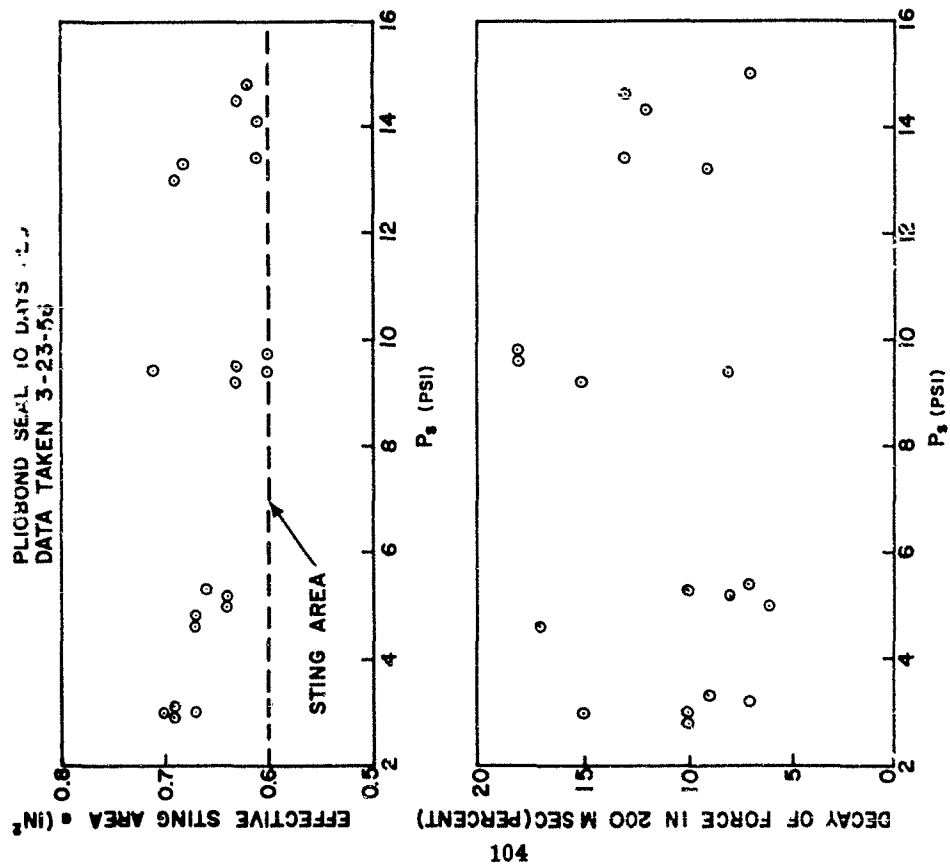


Figure 6.19 Response of Gage 11 (3-inch, 25-pounds) to Step-Function of Pressure.

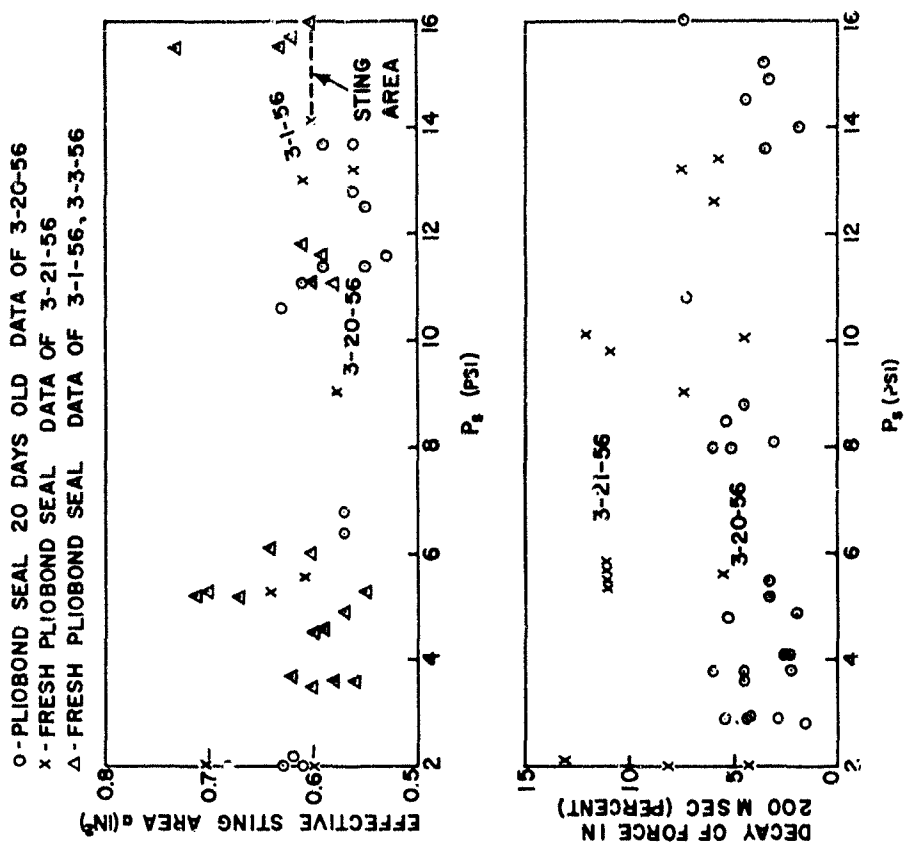


Figure 6.20 Response of Gage 18 (3-inch, 15-pounds) to Step-Function of Pressure.

CONFIDENTIAL

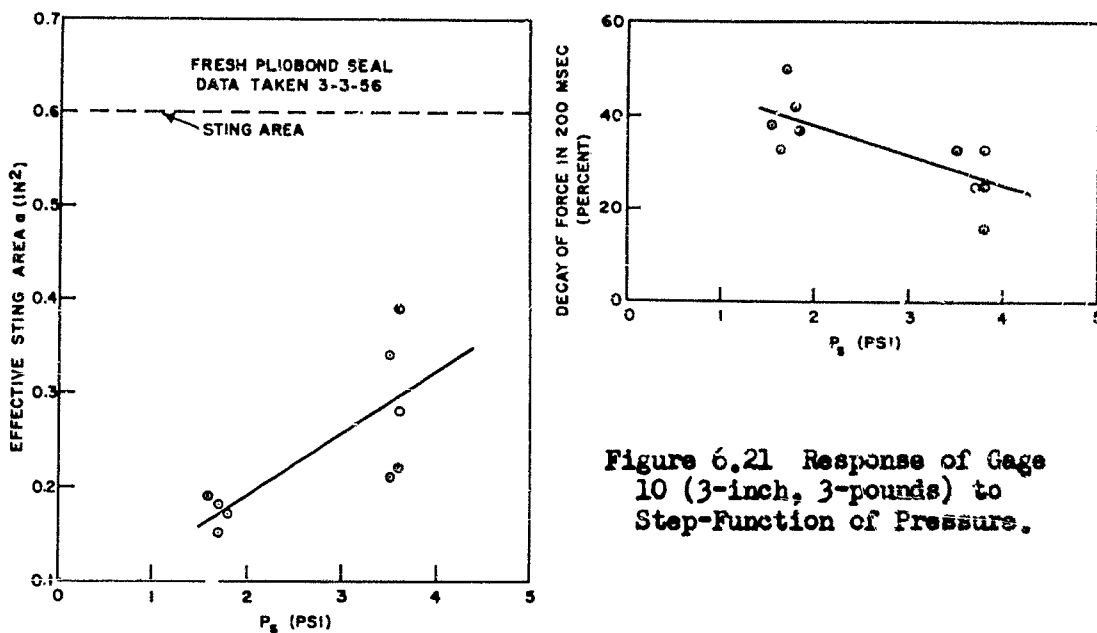


Figure 6.21 Response of Gage 10 (3-inch, 3-pounds) to Step-Function of Pressure.

which exists about the sphere, and one may predict the possible variations of pressure which can leak into the spherical gage. Figure 6.22 illustrates the pressure distribution about a sphere in steady flow. Pressure is reported as the difference between measured pressure ( $P$ ) and static pressure ( $P_0$ ), divided by  $q$ . This ratio of  $P - P_0$  (or  $P - P_s$  in shock wave notation) to  $q$  varies from 1.0 at the stagnation point to about -1.2 near the hemisphere to some small value (+0.2 to -0.3) at the sting. If the shell leaked at its hemispherical joint, the internal pressure would be some  $0.4q$  to  $1.2q$  below  $P_s$ . If the shell leaked at the junction with the sting, the pressure would be about  $0.2q$  above  $P_s$  to about  $0.3q$  below  $P_s$ , depending on Reynolds number. If the leakage took place through the sting, which had an axial hole for electrical leads, the maximum pressure could run as high as  $P_s + q$ , since this represents the maximum, or stagnation, pressure.

Experimental information on the actual pressure inside the 10-inch gages was obtained in the wind tunnel at David Taylor Model Basin, by the use of pressure gages inside the model. The wind tunnel was run in two ways: (1) test section vented to atmosphere and (2) settling chamber vented. In the latter case, the static pressure at the test section runs below atmospheric pressure. The upper portion of Figure 6.23 shows dynamic pressure,  $q$ , versus Mach number for each of these operating conditions. The lower portion of Figure 6.23 shows the pressures measured within the spheres. Note that the internal pressure was always below the static pressure of the flow. Expressing this pressure difference as a fraction of  $q$  (pressure in lower graph divided by  $q$  of upper graph), as in Figure 6.22, one finds that the internal pressure was between  $P_s - 0.1q$  and  $P_s - 0.3q$  for the range of test conditions at DTMB.

Assuming the force-gage-pressure distribution for wind-tunnel conditions (Figure 6.22) is applicable to blast-wave flows and taking



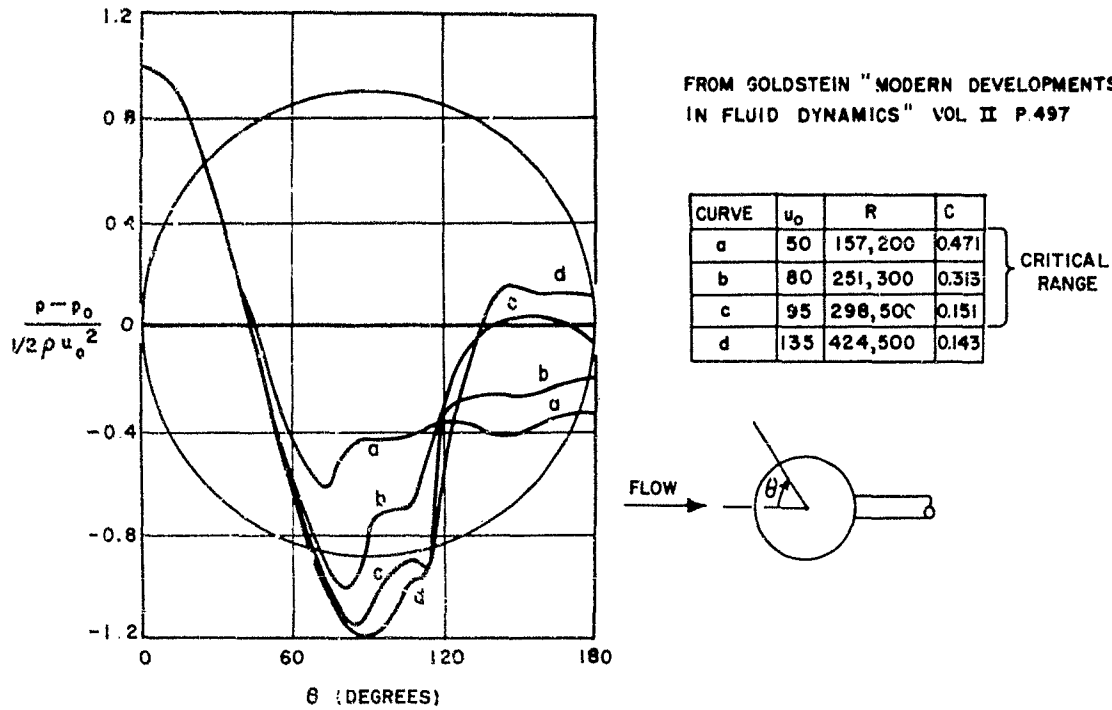


Figure 6.22 Pressure Distribution on Spheres.

$P_1 = P_0 + P_s \pm bq$ , where  $0 < b < 1$  (conservatively using the extremes reached by  $(P - P_0)/q$  in Figure 6.22), one may rewrite Equation 6.4 for rapidly leaking gage:

$$F = qC_D A \pm bqa \quad (6.7)$$

Also, for initial

$$\begin{aligned} P_1 &= P_0, \\ F_0 &= 0, \text{ and} \\ C_D &= \frac{4F}{qA} \pm b \frac{a}{A} \end{aligned} \quad (6.8)$$

For  $a/A = 0.085$  (3-inch gages) to  $0.090$  (10-inch gages),

Equation 6.8 shows that the correction to  $C_D$  for rapidly leaking gage is less than  $\pm 0.1$ , within the framework of the assumption that  $(P_0 + P_s - q) < P_1 < (P_0 + P_s + q)$ .

Having considered the behavior of the perfectly sealed gage and that of a rapidly leaking gage, it is now possible to formulate criteria for the interpretation of the wind-tunnel and shock-tube test records of gross force versus time.

1. Wind-Tunnel Measurements. Wind-tunnel flow is of sufficient duration so that the internal pressure does not change with time, as may

be seen from the tape recordings of the force. Unfortunately, however, few measurements were made of the internal pressure. In these few cases where internal pressure was measured, the uncorrected force readings indicated drag coefficients about 0.01 too high at  $M = 0.2$  and about 0.03 too high at  $M = 0.6$ . Whether the remaining measured drag coefficients are correct within 0.01 to 0.03 is problematical, in view of the uncertainty of location of the leak and lack of knowledge of pressure distributions at these Reynolds and Mach numbers. For this reason, the results of these wind-tunnel tests, without internal pressure readings, have been presented without corrections. Because of these uncertainties, an estimated maximum error of  $\pm 0.1$  in  $C_D$  is introduced into the wind-tunnel results.

2. Shock-Tube Tests. Since the majority of the shock-tube tests were run with 3-inch Gages 10, 11, and 18 and these three gages were checked for leakage characteristics in the pressure step-function apparatus, it was possible to correct for pressure effects. Gages 11 and 18 leaked slowly enough for Equation 6.6 to hold throughout the shock-wave duration (20 to 40 msec). Records from these gages were used for analysis of  $C_D$  throughout the flat top and decay of the wave in the shock tube to permit investigation of the question of one-to-one correspondence of  $C_D$  and  $P_s$ , independent of any previous loading history.

Gage 10 leaked more rapidly than the other two, but not fast enough for Equation 6.8 to be valid. The initial value of  $C_D$  (immediately after the diffraction phase) was read from Gage 10 records on the assumption that not much leakage had occurred during the 3 or 4 msec in which violent oscillations were dying down. (One could reason that, since the effective sting area had dropped to about 50 percent (Figure 6.21) in 20 msec, it would drop about 13 percent in 5 msec.) However, the

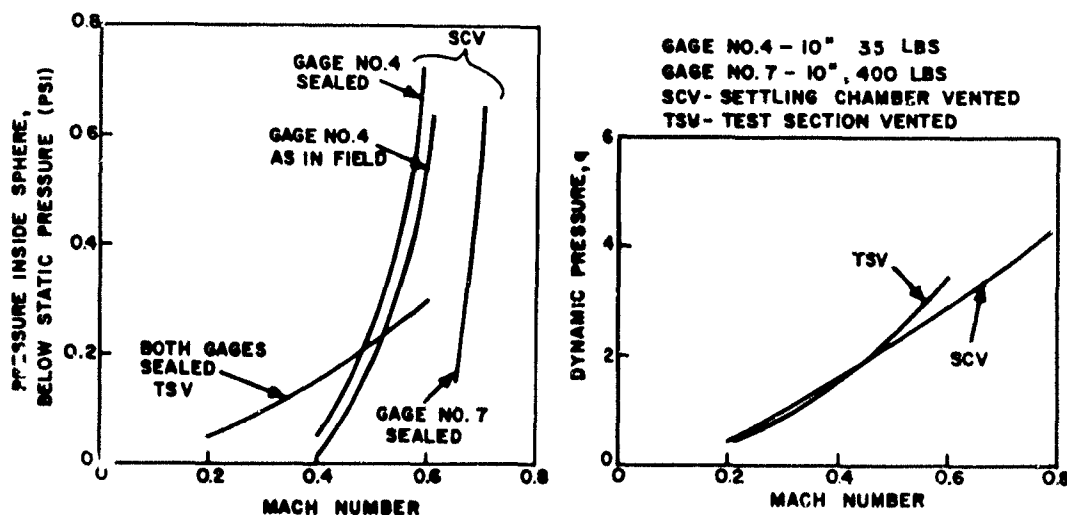


Figure 6.23 Pressure Inside Force Gages During DTMB Wind Tunnel Tests.

accuracy of these initial values of  $C_D$  obtained from Gage 10 is uncertain, perhaps within 20 percent.

It may be noted here that a force gage that leaked rapidly at the sting would be more useful than is indicated above by the estimate of accuracy of  $C_D$  within  $\pm 0.1$ , since such a gage would be expected to record drag forces of about the same magnitude that would exist for the stingless sphere. Assuming that the base pressure is not appreciably affected by the presence of a sting (note the fact that the pressures are fairly constant from about  $\theta = 150^\circ$  to  $\theta = 180^\circ$  in Figure 6.22), one may write Equation 6.4 with  $P_i$  equal to absolute base pressure,  $P_b + (P_s + P_o)$ ,

$$(P_o + P_s - P_b - P_s - P_o)a + qC_D A = F$$

or, since  $F_o = 0$  for a leaky gage:

$$\Delta F = qC_D A - P_b a$$

If one wanted to find the force on a stingless sphere, using the drag measured by a sting-supported gage which read drag forces correctly, the conversion factor would be base pressure ( $P_b$ , not absolute base pressure) times sting area. That is, the force on the stingless sphere would be:

$$\Delta F = qC_D A - P_b a$$

This expression is identical with Equation 6.9, which illustrates the point that the rapidly leaking gage with a sting could be used to measure the drag coefficient of a stingless sphere.

Some shock-tube tests were performed using a 3-inch gage with Pliobond removed from the base seal between shell and sting. Figure 7.7 illustrates the nature of the force-time records obtained from such a gage, as compared with force-time records from the same gage in a sealed condition. Note the persistence of violent oscillations on the record of the open gage, which makes these records difficult to smooth and interpret and, therefore, relatively inaccurate. An effort was made to seal the gages used in the shock-tube tests, correct for the effect of static pressure, and make all drag coefficient comparisons for spheres with stings.

The discussion of gage reproducibility must be reopened in light of the fact that a correction factor must be subtracted from the force reading, as per Equation 6.6. If  $e_1$  is the error in force-gage reading,  $e_2$  is the error in the correction factor and  $e$  is the probable cumulative error in the final determination of drag coefficient:

$$e^2 = e_1^2 + e_2^2 \quad (6.10)$$

The cumulative error,  $e$ , is now somewhat larger than the error due to irreproducibility of the gage. Further, and more important, it becomes

evident that the process of subtraction makes it necessary to take a sufficient number of readings at any one point to insure statistical significance. Consider, for example, the 3-inch force gage that reads 2.2 pounds force where  $P_g = 3$  psi ( $q = 0.22$  psi). The uncorrected drag coefficient  $\Delta F/qA = 1.45$  must be adjusted as per Equation 6.6 or Figure 6.15:

$$C_D = 1.45 - 1.20 = 0.25$$

If it is assumed, however, that the gage reading was  $2.2 \pm 0.33$  (15 percent error) and that there was no error in the pressure correction:

$$C_D = (1.45 \pm 0.22) - 1.20 = 0.25 \pm 0.22$$

This individual reading could be between 0.03 and 0.47. Thus it is evident that many tests at a point are necessary when one uses the presently developed force gage that requires correction to its readings because it is pressure-sensitive.

CONFIDENTIAL

## Chapter 7

# PROCEDURES AND RESULTS

The operational plan for the aerodynamic evaluation of the 3-inch and 10-inch spherical models in the test facilities available has been presented in Chapter 5, as well as the broad objectives of the Teapot laboratory tests. The objectives were not more specific, because it was not expected (due to limitations on the extent of the program) that definitive answers would be obtained as to the influence of each likely drag-loading parameter. The following parameters were investigated, some rather thoroughly and others briefly, for their effects on the drag coefficient of the sphere:

1. Shock-tube flow parameters: (1) shock overpressure, defines Mach number and Reynolds number per unit size; (2) Reynolds number, due to size of model; and (3) wave shape, flat top versus peaked shocks.

2. Wind tunnel flow parameters: (1) Mach number and (2) Reynolds number, due to size of model and also venting condition of the wind tunnel.

3. Condition of model: (1) surface roughness, (2) frequency of model, (3) damping of model, (4) sealed model versus model with opening at sting, and (5) model at angle of attack to flow.

The effects of turbulence of the flow were not investigated systematically, since the state of the art of turbulence measurements indicated that such an investigation would require extensive effort. Some qualitative information is afforded indirectly, however, since the two wind tunnels used for obtaining drag data could be expected to have somewhat different levels of turbulence (although neither wind tunnel had been calibrated for turbulence).

The measurements made in the wind tunnel included the free stream parameters  $M$ , Mach number, Reynolds number, and  $q$ , as well as the force on the model. Data reduction consisted of dividing force by  $q$  and  $A$ , as per Equation 6.1 or Equation 6.8, with an estimated accuracy of  $\pm 0.1$ , to yield values of  $C_D$ . Besides plots of  $C_D$  versus Mach and Reynolds numbers, information was obtained on the frequencies of vibration of the models, which were not necessarily the same as their natural frequencies.

Shock-tube instrumentation was much more difficult than wind-tunnel instrumentation, due to the transient nature of the flow. Side-on overpressure versus time was measured simultaneously with force versus time. These overpressure records were converted to  $q$ -

time records by theoretical calculation based on the Rankine-Hugoniot formula and on the assumption of adiabatic flow within the wave. Point-by-point comparisons of force-time and  $q$ -time records were made to yield curves of  $C_D$  versus time for each shot, as per Equation 6.6 for the sealed gages. "Pseudo-steady" values of  $C_D$  could then be plotted versus Mach and Reynolds numbers and compared with similar plots for wind-tunnel and free-flight data.

Much emphasis was placed on obtaining valid and consistent data in the wind tunnel and shock tubes by such methods as cross-correlating the supporting measurements of  $P_g$  and  $q$  and repeating the same test as many times as might prove necessary to achieve statistical confidence. Thus, the laboratory investigation contrasted sharply with the Teapot field test, where the condition of the gages was not well known at the time of the test, reliable supporting parameters were not available, and insufficient numbers of measurements of force were made at each gage station.

## 7.1 BRL 24-INCH DIAMETER SHOCK TUBE

7.1.1 Procedure. The 24-inch-diameter shock tube at the Ballistic Research Laboratories, Aberdeen, Maryland, was made available to NOL from 1 October to 5 October 1955 and from 17 October to 21 October 1955 for testing the 3-inch diameter spherical force gages used during Operation Teapot. Because of the problem of blockage of flow, the 10-inch-diameter gages were not tested in this shock tube. It was estimated that flow blockage difficulties would not be significant for the 3-inch gages and that the effects of wall proximity in producing shock reflections would be negligible insofar as these signals would hardly register on the relatively low-frequency force gages.

Figure 7.1 shows the 3-inch force gage mounted at  $0^\circ$  (sting parallel to the flow). Changes in inductance of the pad-coil circuit due to elastic deflection of the gage (caused by the applied loading) were responsible for changes in the frequency of the oscillators. The oscillator signal was fed through a discriminator (see Figure 2.1 for the similar field setup) and thence to an oscilloscope for photographic recording of the signal. A frequency-alarm step and a timing signal were recorded with the force record on the same film, thus providing a means of interpreting the record in terms of frequency shift (or force, from the gage calibration curve, Figure 6.12, for example) as a function of time.

BRL personnel recorded the side-on pressure-time signature of the input shock waves and the shock front velocity, or more precisely, the time for the shock front to traverse the distance between two fixed points. The gage station was located such that the shock was well-formed by the time it reached the station (except at very-low pressures of the order of 2 psi) and such that reflections from the open end of the tube did not return soon enough to disturb the record. Figure 7.2 shows the typical pressure records,

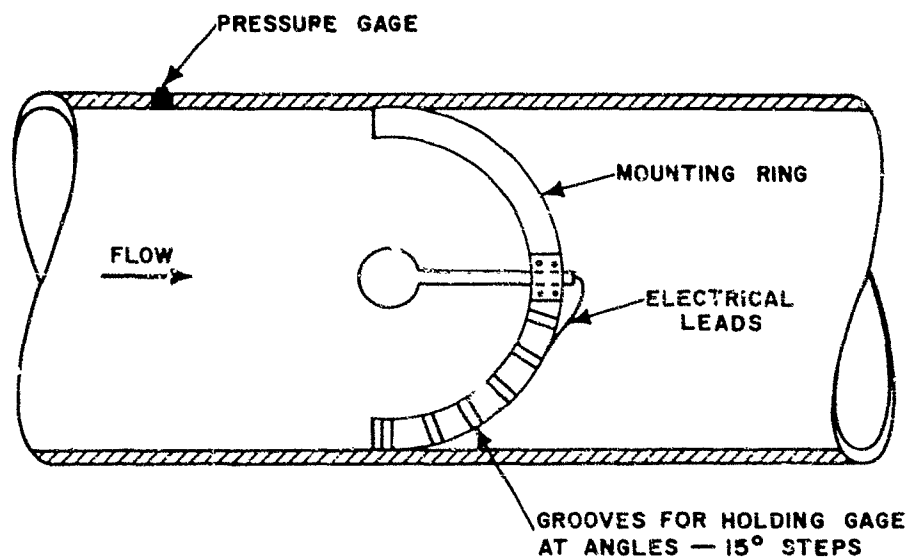


Figure 7.1 Plan View of 3-inch Gage and Mount in BRL Shock Tube.

one with a peak of about 8 psi, and the other about 3 psi. The velocity-measuring equipment did not function properly at very-low pressures, and no readings were taken below about 2 psi. Essentially, then, the applied aerodynamic forcing function consisted of a flat-topped shock wave of 10 to 15 msec duration, followed by a decay lasting about 40 msec.

The parameters under investigation included surface condition of the gages, effects of sealing and leakage of pressure, effects of damping and natural frequency of gage, and peak static over-pressure,  $P_s$ , (which defines the other shock-wave properties, assuming an ideal wave). Surface conditions were varied from

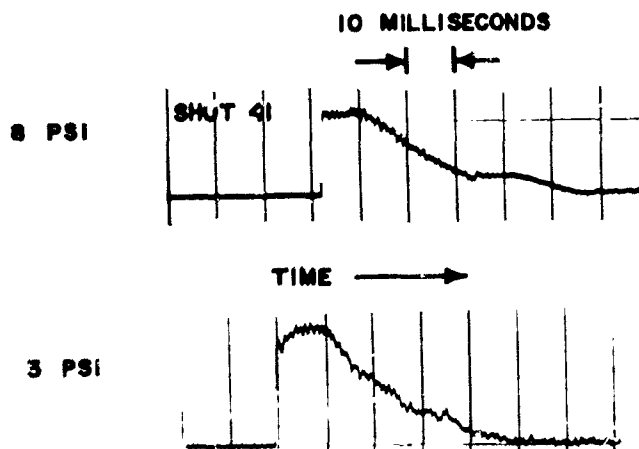


Figure 7.2 Typical Pressure Records in BRL 24-inch Shock Tube.

extreme roughness (surface fouled with damping fluid and coarse particles) to a slightly irregular surface, to a polished surface, and finally to a reproducible surface consisting of a very-thin rubber cover. Damping varied from underdamped to overdamped, and natural frequency varied from about 140 to about 380 cps. Sealing was varied by stripping various amounts of the Pliobond loose from the base seal. Side-on flat-top overpressures ranged from 2 to 20 psi.

Some of the qualitative effects of these parameters may be seen in the force-time records. Figure 7.3 presents typical force-time records obtained in the BRL shock tube with well-damped spherical force gages. The three parallel dotted lines are frequency-calibration steps, with 2.5 msec between dots (400 cps timing). Note the general similarity to the side-on-pressure records of Figure 7.2, except for the diffraction spike. The existence of the diffraction spike and the dependence of spike amplitude on the natural frequency of the force gage, as illustrated in Figure B.4, are discussed in Appendix B. Note also that both sets of records in Figure 7.3 display oscillations of about 550 cps, even though Gage 11 has a natural frequency of 330 cps and Gage 10 has a natural frequency of some 140 cps.

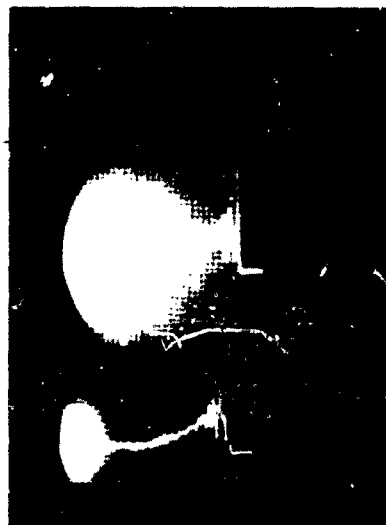
Figures 7.4, 7.5, and 7.6 show the qualitative effects of damping on the force-time signatures of Gages 18, 10, and 11, respectively. Figures 7.4 and 7.5 show that the force records from underdamped gages exhibit lower-frequency oscillations than the records from the well-damped gages. Figure 7.6 shows that Gage 11 can vibrate at the low frequency, whether well damped or underdamped. These effects will be discussed quantitatively in the following sections, as will the effect of gage leakage illustrated in Figure 7.7.

The reduction of data may be briefly summarized as follows:

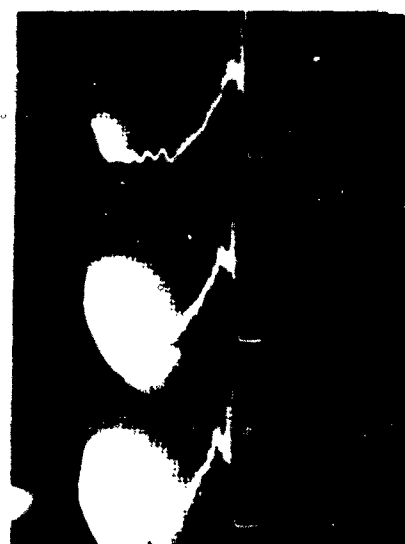
1. Peak side-on pressure is calculated from the Rankine-Hugoniot relations for the ideal shock wave by the use of the shock-front velocity measured by the light screen and the taking of ambient temperature into account. It was possible to account for and correct those situations which involved triggering of the light-screen pickups by an initial overshoot or an early spike on the slow buildup of the lower blast pressures (these irregularities are clearly visible on the backup-pressure-gage records, such as Figure 7.2). It was also possible to check these corrections, since the same backup pressure gage was used for all shots, and its calibration (checked against the light-screen peaks) did not change appreciably during the course of the tests. Once having identified the flat top (or other distinctive signal which triggered the light-screen pickups), it was possible to scale all pressures directly from the pressure-time records, such as that given in Figure 7.2.

2. Dynamic pressure,  $q$ , is calculated from the Rankine-Hugoniot relations for the entire wave history corresponding to





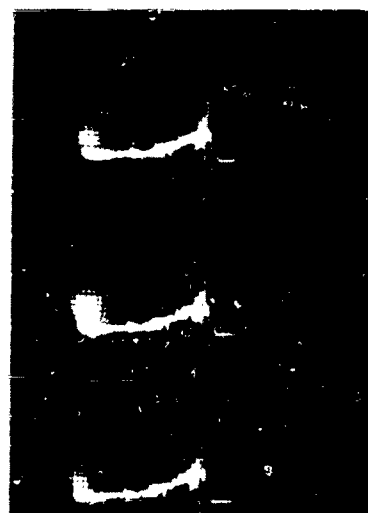
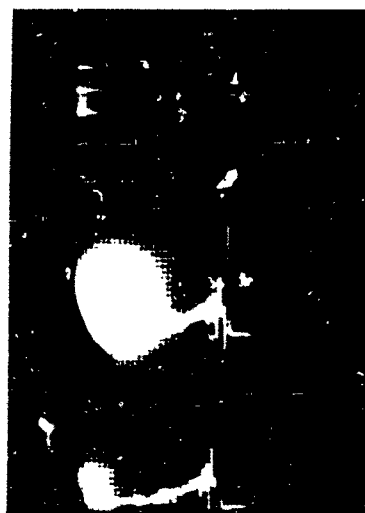
SHOT 18-22 (10 PSI)  
HIGH FREQUENCY GAGE (NO. 11)



SHOT 36-42 (8 PSI)  
LOW FREQUENCY GAGE (NO. 10)

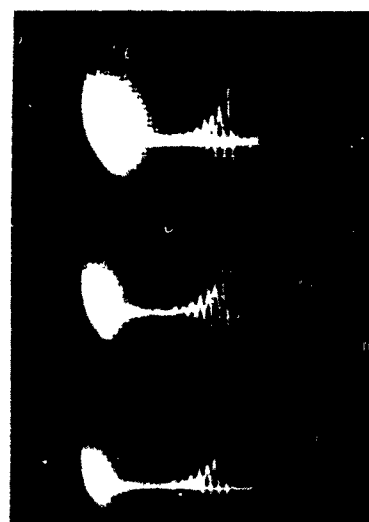
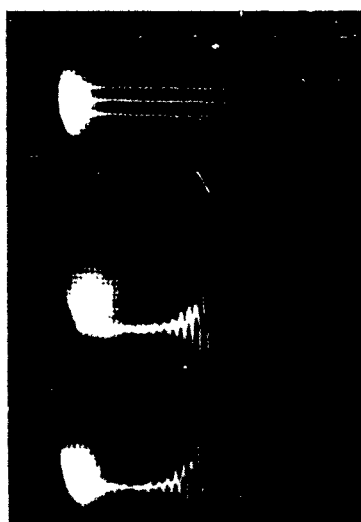
Figure 7.3 Force Records for Gages with High and Low  
Natural Frequencies in the BRL Shock Tube.

WELL  
DAMPED



SHOTS 53-57 (10 PSI)

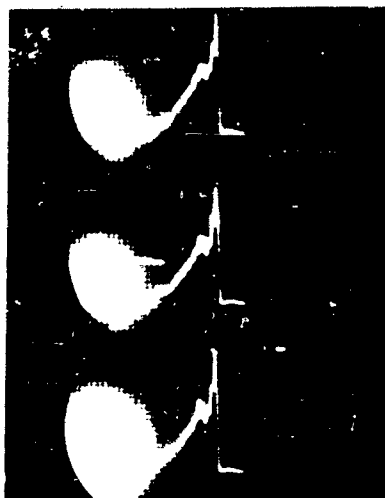
UNDERDAMPED



SHOTS 58-62 (8 PSI)

Figure 7.4 Effect of Damping on Force Records of  
Gage 18.

WELL  
DAMPED

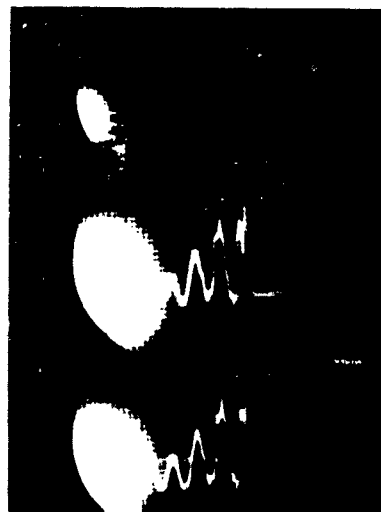


SHOTS 45-47 (6 PSI)



SHOTS 85-87 (6 PSI)

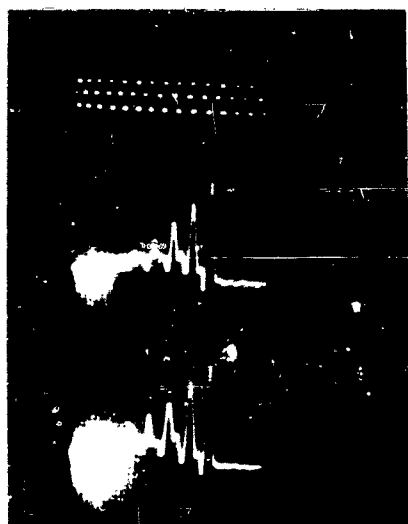
UNDERDAMPED



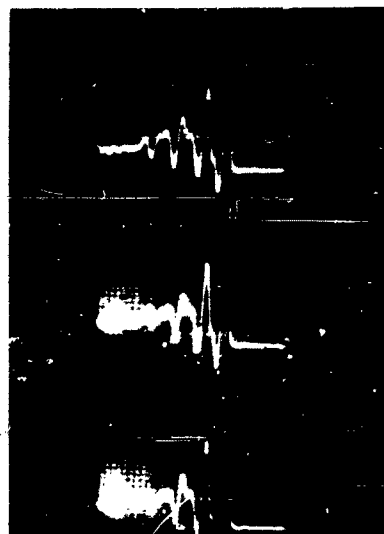
SHOTS 117, 118 (6 PSI)

Figure 7.5 Effect of Damping on Force Records of  
Gage 10.

WELL  
DAMPED

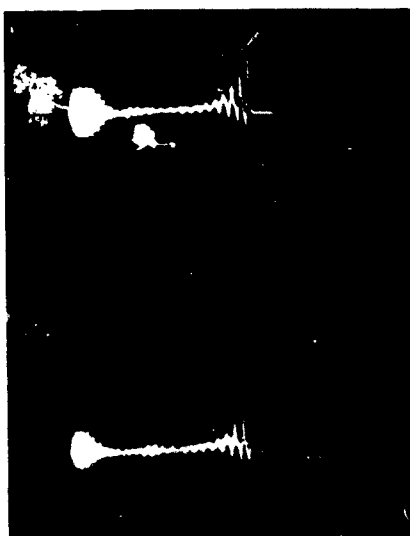


SHOTS 151, 152 (15 PSI)



SHOTS 163-165 (10 PSI)

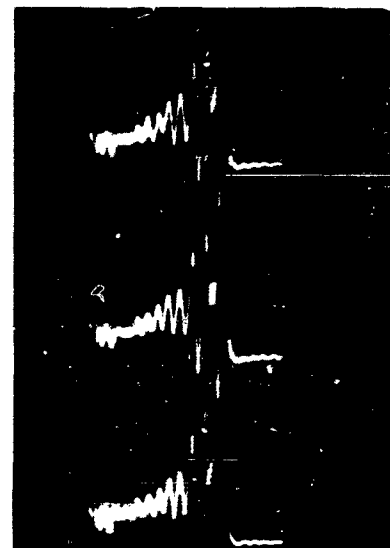
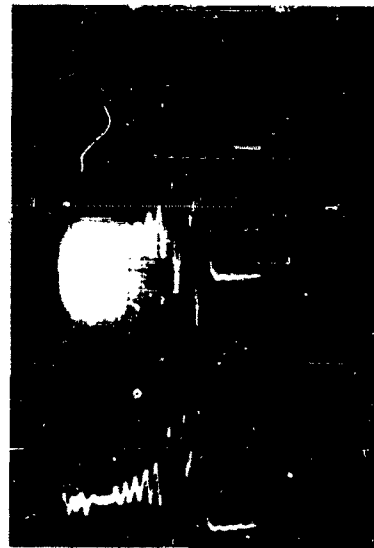
UNDERDAMPED



SHOTS 70, 72 (8 PSI)

CONFIDENTIAL

Figure 7.6 Effect of Damping on Force Records of Gage 11.



SHOTS 166-170 (10 PSI) GAGE COMPLETELY SEALED

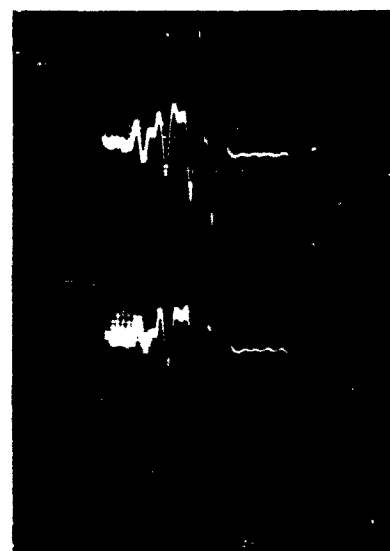


Figure 7.7 Force Records for Sealed and Leaking Gages in BRL Shock Tube.

the pressure records. (For low-pressure shocks, such as those used, it may be shown that there is little difference between the  $q$  calculated by the Rankine-Hugoniot formula and the  $q$  calculated on the assumption of adiabatic flow within the wave.)

3. A line is faired through the midpoints of the oscillations of the force-time records (more precisely, the record of frequency shift or voltage versus time). At any instant in time the signal amplitude is measured from the base line to the faired record and compared with the calibration step on the same film. This amplitude is converted to a frequency shift, which in turn is converted to force,  $F$ , through use of the static calibration curve of force versus frequency (such as Figure 6.12).

4. Drag coefficient,  $C_D$ , is computed at any instant in time by the assumption that the pressure correction for the sealed gage is applicable, whence  $C_D = (F - aP_s)/qA$ , where  $P_s$  and  $q$  occur at the same time as  $F$ . The leaky Gage 10 is treated in the same manner, the effects of leakage thus showing up on the  $C_D$  time curves.

5. Oscillation frequencies are estimated by the comparison of the peak-to-peak distances of the oscillations with the distance between the timing signals. The more-sophisticated methods of frequency analysis were not warranted at this stage of the program.

7.1.2 Results. Using the above procedures, the force records obtained in the BRL shock tube were reduced to curves of  $C_D$  versus time or  $C_D$  versus side-on-overpressure (throughout the decay of the shock wave) for any one shot,  $C_D$  versus  $P_s$  (peak overpressure) for all shots, etc. It was hoped that the curves of  $C_D$  versus overpressure for each shot as the wave decays would coincide with  $C_D$  versus peak overpressure for all shots, since this would signify a direct correspondence of  $C_D$  with overpressure, regardless of the shape of the shock wave.

Mention has been made of the fact that high-frequency oscillations sometimes appeared on records obtained with low-frequency gages. For example, Gage 10 sometimes exhibited 140-cps oscillations (its natural frequency) and sometimes it appeared to oscillate at about 550 cps, either one or the other mode of response occurring when loaded by apparently identical shock waves. The next item of significance noted was that the 550-cps oscillation was common to all three 3-inch-diameter spherical gages tested, regardless of their respective natural frequencies. That is, all three gages sometimes appeared to vibrate at 550 cps and sometimes at their own natural frequencies (140 cps, 330 cps, and 380 cps). The third fact was that the drag coefficient obtained by fairing a line through the oscillations was different for the records showing vibrations at 550 cps from those obtained from the records showing

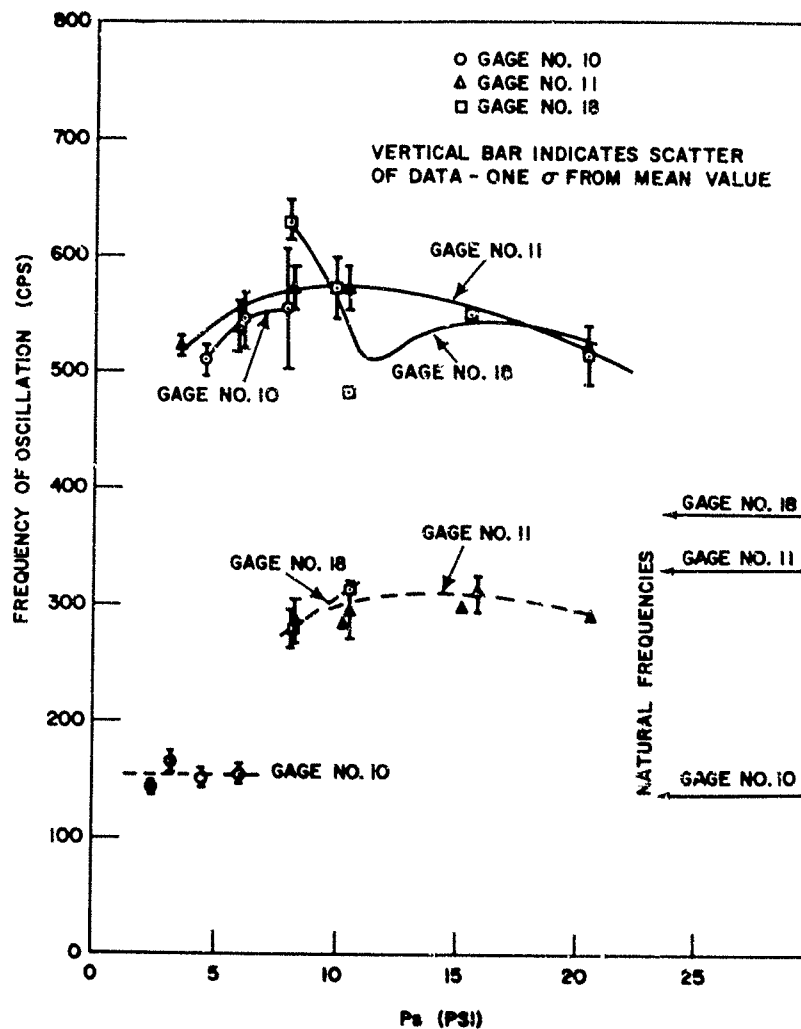


Figure 7.8 Frequencies of Oscillation on Force Records - MFL Shock Tube.

the lower (natural) frequency oscillations. This latter fact is particularly disturbing; however, no aerodynamic significance is attached to it at this time for the following reasons:

1. Figure 7.8 presents the data on frequency of oscillation appearing on the shock-tube force records. Note the double-valued curves for each gage (the solid-line curves at about 550 cps and the dashed curves roughly at gage natural frequency) with little dependence on  $P_s$  and, hence, little dependence on Mach number. If this phenomenon were similar to the vortices breaking away from cylinders, the frequency would be proportional to some constant Strouhal number and to the flow velocity.

2. In most cases where the 550-cps oscillation appeared on the force signature, the same frequency signal appeared on

the trace before the shock arrived at the gage. It is probable that the source of this extraneous signal stems from shock-tube-wall vibrations, sting and mount vibrations, and the complex interplay of these vibrations.

Figures 7.9, 7.10, and 7.11 show that: the apparent drag coefficients depend on the oscillation frequency; the drag coefficient

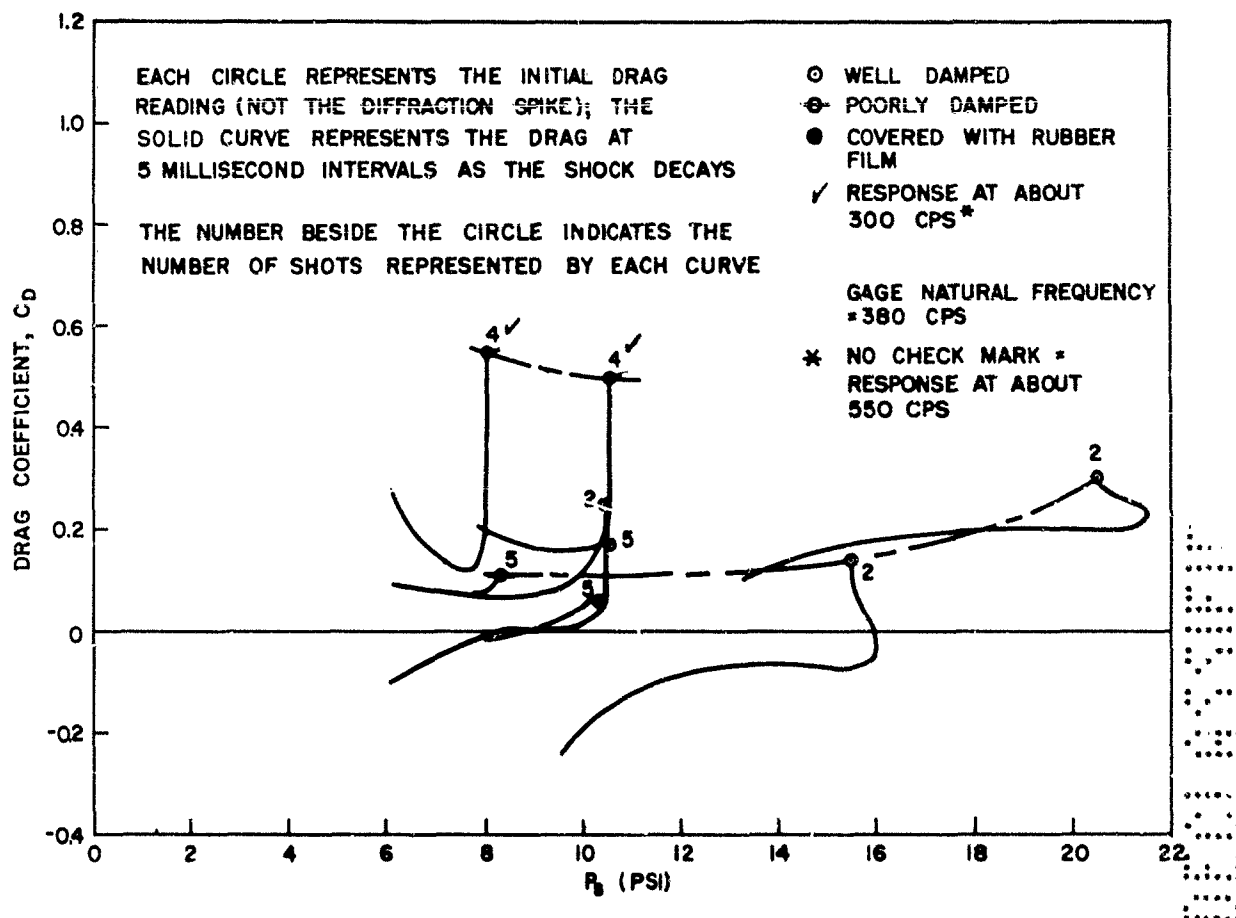


Figure 7.9 Drag Coefficients for Gage 18 (3-inch, 15-pounds) in BRL Shock Tube.

appears to shift during the course of each loading history; the drag coefficients obtained from each record exhibiting 550 cps seems to follow the same rough  $C_D - P_0$  plot as the initial values from many shots; and the degree of damping influences the mode of oscillation. Having presented the conclusions, a closer examination of Figures 7.9, 7.10, and 7.11 is in order.

The dashed curves are faired through the circles, which represent the mean values of the initial  $C_D$  readings for several shots, the



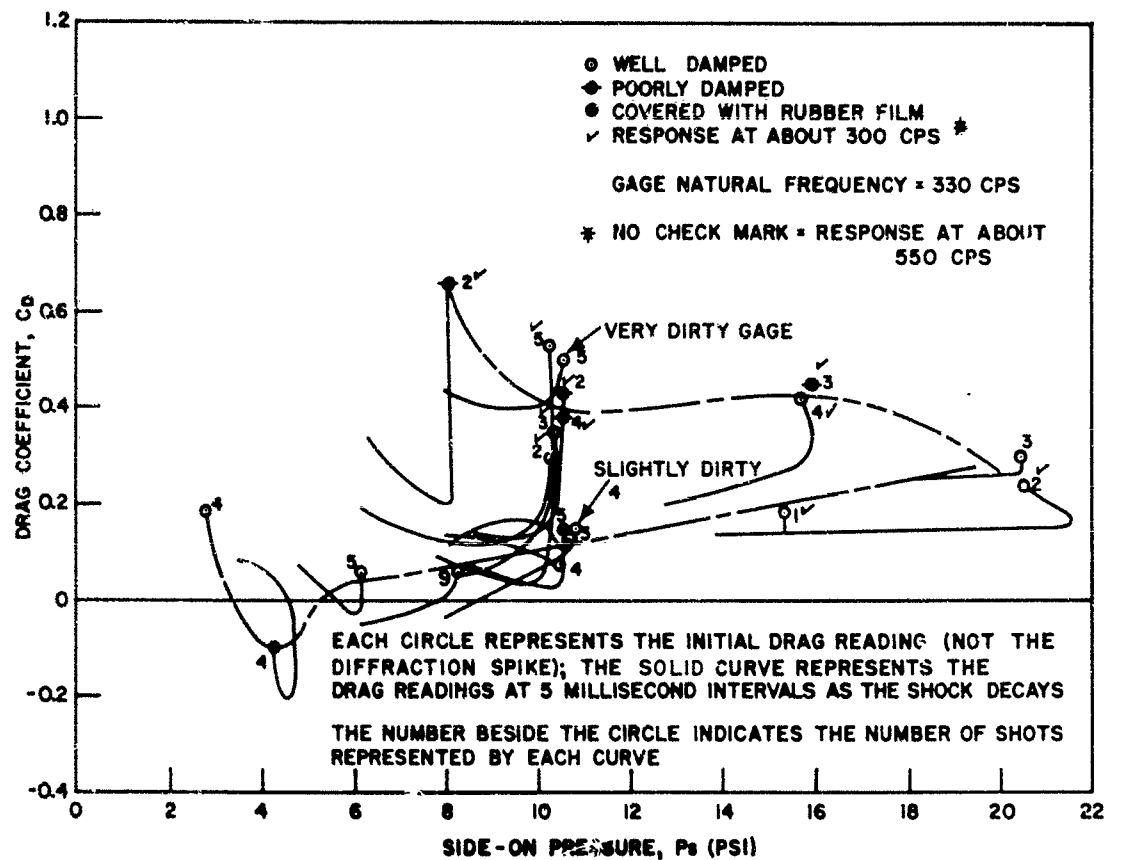


Figure 7.10 Drag Coefficients for Gage 11 (3-inch, 25-pounds) in BRL Shock Tube.

number adjacent to each circle indicating the number of shots represented. Two distinct dashed curves are obtained, one where the initial vibrations were at gage natural frequency (check marks) and one where the initial vibrations were at 550 cps. The solid curves appended to each circle represent the  $C_D$  values taken at 5-msec intervals (generally up to 20 msec) as the shock wave decays.

Figure 7.9, for Gage 18, shows two distinct dashed curves, different by a factor of about 5. The upper dashed curve, characterized by initial vibrations at about gage natural frequency, appears to occur when the gages are poorly damped. In each case, the solid decay curves rapidly drop down to the lower dashed curve as though the gage were leaking, but then level off parallel to the dashed curve.

Figure 7.10 for Gage 11 represents a much-more-exhaustive set of data. Again, there are two dashed curves, although for this gage a point on the upper curve sometimes occurs with a well-damped gage (points on the lower curve never occur with a poorly damped gage). In each case the decay curves drop from the upper dashed curve to the lower dashed curve, whereas the decay curves starting on the lower dashed

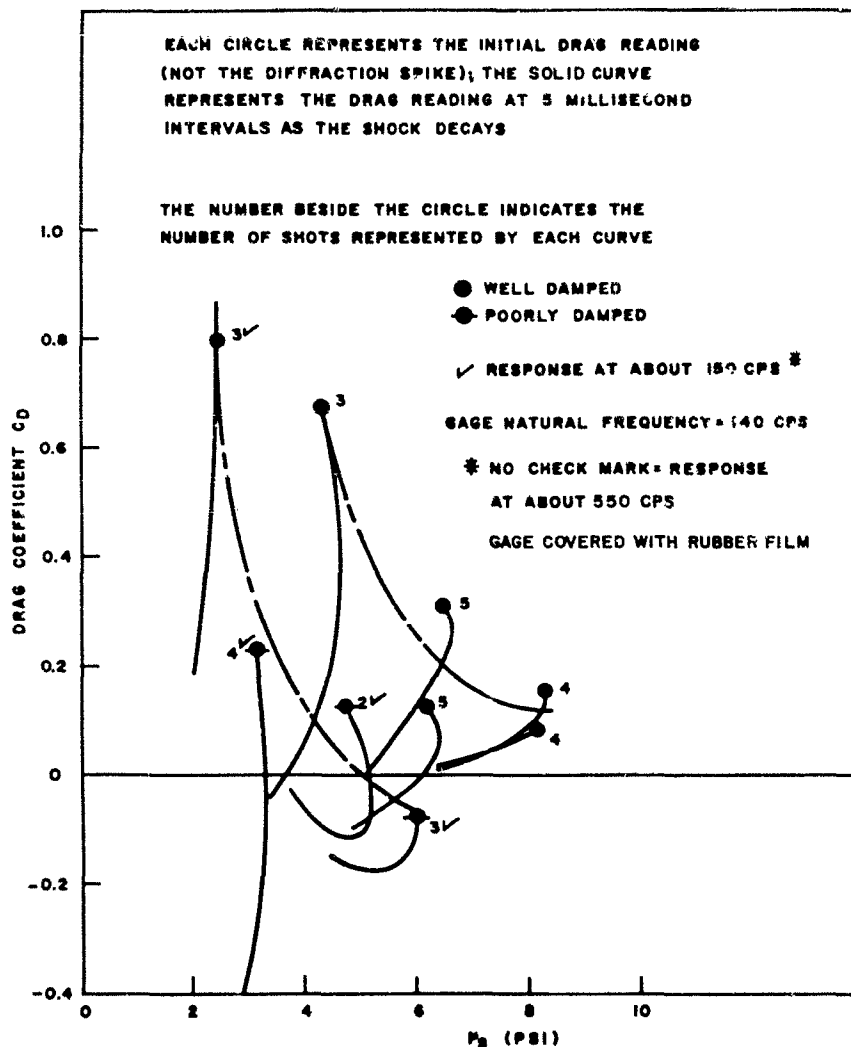


Figure 7.11 Drag Coefficients for Gage 10 (3-inch, 3-pounds) in BRL Shock Tube.

curves continue to coincide with the lower dashed curve. An exception is the record of the very dirty gage (smeared with grease and sprinkled with large particles of silica gel), which falls in the high  $C_D$  region (even though the gage was vibrating at high frequency) and decays in the high  $C_D$  region. The slightly dirty gage acts like the clean gages. Its being covered with the reproducible rubber surface film seems to have little effect. Drag coefficients do not seem, therefore, to be particularly sensitive to small amounts of surface roughness.

Figure 7.11, for Gage 10, reverses the position of the dashed curves, although there are still two distinct curves, and the low-frequency curves are induced by underdamping, as was true of the other two gages. The decay curves for each shot drop rapidly with time, probably due to the fact that Gage 10 was known to leak rapidly (see Figures 6.18 and 6.21).

Even the initial  $C_D$  values are probably about 15 percent low, due to leakage during the diffraction oscillations.

Figure 7.12 illustrates the decay behavior of a gage with various leakage conditions. (Drag coefficient is calculated as for a sealed gage.) Note that the initial point is unaffected by small leaks (0.008 in<sup>2</sup> opening was attained by stripping of 1/4-inch of the Pliobond base seal, a hole not likely to exist in a "sealed" gage) but that the decay changes radically when a leak exists. It was on this basis that the initial values of the leaky Gage 10 were retained and reported.

Figure 7.13 summarizes the data for the three 3-inch gages tested in the BRL 24-inch shock tube. The amount of scatter of the data is quite large, pointing up the need for many shots at each point. The scatter is greatest at lower pressures, the critical Reynolds number regions (see Figure 6.1). The lateral shift of the critical Reynolds-number region for each individual gage is believed responsible for the major disparities in the three solid curves.

## 7.2 ARF 6-FOOT-DIAMETER SHOCK TUBE

7.2.1 Procedure. The 3-inch and 10-inch spherical force gages were tested in the Armour Research Foundation (ARF) shock tube in Gary, Indiana, from 9 November through 19 November 1955. This 6-foot-diameter shock tube was considered suitable for the 10-inch-diameter spheres and also afforded the opportunity to study the loading effects of a peaked shock wave.

The parameters to be investigated included peak shock overpressure, size of gage, and wave shape; this latter parameter and the size parameter were tied together by expressing the decay rate of the wave relative to the transit time of the shock front, the transit time depending directly on size.

In the ARF shock tube, the shock waves were generated by detonating various lengths of primacord upstream of the model, some control over duration of the blast being afforded by variation of the distance of the charge from the model. Shock waves produced in this fashion have a sharp rise and a fairly linear decay. Since a blast wave with long duration was desired, the charge was placed as far away as possible (about 100 feet), which resulted in a positive blast duration of about 25 msec.

Figure 7.14 consists of typical  $P_z$  records obtained from ARF barium titanate gages mounted flush in the wall of the shock tube. The initial peak value of each record was checked with the value obtained from shock-velocity measurements, also made by ARF personnel. NOL personnel recorded the force-gage information and also made some supporting  $P_z$  and  $q$  measurements with an SRI gage, which contains Wilcnko pressure-sensing elements compatible with the NOL recording instrumentation. The NOL instrumentation was similar to that used at BRL (see Figure 7.15).

GAGE NO. 18 (3", 15 LBS) IN BRL SHOCK TUBE

AREA EXPOSED TO EXTERNAL PRESSURE INCREASED BY PROGRESSIVE REMOVAL OF PORTIONS OF PLIOBOND BASE SEAL

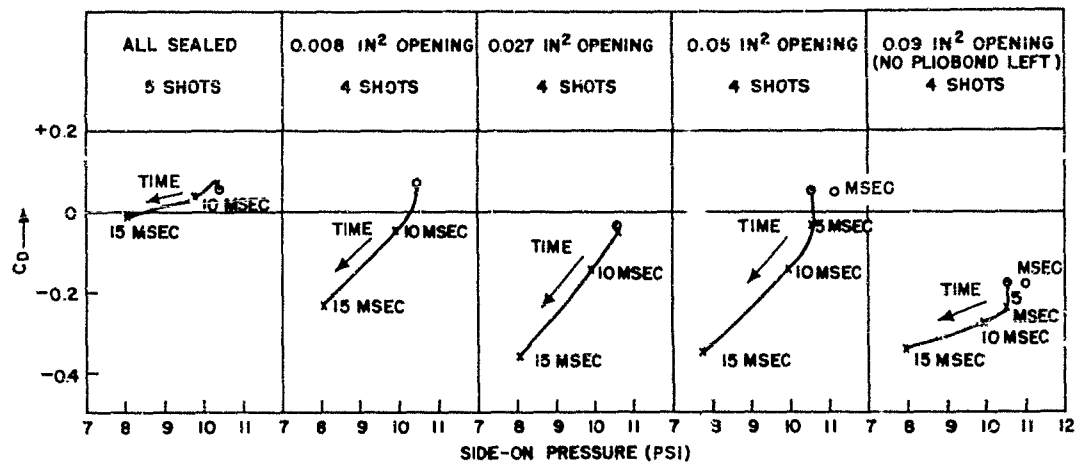


Figure 7.12 Effect of Leakage Area on  $C_D$ -Time or  $C_D$ - $P_s$  Curves.

SOLID CURVES - OSCILLATIONS ON RECORDS ARE AT ABOUT 550 CPS  
DASHED CURVES - OSCILLATIONS AT ABOUT NATURAL FREQUENCY OF GAGE  
VERTICAL BARS INDICATE SCATTER OF DATA - ONE  $\sigma$  FROM MEAN VALUE

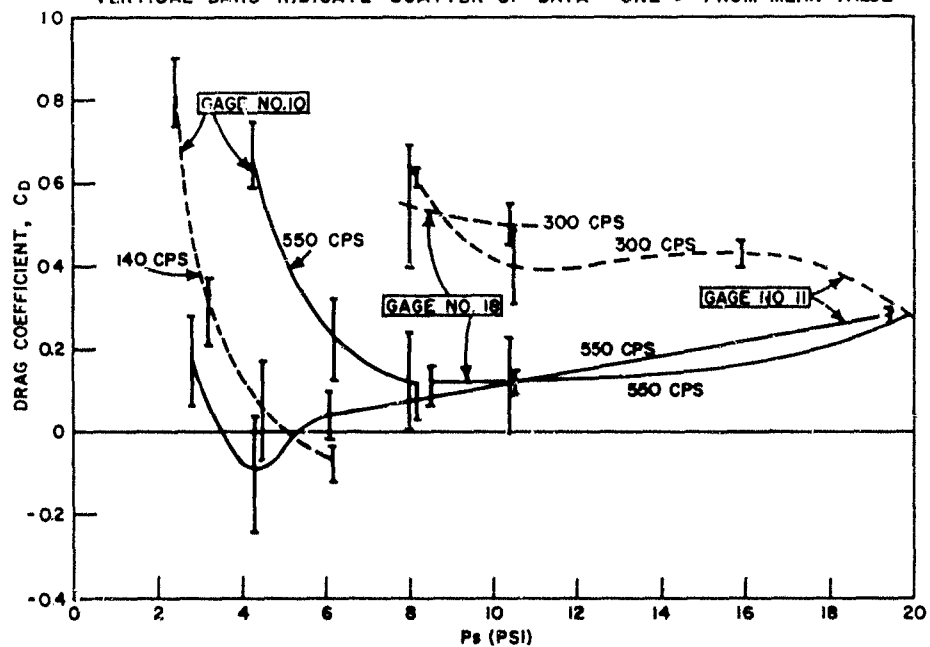


Figure 7.13 Summary of Initial Drag Coefficient in BRL Shock Tube (Dashed Curves of Figures 7.9 through 7.11).

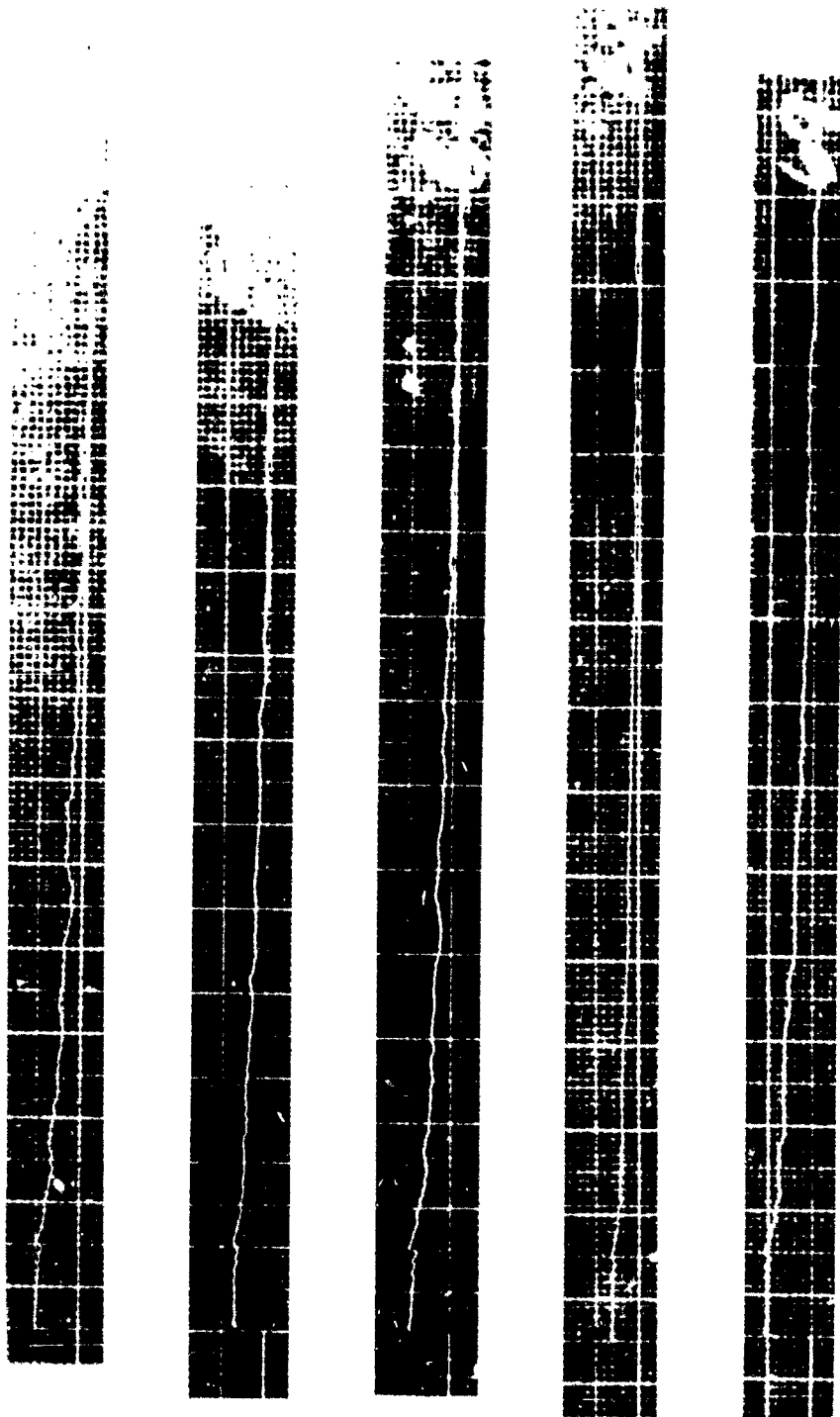


Figure 7.14 Pressure-Time Signatures in the ARF Stock Tube.

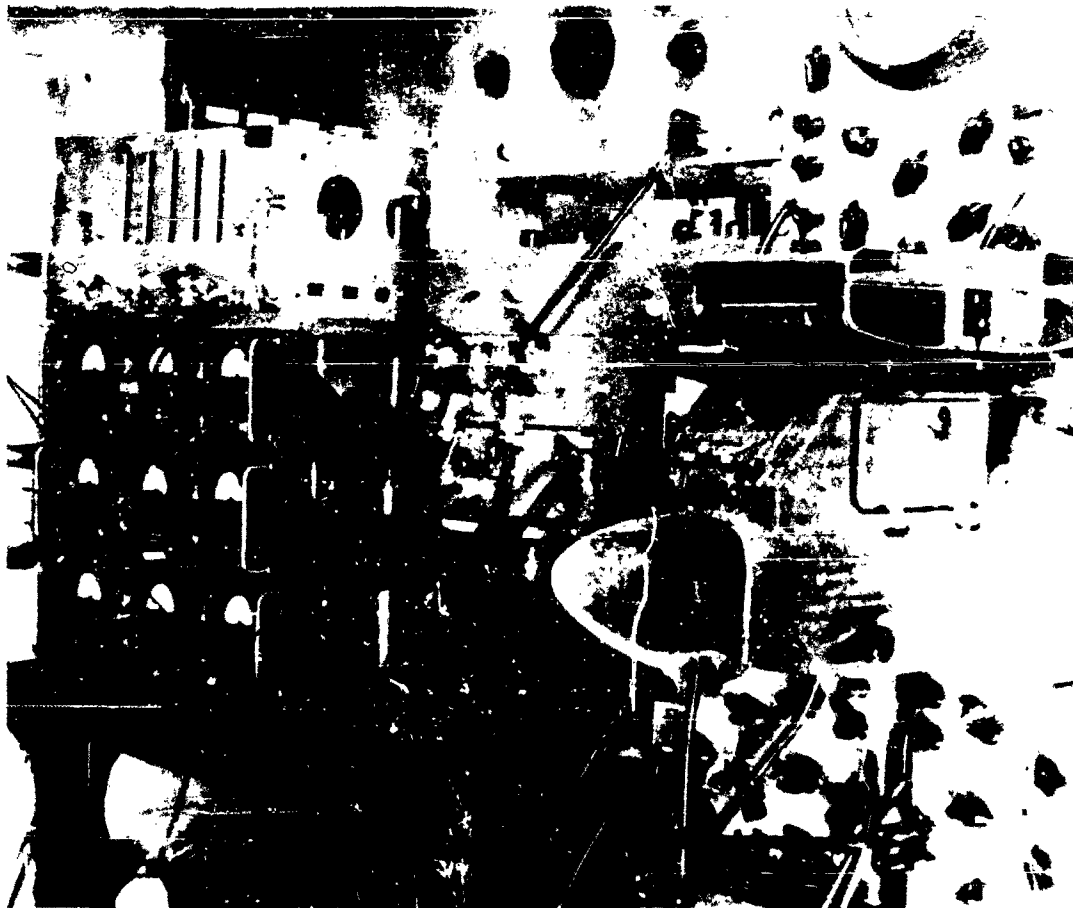


Figure 7.15 NOL Recording Instrumentation - ARF Shock Tube Tests.

At first, the force gages were mounted on the floor of the shock tube, as shown in Figure 7.16. Unfortunately, however, the stress waves in the shock-tube walls, generated by the primacord explosions, arrived at the gage station well ahead of the air blast, causing excessive oscillations on the force records. Attempts to shock mount the gage mounting proved unsuccessful, and it was finally found necessary to anchor the gage mount outside the shock tube with no contact between mount and tube walls (see Figure 7.17 and 7.18). The oscillations were thus greatly reduced, as may be noted in Figure 7.19.

Although the initial vibrations were considerably reduced, the records for the 10-inch-diameter force gages were still virtually

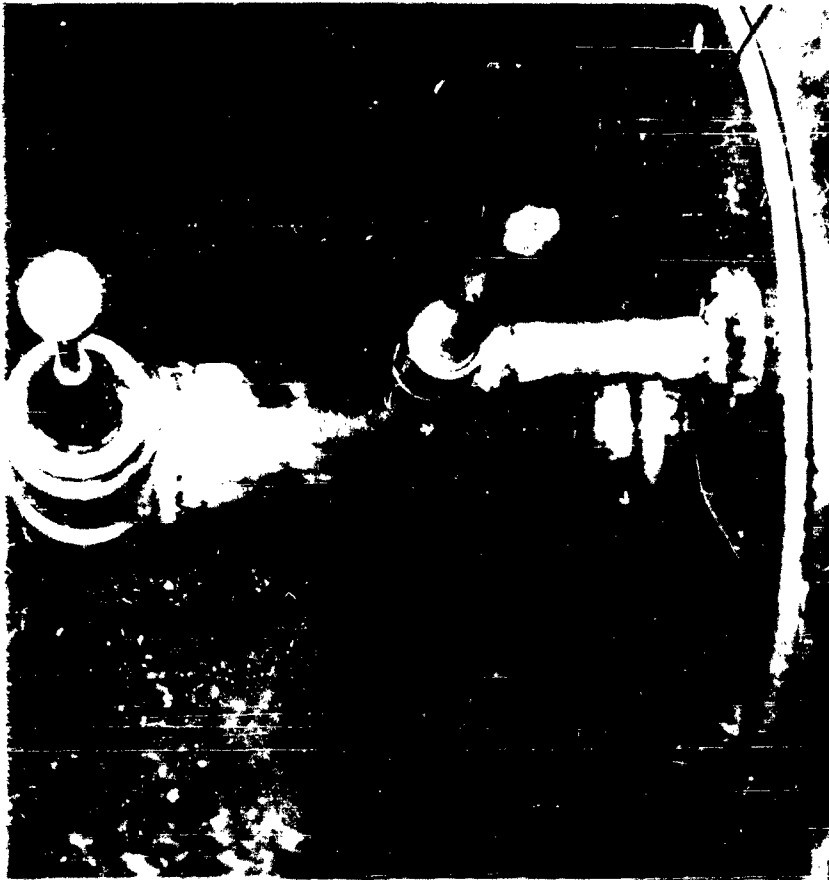


Figure 7.16 Three-inch Force Gage and SRI q Gage  
in ARF Shock Tube.

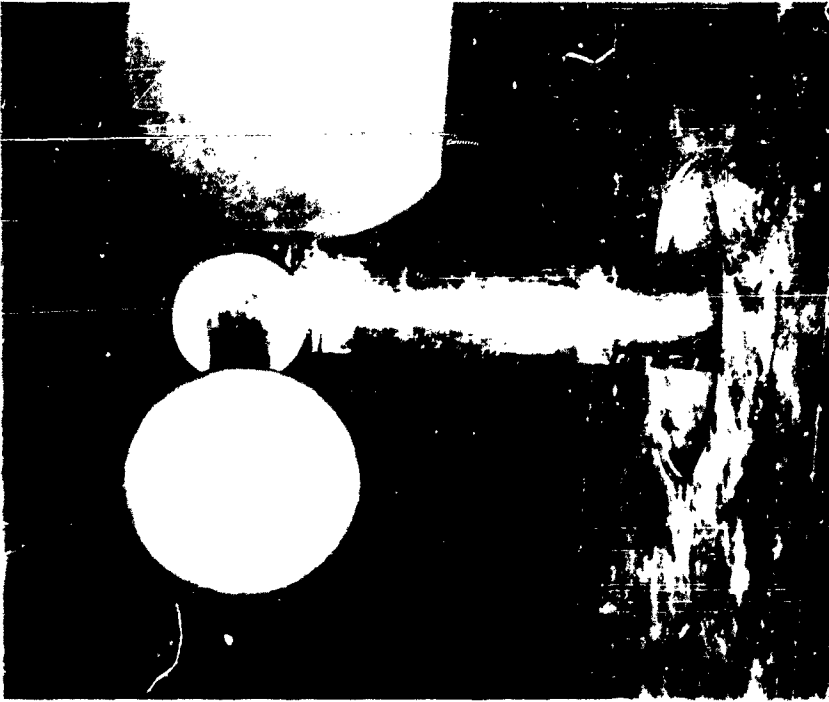


Figure 7.17 Ten-inch Force Gage in ARF Shock  
Tube - Mount Isolated from Shock Tube.

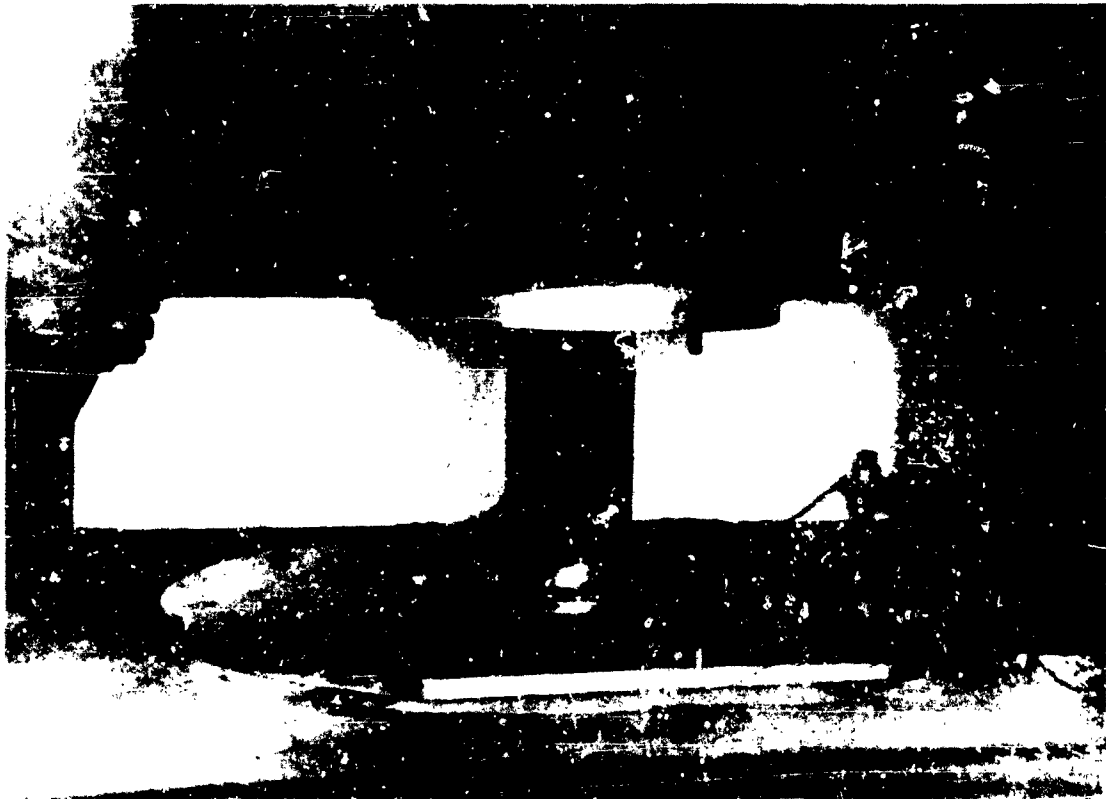


Figure 7.18 View of Gage Mount Anchored to Floor Outside of ARF Shock Tube.

BEFORE

AFTER

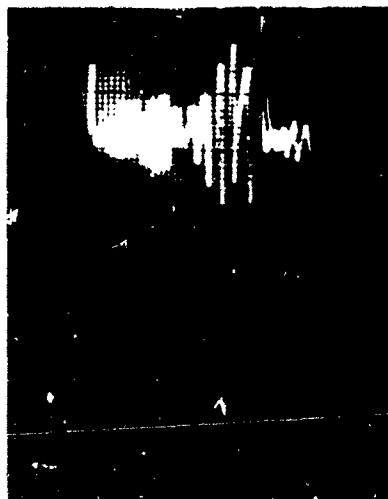


Figure 7.19 Force Records from Gage 11 (3-inch, 25-pounds) Before and After Shock Isolation of Gage Mount - 4 psi Overpressure - ARF Shock Tube.



unreadable (see Figure 7.20 and 7.21). Further attempts to damp the 10-inch gages resulted in overdamping of the net (faired) signal but did not remove these large-amplitude oscillations. (This undesirable damping characteristic of the Schaevitz force gages is believed due to the damping force being dependent on amplitude as well as velocity.) Since these 10-inch-gage records were of such poor quality, it was decided to defer the testing of the 10-inch gages until such time that the damping had improved or the available shock durations had increased considerably.

The remainder of the test program was carried out with the two 3-inch gages, Numbers 11 and 18, and with the SRI q gage. Figures 7.22 and 7.23 show typical records obtained with these gages. Note the reflection of the shock wave from the closed end of the shock tube, arriving some 40 msec after the initial shock.

7.2.2. Results. In the ARF shock tube, the 3-inch spherical force gages did not reproduce the behavior of vibrating either at about 550 cps or at their natural frequencies. Instead, as may be seen in Figure 7.24, the two 3-inch gages oscillated over a more or less continuous frequency band between their natural frequencies (330 cps to 380 cps) and 550 cps. Further, it was not possible to show correlation between frequency of vibration and drag coefficient. Thus, the identical force gages were found to respond in one manner in the BRL tests and in another in the ARF tests.

The plots of  $C_D$  versus time as each shot decays show a tendency to rise as the pressure drops, regardless of the initial pressure (see Figure 7.25). This may be valid response to a peaked shock (see the negative values illustrated in Figure 1.3), or the supporting pressure-time records may be incorrectly reading the shock decay. Figure 7.26 shows that the NOL check points on pressure fall somewhat (about 20 percent) below the ARF readings, and the measurements of q agree about as well. However, the NOL q records do not decay as rapidly as the q calculated from the ARF pressure records. Unfortunately, these discrepancies were not resolved, and the reasons for the shape of the  $C_D - P_s$  decay curves of Figure 7.25 must be the object of future study.

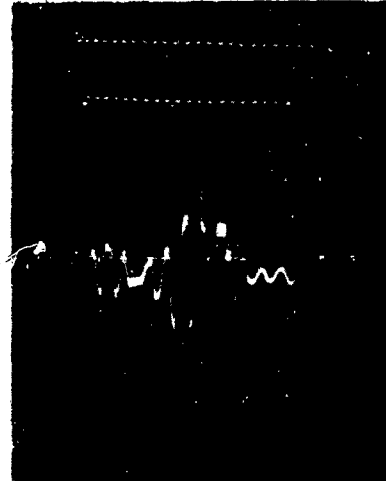
In general, only two shots were made at each pressure, hence the "estimated curves" of Figure 7.27. Reasonable curve shapes were selected to pass through the points of Figure 7.25, but the quantitative values of  $C_D$  are not believed to be reliable. It is recommended that this series of tests using peaked shock waves be repeated with about 10 shots at each pressure, with several cross checks made of the supporting pressure measurements.

### 7.3 NOL 40-BY-40-CM (16-INCH) WIND TUNNEL

7.3.1 Procedure. The NOL 40-by-40-cm wind tunnel was run in the subsonic and transonic ranges 5 and 6 December 1955 for wind tunnel tests of the 3-inch spherical force gages. As in the case of the BRL shock tube, the 10-inch-diameter spheres were considered too large for

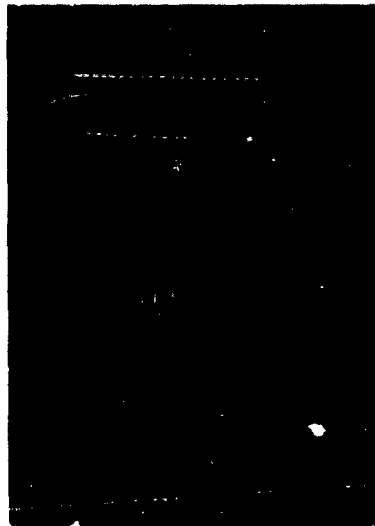


SHOT 18 — 4.0 PSI



SHOT 20 — 4.1 PSI

**BEFORE SHOCK ISOLATION OF GAGE MOUNT**



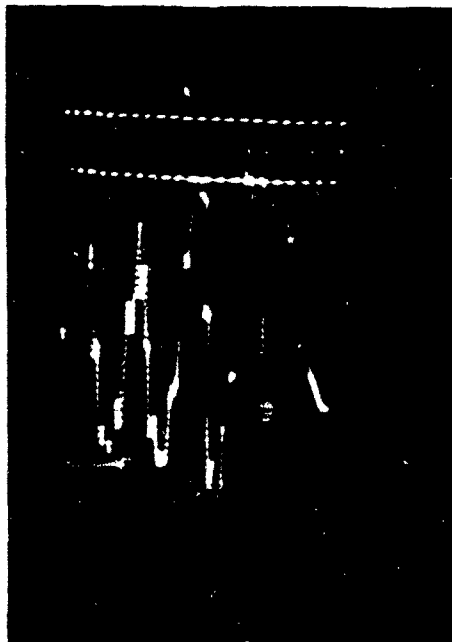
SHOT 21 — 4.9 PSI



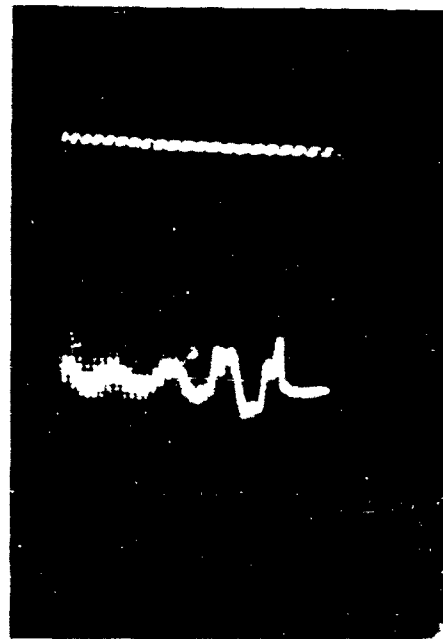
SHOT 22 -- 6.5 PSI

**AFTER SHOCK ISOLATION OF GAGE MOUNT**

Figure 7.20 Force Records from Gage 7 (30-inch, 400-pounds) in ARF Shock Tube.

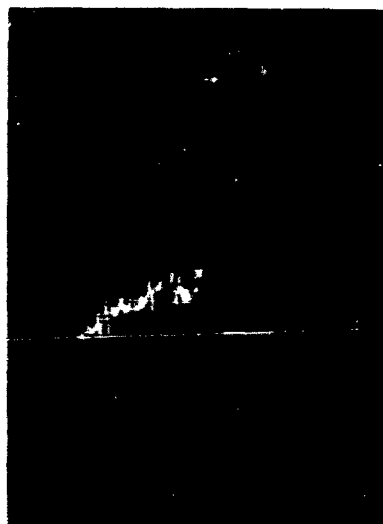


SHOT 30 — 5.0 PSI

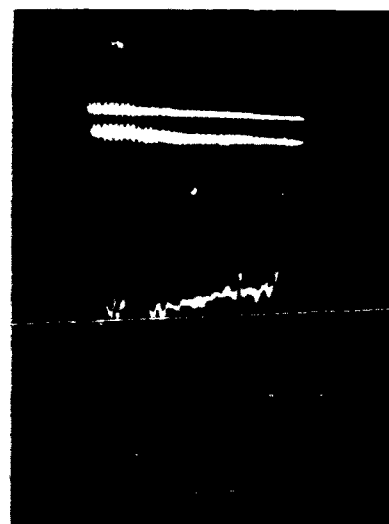


SHOT 31 — 1.0 PSI

Figure 7.21 Force Records from Gage 4 (10-inch, 35-pounds) in ARF Shock Tube.

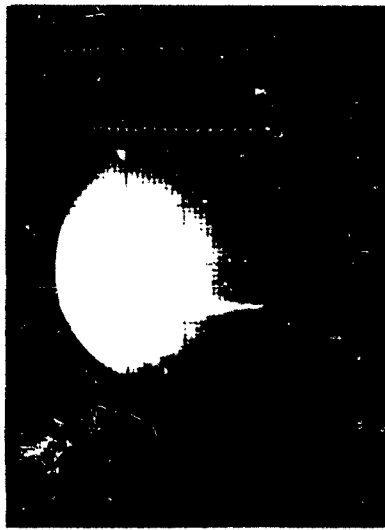


SHOT 29 — 11 PSI

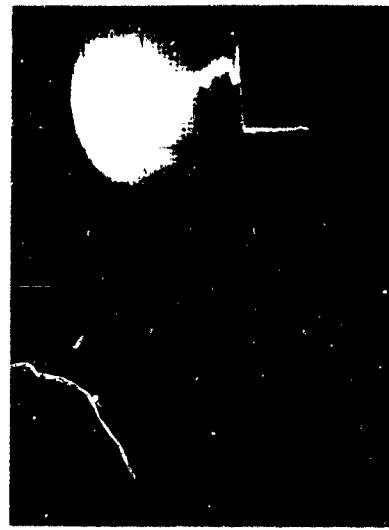


SHOT 42 — 22 PSI

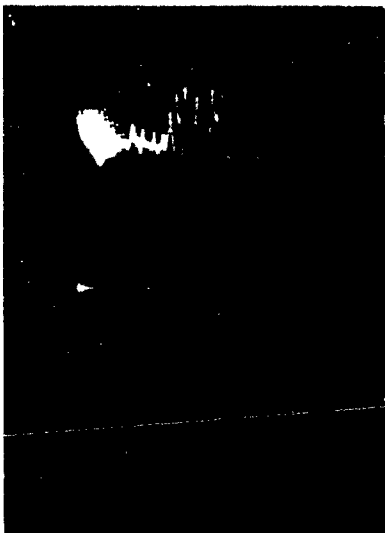
Figure 7.22 Force Records from Gage 11 (3-inch, 25 pounds) in ARF Shock Tube.



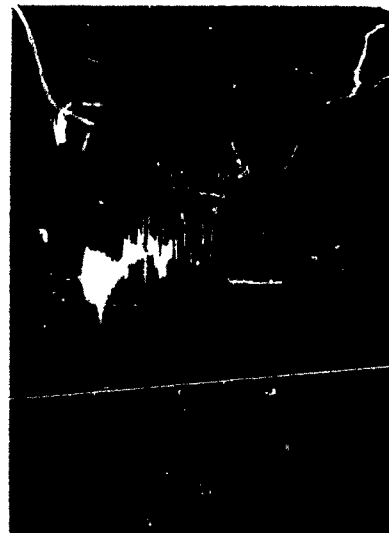
14 P — 4.4 PSI



15 P — 6.6 PSI



15 q — 6.6 PSI



16 q — 8.7 PSI

Figure 7.23 P and q Records from SRI Gage in ARF Shock Tube.

CONFIDENTIAL

134

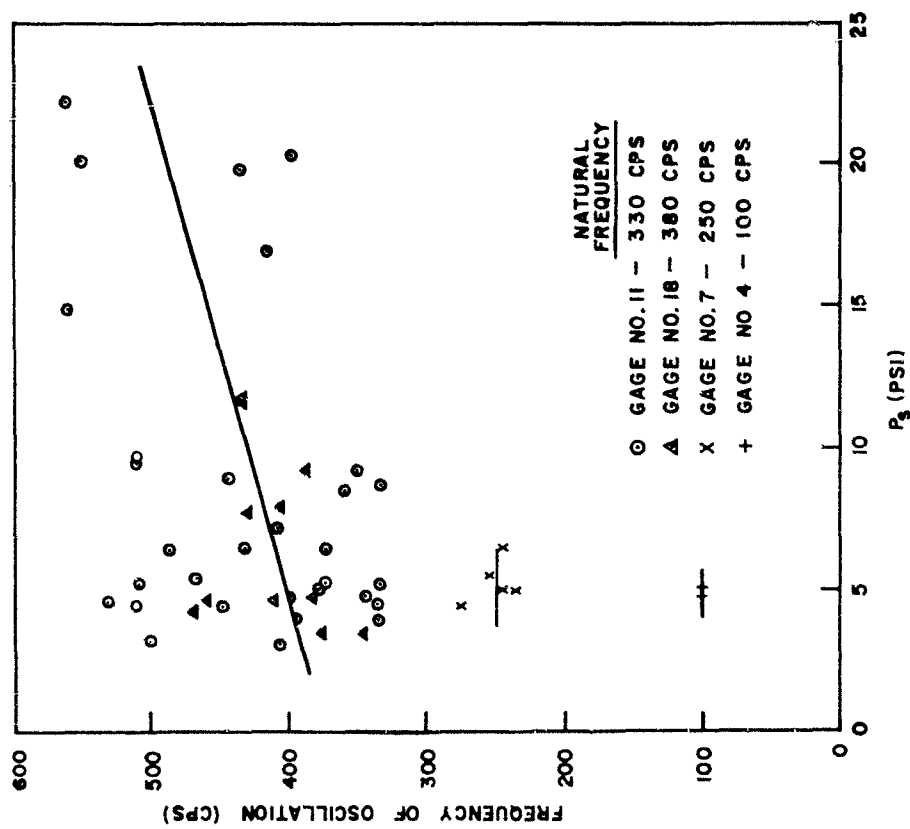


Figure 7.24 Frequencies of Oscillations on Force Records - ARF Shock Tube.

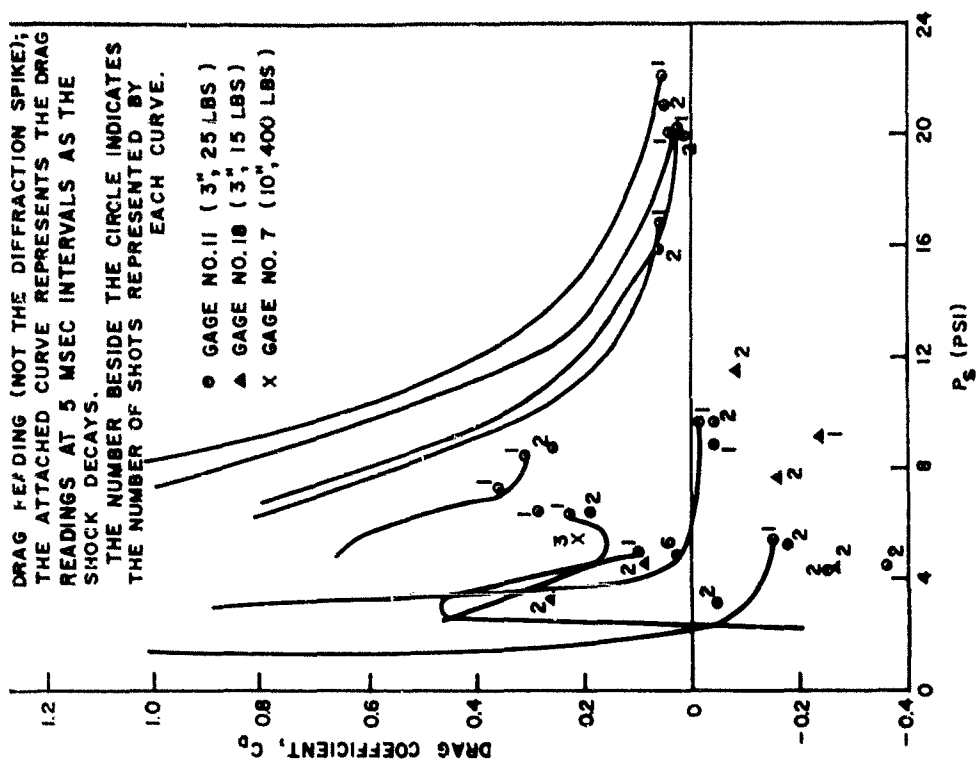


Figure 7.25 Drag Coefficients in ARF Shock Tube.

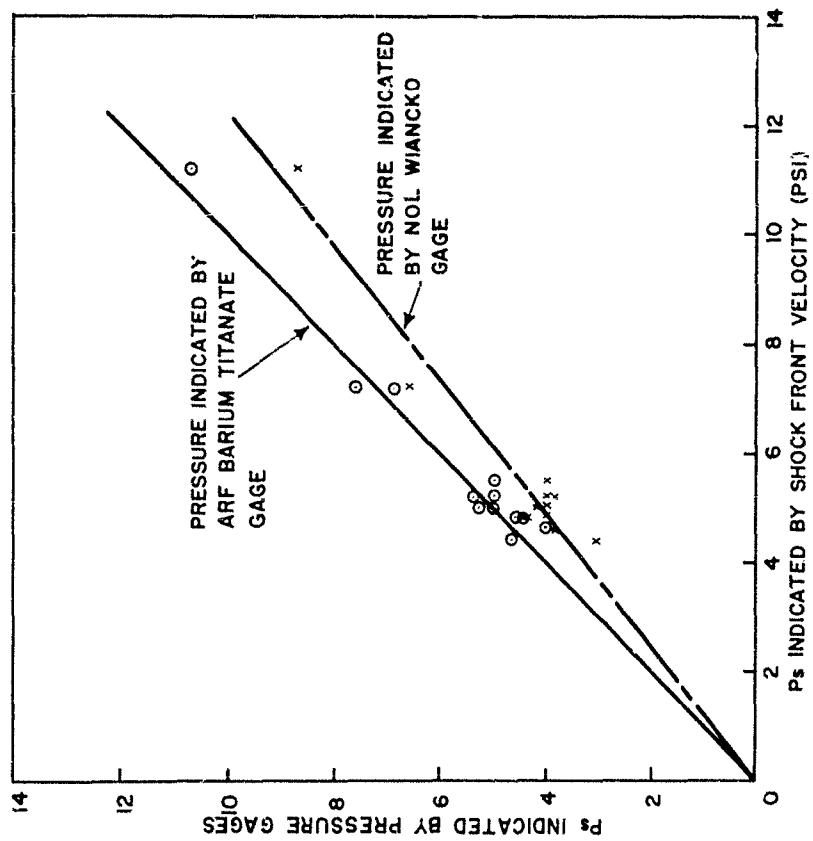


Figure 7.26 Comparison of Side-On Overpressures Recorded by Several Methods in APF Shock Tube.

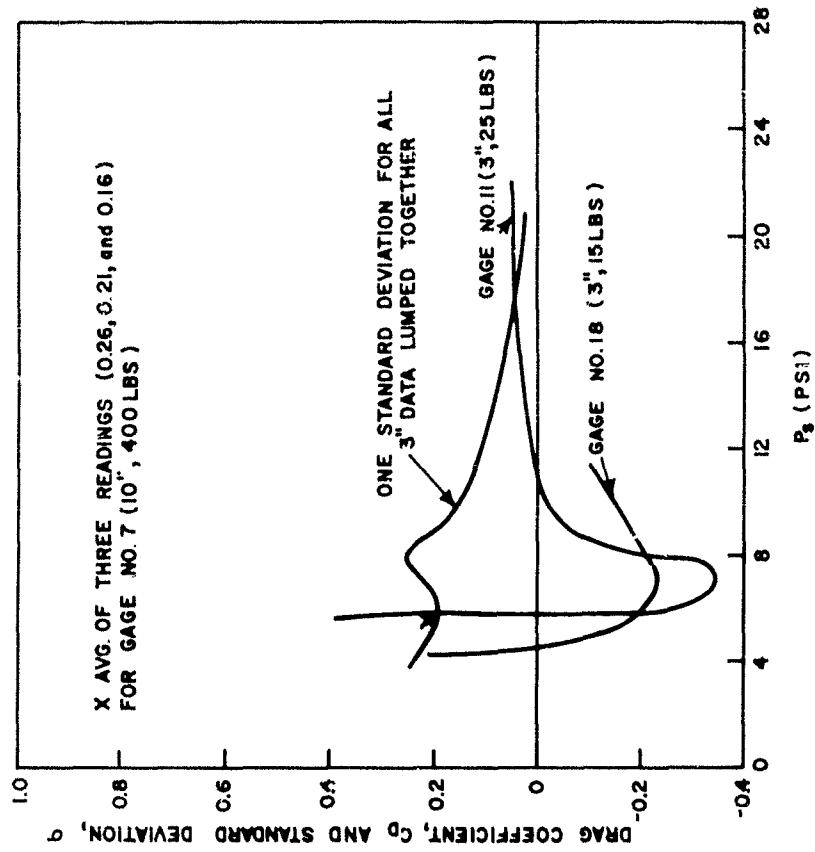


Figure 7.27 Estimated Curves for Initial Drag Coefficients and Standard Deviation of the Data in APF Shock Tube.

CONFIDENTIAL

this test facility, so the tests were restricted to performance of the 3-inch gages and the SRI  $q$  gage under steady wind-tunnel conditions.

The parameters under investigation in this test were Mach number, angle of attack, damping, and gage surface condition. Also of interest was the performance of a gage with base seal removed, since this would supply some clue as to the location of a leak when a gage is placed in a very-long-duration flow (see Figure 6.20).

Figure 7.28 shows a 3-inch force gage mounted in the wind tunnel at an angle of attack of about 15 degrees. The rack-driven sector was controlled externally and was used for angles between 0 (axial) and 30 degrees. This wind tunnel is the blowdown type, air being drawn from the atmosphere, down-stream through the test section, to a large, evacuated reservoir.

The instrumentation (see Figure 7.29) was somewhat different from that used in the shock-tube tests. Tape recordings were made of the force and pressure records throughout the relatively long-duration blows (up to about 30 seconds duration). Figure 7.30 shows a typical set of force records (Y and Z axes) as played back from the tape recording. Note the slow rise to the desired flow rate (lines 100 msec apart) and the fairly slow shut down, achieved by the quick-acting valve between test section and evacuated chamber. The time during each blow was long enough so that the reasonably steady force level could be read on an E-put meter. However, there was not enough time for more than one or two readings; and since the signal did vary dynamically (vibrations of the model), the tape readings remained the primary source of force data.

To record the model vibration frequencies and amplitudes, the oscilloscopes in Figure 7.29 were tripped at some time during the course of each blow, producing records such as those of Figure 7.31. Use of the scopes provided a further check on the force level measured on tape and E-put meter. A base line was placed on each scope film immediately before each blow, the distance from the centerline of the vibrating signal to the base line being proportional to the net force reading. Despite the possibility of drift of the scope base line, there was good agreement between the force readings obtained by all three methods.

Note that the ambient static pressure about the gage in the wind-tunnel tests is below atmospheric pressure (contrary to conditions existing in shock wave flow), since the total head of the air is equal to ambient atmospheric pressure. Figure 7.32 illustrates this fact and further demonstrates that  $q$  is about equal to the static underpressure. The high values of  $q$  indicated by the SRI gage on Figure 7.32 are probably due to the fact that the gage readings were not corrected for compressibility effects (see Equation 6.2).

7.3.2 Results. Frequencies of vibration of Gages 11 and 18 (natural frequencies of 330 and 380 cps, respectively) in response to wind-tunnel

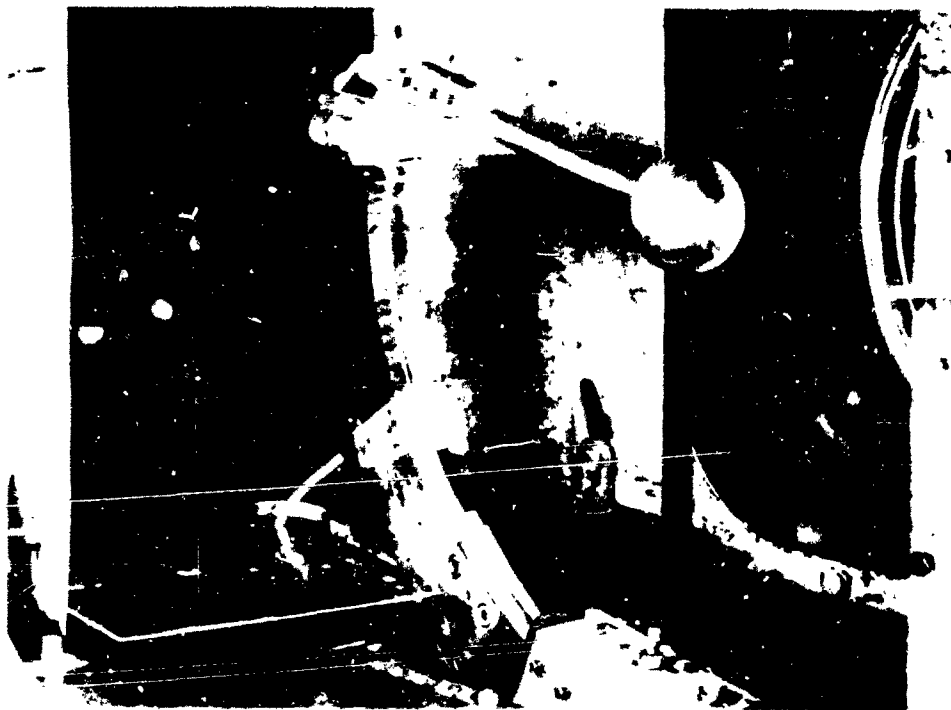


Figure 7.28 Three-inch Force Gage in NOL 40-by-40-cm Wind Tunnel.

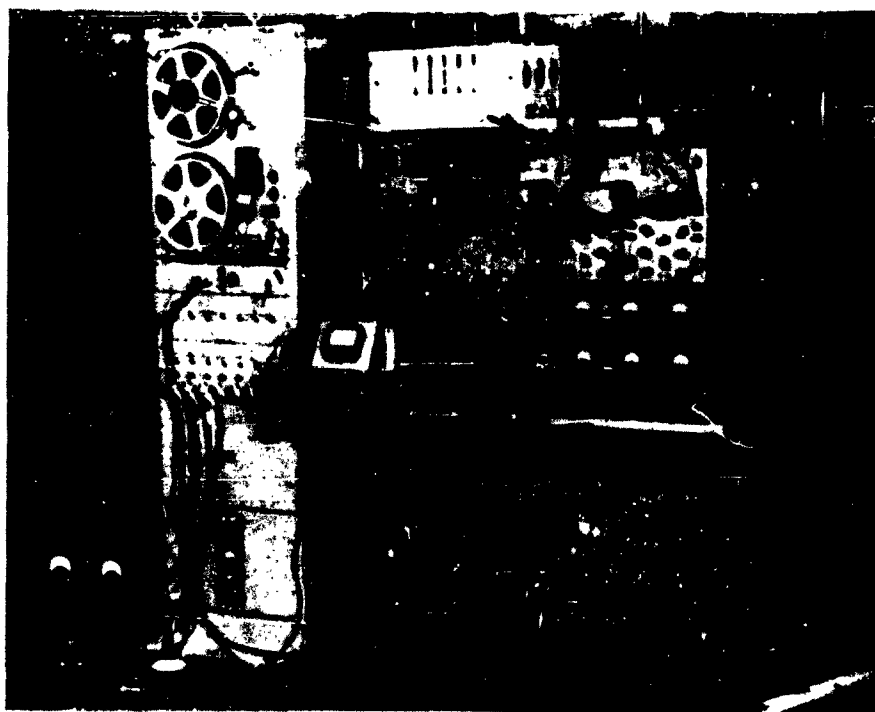


Figure 7.29 Instrumentation for NOL Wind Tunnel Test.



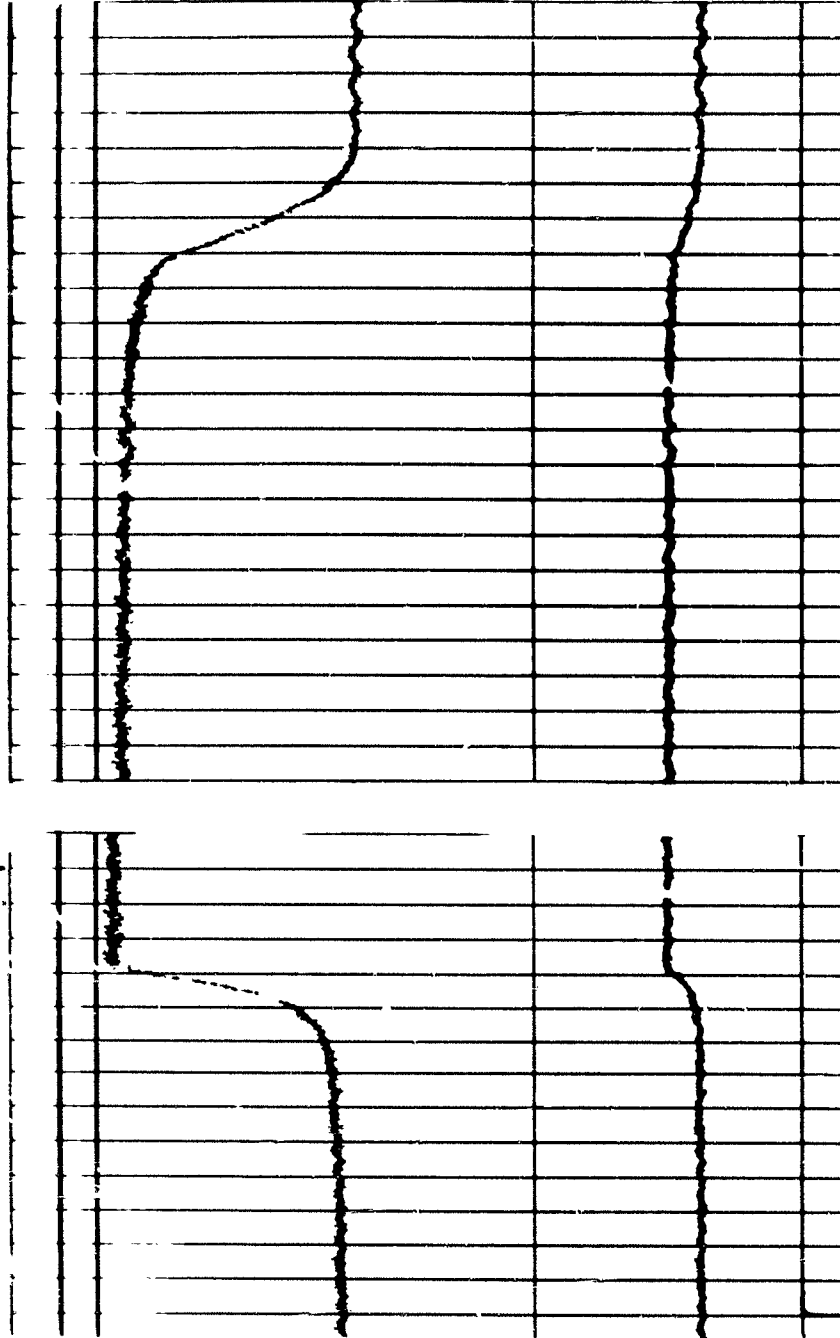
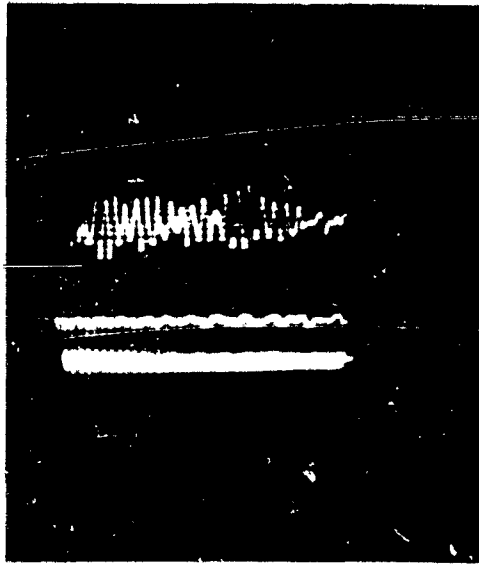


Figure 7.30 Tape Recordings of Force During Blow in  
NOL Wind Tunnel.



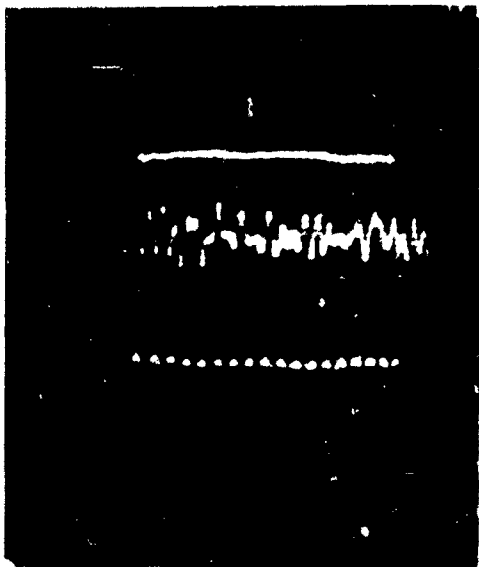
GAGE NO. 11

BLOW 18 -  $M=0.76$

BLOW 19 -  $M=0.59$

BLOW 20 -  $M=0.38$

BLOW 21 -  $M=0.19$



GAGE NO. 11

BLOW 52 -  $M=0.51$

400 - 1 - 1947

CONFIDENTIAL

Figure 7.31 Vibration of 3-inch Sphere in Steady Air Stream NOL Wind Tunnel.

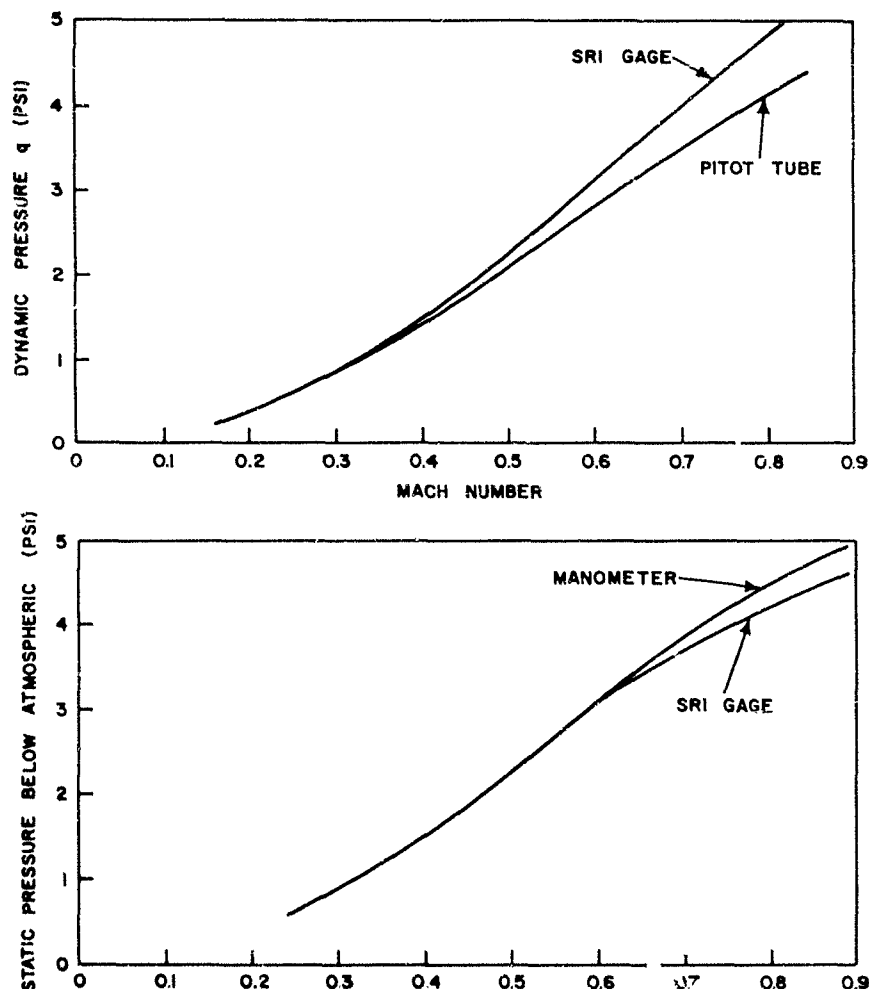


Figure 7.32 Comparison of SRI q Gage Readings with Wind Tunnel Instrumentation.

loads are shown in Figure 7.33. Although the mean response frequencies are above the gage natural frequencies, there is a considerable amount of scatter of the data, and the mean curve does not clearly fall on 550 cps as distinctly as the BRL shock-tube data. Further, no correlation between frequency and drag coefficient was found, again contrary to BRL shock-tube experience.

Amplitudes of vibration of the force gages are presented in Figure 7.34. These numbers are below those experienced in the shock tubes by about a factor of 5.

Figure 7.35 presents the drag-coefficient data. Any differences in drag coefficient due to variations in the parameters of damping, frequency, and moderate fouling of the shell are obscured by the scatter of the data. In the case of the gage without a base seal,

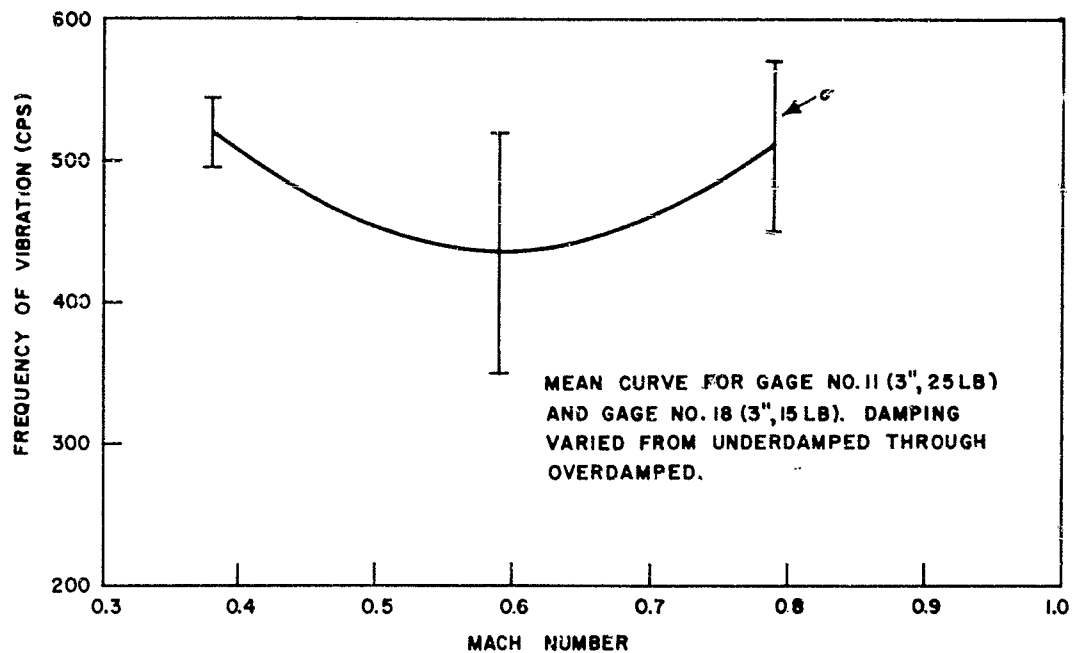


Figure 7.33 Frequencies of Vibrations on Drag Force  
Records - NOL Wind Tunnel.

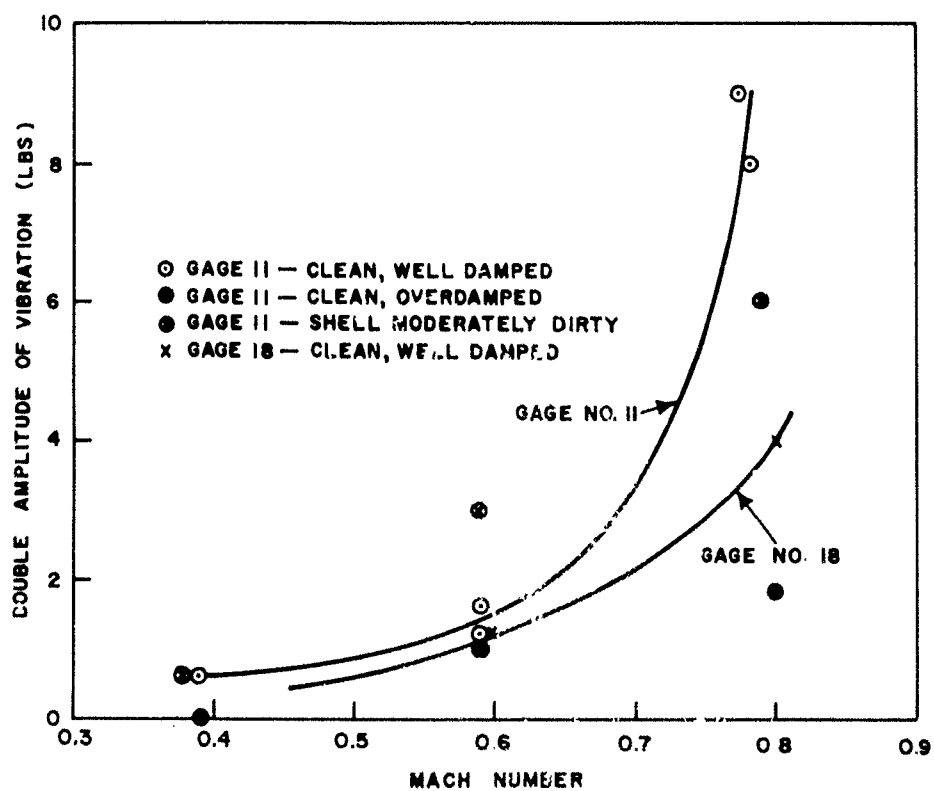


Figure 7.34 Amplitudes of Vibrations on Drag Force  
Records - NOL Wind Tunnel.

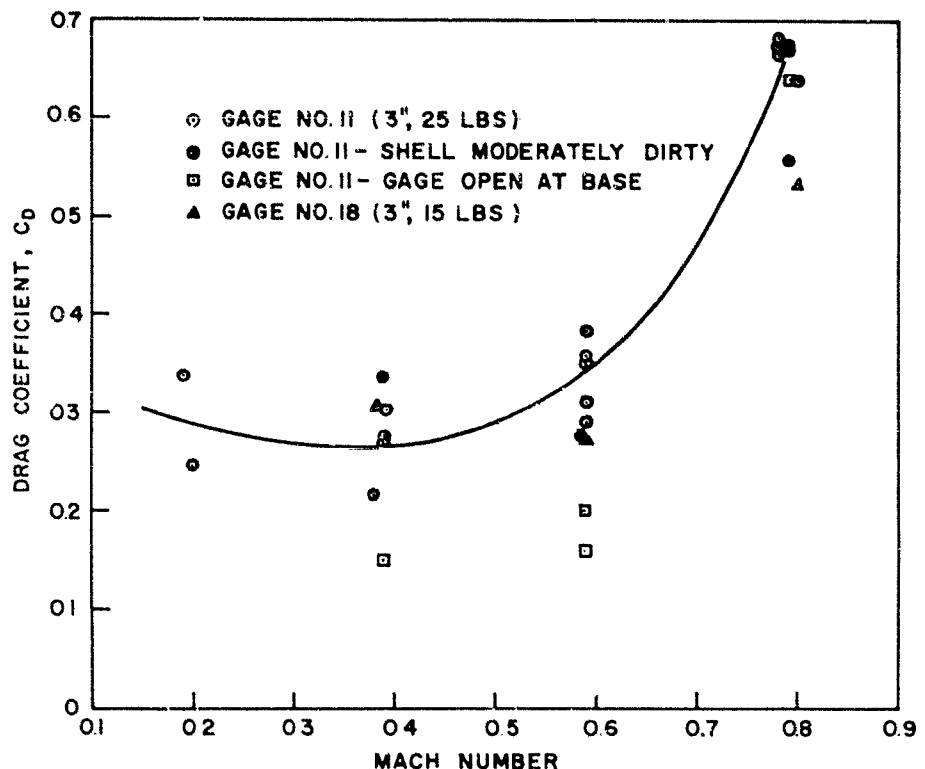


Figure 7.35 Drag Coefficients in NOL Wind Tunnel.

however, the results are considerably at variance with the mean-drag-coefficient curve, more so than is predicted by Equation 6.8 (which places the maximum error due to rapid leakage from any part of the shell at  $\pm 0.1$ ). The explanation may be that this difference in drag coefficient for the unsealed gage is not merely a static-pressure effect but represents an aerodynamic factor of significance in the critical Reynolds-number region. Some support for this explanation lies in the evidence that the differences exist at the low Mach numbers but not at  $M \approx 0.75$ .

#### 7.4 DTMB 7-BY-10-FOOT TRANSONIC WIND TUNNEL

**7.4.1 Procedure.** The same 3-inch and 10-inch force gages as had been used for the previous laboratory experimentation were used again in the 7-by-10-foot transonic wind tunnel at the David Taylor Model Basin (DTMB) from 3 to 13 April 1956. The test section was ample in size to accommodate the 10-inch sphere, as may be seen in Figures 7.36 and 7.37. The sting could be turned through the required yaw angles by remote control while the tunnel was in operation (the wind tunnel can be run continuously).

The parameters under investigation in this test were Mach number, angle of attack of flow, and Reynolds number. This latter parameter varies with the Mach number of the flow and, also, with size of sphere.

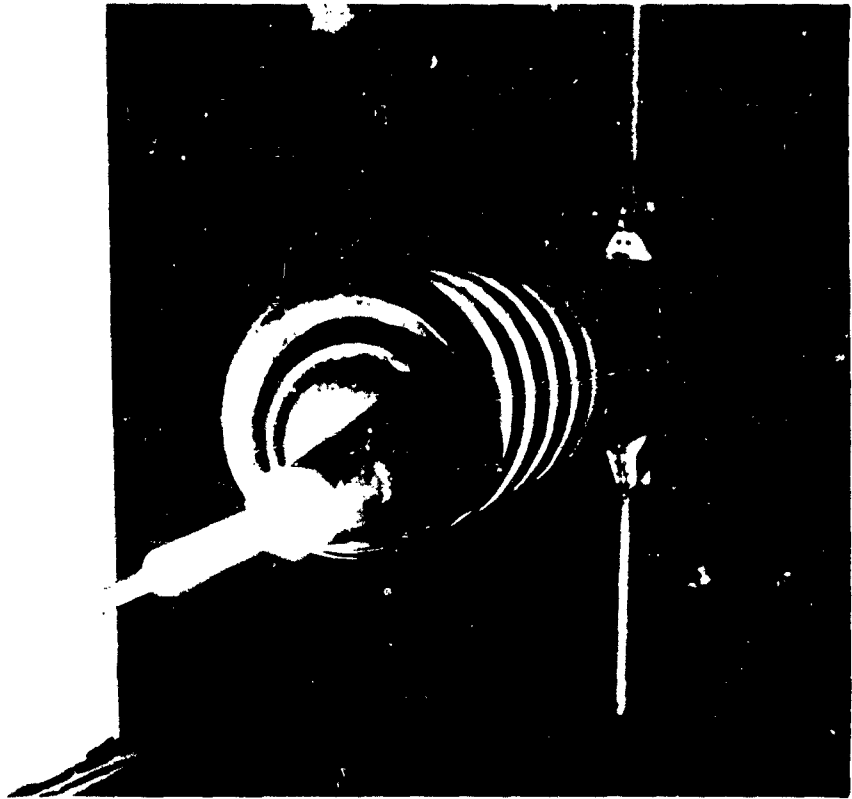


Figure 7.36 Three-inch Spherical Force Gage in DTMB  
7-by-10-foot Transonic Wind Tunnel.



Figure 7.37 Ten-inch Spherical Force Gage in DTMB  
7-by-10-foot Transonic Wind Tunnel.

The 7-by-10-foot test section permitted tests of the 10-inch spheres, as well as the 3-inch spheres. Besides serving to provide Reynolds number differences from the 10-inch spheres, the 3-inch spheres were expected to afford direct drag coefficient comparison between spheres in the NOL wind tunnel and the DTMB wind tunnel.

The DTMB transonic wind tunnel was run with the test section substantially at atmospheric pressure (test section vented, or TSV) and, also, with settling chamber vented (SCV), which produced subatmospheric pressures in the test section similar to NOL wind-tunnel test conditions. These two sets of conditions afforded some small variation in Reynolds number at the same Mach number and provided more information on pressure effects on these gages. Gross comparisons of the effects of R and static pressure on  $C_D$  were observed, and pressures were measured inside the 10-inch-force-gage shells to obtain data on leakage characteristics.

Some difficulty was encountered at first, due to the presence of dust in this new facility (NOL was the first user of the DTMB transonic wind tunnel). This resulted in sand-blasting of the shell of Gage 18 (see Figure 7.38). After several days of cleaning and filtering, however, this source of difficulty disappeared, and the remainder of the program was completed as planned.

The instrumentation (see Figure 7.39) was similar to that used for the NOL wind-tunnel test. For this continuously running tunnel, however, the readings of the E-put meter were of great value, because many readings could be taken during each run and the variations (due to vibration, etc) could be averaged out. Figure 7.40 shows typical vibration records taken by tripping the scopes during a run, as had been done during the NOL test. Besides the scope vibration records and E-put readings, the drag forces were recorded on tape for a considerable length of time during each run.

7.4.2 Results. Figure 7.41 presents the data on frequencies of vibrations of 10-inch Gages 4 and 7, and of 3-inch Gage 11 in the DTMB transonic wind tunnel. Comparison of the DTMB data for Gage 11 with NOL data for Gages 11 and 18 (see Figure 7.33) shows that the mean DTMB curve is below the mean NOL curve, although the difference is not too significant in view of the scatter in the data.

The performance of the 10-inch gage can only be compared with the results of the ARF 6-foot shock tube (Figure 7.24). Gage 4 vibrated at its natural frequency of 100 cps in both tests; Gage 7 vibrated at its natural frequency of about 250 cps in the ARF test but vibrated somewhat below 200 cps in the DTMB test.

Amplitudes of vibrations of the force gages are presented in Figure 7.42. Good agreement is obtained between DTMB and NOL data (Figure 7.34), but both 3-inch- and 10-inch-wind-tunnel vibration amplitudes are about a factor of 5 lower than those experienced in the shock tubes. Note that the 400-pound Gage 7 and 35-pound Gage 4

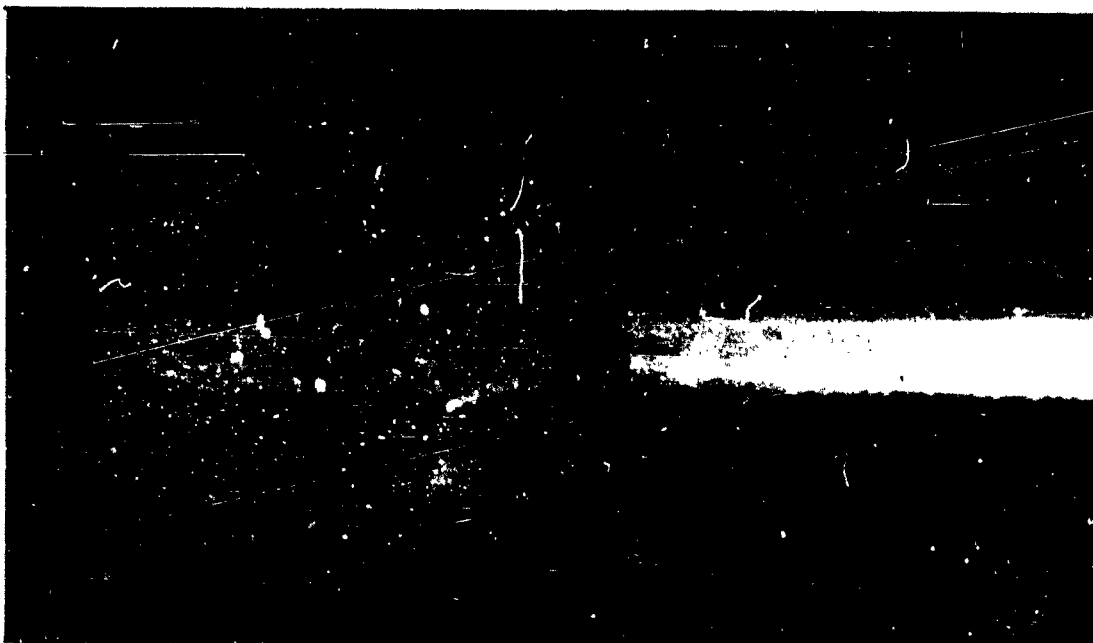


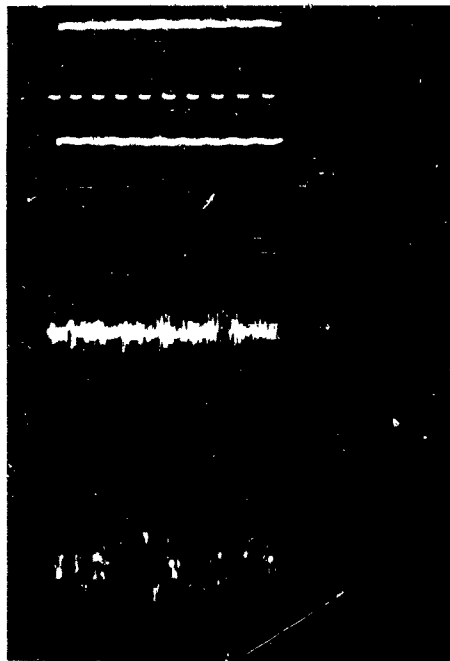
Figure 7.38 Sand-Blasting of Shell of 3-inch Sphere  
Due to Dust in DTMB Transonic Wind Tunnel.



Figure 7.39 NOL Instrumentation - Force Gage Test at  
DTMB Transonic Wind Tunnel.

CONFIDENTIAL



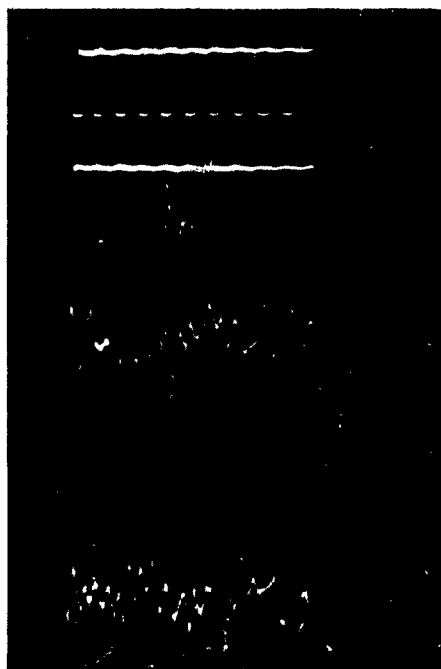


GAGE NO. 11 (3", 25 LBS)

RUN 19 —  $\alpha = 0^\circ$ ,  $M = 0.603$

RUN 20 —  $\alpha = 0^\circ$ ,  $M = 0.749$

60  $\sim$  TIMING



GAGE NO. 4 (10", 35 LBS)

RUN 25 —  $\alpha = 15^\circ$ ,  $M = 0.403$

RUN 22 —  $\alpha = 0^\circ$ ,  $M = 0.406$

Figure 7.40 Vibrations of Spheres in Steady Flow at DTMB Transonic Wind Tunnel.

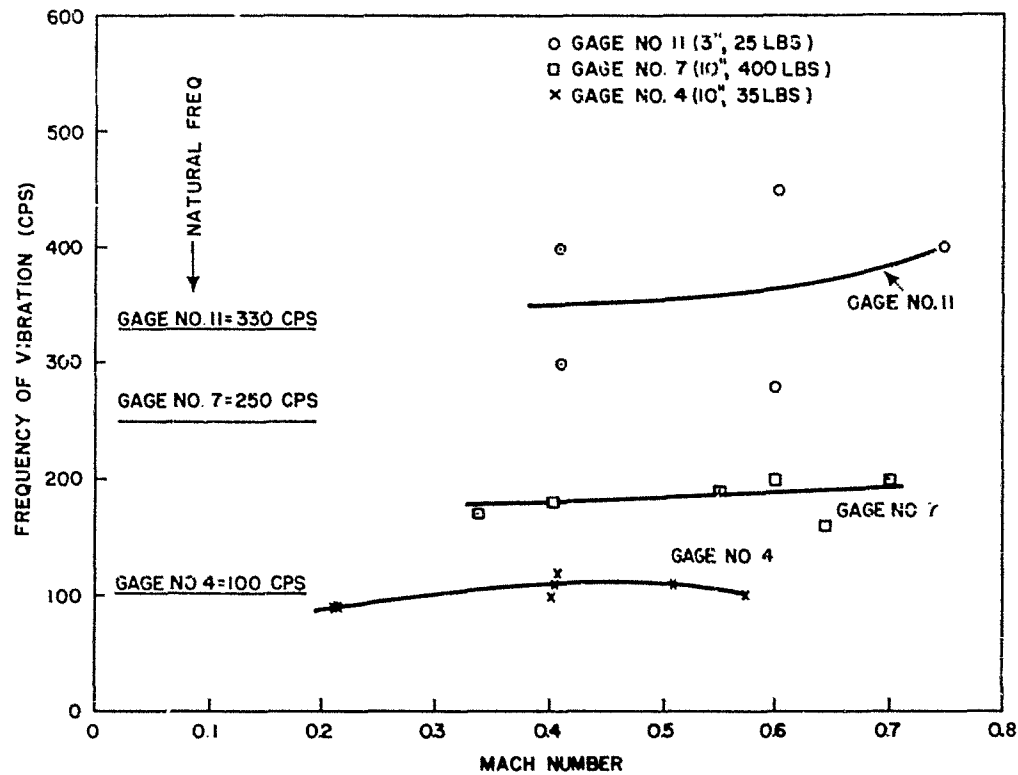


Figure 7.41 Frequencies of Vibrations on Drag Force Records DTM Transonic Wind Tunnel.

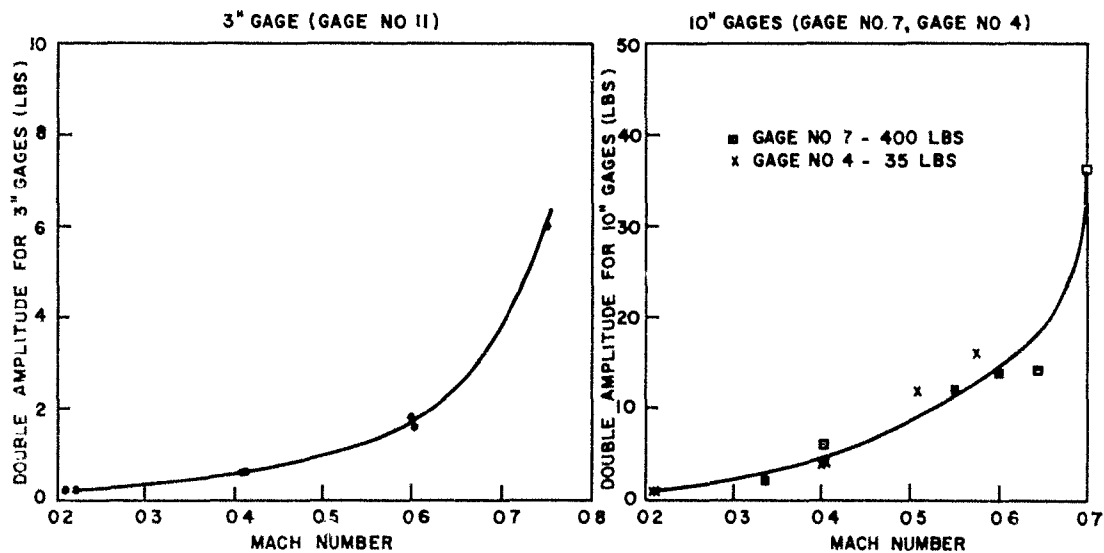


Figure 7.42 Amplitudes of Vibrations on Drag Force Records DTM Transonic Wind Tunnel.

CONFIDENTIAL

vibrated with the same force amplitude, even though the amplitude of motion in the air stream of the 35-pound gage is about 10 times that of the 400-pound gage. The conclusion is drawn from this fact that the model motion is not usually an important factor in drag force considerations.

Figure 7.43 presents the DTMB wind-tunnel data on drag coefficients. The small changes in Reynolds number induced by venting the test section

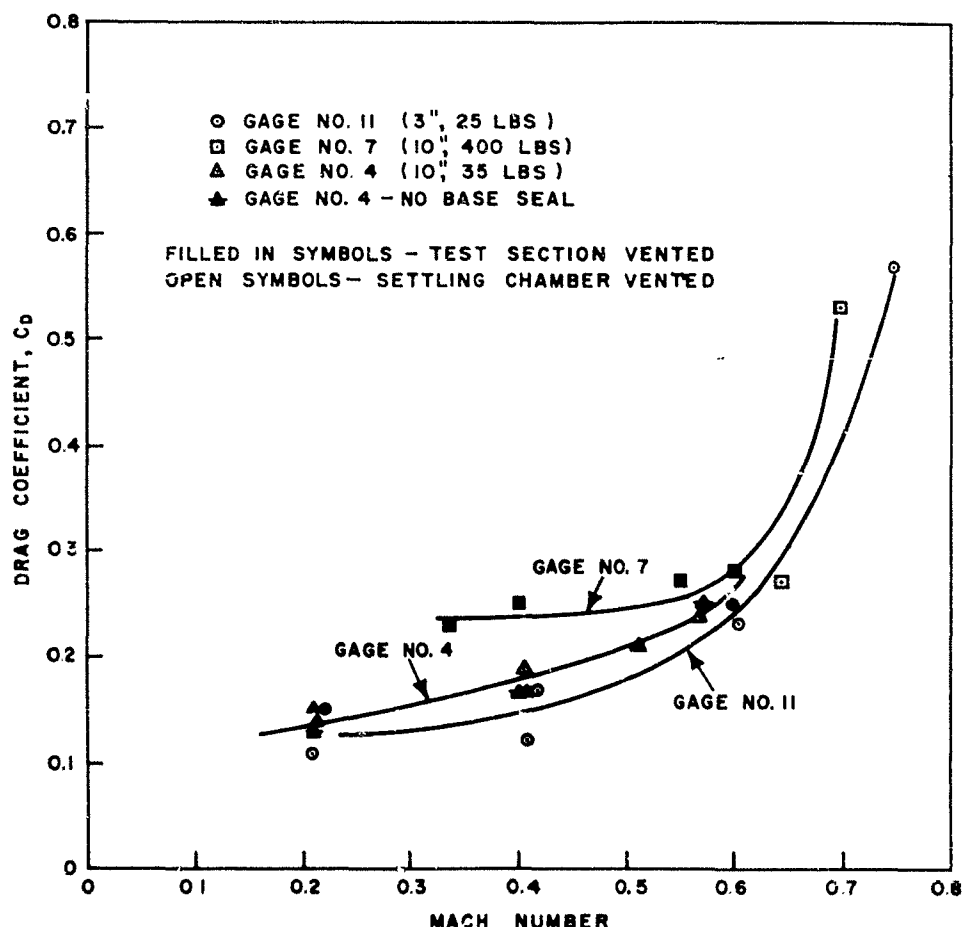


Figure 7.43 Drag Coefficients in DTMB 7-by-10-foot Transonic Wind Tunnel.

appeared to have little effect on drag coefficient, as did the removal of the base seal of Gage 4. This latter result is in harmony with the internal pressure measurements on Gage 4, which showed little change in internal pressure when the Pliobond base seal was removed.

Comparison of drag coefficients obtained at DTMB with those at NOL (Figure 7.46) shows the NOL data higher than the DTMB data. This difference may well be due to different gage leakage characteristics during the different tests. However, this question cannot be resolved,

since the internal pressures were not measured for the 3-inch-diameter gages, and it was the 3-inch gages which were tested in both facilities. For more-precise wind-tunnel data (better than the  $\pm 0.1$  on  $C_D$  for a leaking gage), more tests are recommended with a redesigned force gage or with internal pressure measurements in existing gages.

## 7.5 DISCUSSION OF RESULTS

To compare gage-performance data in wind tunnels and in shock tubes, it is necessary to reduce the independent variables of Mach number and side-on overpressure to some common basis. Following the lead of the aerodynamicists in order to make use of the published data on drag coefficients (see Figure 6.1), the independent variables selected for purposes of presentation are Mach number and Reynolds number. Since the drag phase of the loading is of principal concern, the following analysis of flow conditions behind the shock front is made, Mach number relating the motion of the particles within the wave with the local speed of sound within the wave.

Defining symbols:

- C - Speed of sound
- D - Diameter of sphere
- M - Mach number =  $u/C$
- $P_s$  - Side-on overpressure
- R - Reynolds number =  $\rho Du/\nu$
- $R_o$  -  $\rho_o DC_o/\nu_o$
- T - Temperature
- u - Particle velocity in shock wave
- $\nu$  - Viscosity of air
- $\rho$  - Density of air

Subscript o refers to ambient conditions before passage of the shock wave.

In order to obtain an expression for Reynolds number in terms of some ambient preshock parameter, the artificial Reynolds number  $R_o = \rho_o DC_o/\nu_o$  is introduced, and the variation of  $R/R_o$  with shock strength is considered. First consider the individual ratios involved in

$$R/R_o = \left\{ \frac{\rho}{\rho_o} \right\} \left\{ \frac{u}{C_o} \right\} \left\{ \frac{\nu_o}{\nu} \right\} :$$

$$\frac{\rho}{\rho_o} = \frac{6 \frac{P_s}{P_o} + 7}{\frac{P_s}{P_o} + 7} \quad (7.1)$$

$$\text{and } \left\{ \frac{u}{C_o} \right\}^2 = \frac{25}{7} \frac{(P_s/P_o)^2}{6P_s/P_o + 7} \quad (7.2)$$

through application of the Rankine-Hugoniot equations for a clean shock. A simple expression for viscosity of air, which closely fits the data of Reference 38 for the temperatures involved in the range of shock overpressures through about 30 psi:

$$\nu = 2.60 (T)^{0.75} \text{ Micropoises } (T \text{ in } ^\circ K) \quad (7.3)$$

may be combined with the Rankine-Hugoniot equation:

$$\frac{T}{T_0} = \left( \frac{P_s}{P_0} + 1 \right) \frac{\left\{ \frac{P_s}{P_0} + 7 \right\}}{\left\{ 6 \frac{P_s}{P_0} + 7 \right\}} \quad (7.4)$$

to yield the expression

$$\frac{\nu}{\nu_0} = \left[ \left( \frac{P_s}{P_0} + 1 \right) \frac{\left\{ \frac{P_s}{P_0} + 7 \right\}}{\left( 6 \frac{P_s}{P_0} + 7 \right)} \right]^{0.75} \quad (7.5)$$

Combining Equations 7.1, 7.2, and 7.5

$$\frac{R}{R_0} = \frac{\left\{ 6 \frac{P_s}{P_0} + 7 \right\}^{1.25} \sqrt{\frac{25}{7}} \frac{P_s}{P_0}}{\left\{ \frac{P_s}{P_0} + 7 \right\}^{1.75} \left\{ \frac{P_s}{P_0} + 1 \right\}^{0.75}} \quad (7.6)$$

Fortunately, the numerical value of the expression

$$\frac{\sqrt{\frac{25}{7}} \left( 6 \frac{P_s}{P_0} + 7 \right)^{1.25}}{\left\{ \frac{P_s}{P_0} + 7 \right\}^{1.75} \left\{ \frac{P_s}{P_0} + 1 \right\}^{0.75}}$$

remains remarkably constant for the overpressure range of interest, namely,  $0.1P_0 < P_s < 2P_0$ :

$P_s/P_0$	0.1	0.2	1.0	2.0
$P_s$ , for $P_0 = 14.7$ psi	1.47	2.94	14.7	29.4
$\frac{\sqrt{\frac{25}{7}} \left\{ 6 \frac{P_s}{P_0} + 7 \right\}^{1.25}}{\left\{ \frac{P_s}{P_0} + 7 \right\}^{1.75} \left\{ \frac{P_s}{P_0} + 1 \right\}^{0.75}}$	0.715	0.720	0.728	0.701

Using 0.72 as a representative value:

$$\frac{R}{R_0} = 0.72 \frac{P_s}{P_0} \quad (7.7)$$

This relationship may be useful when scaling from ambient conditions to sea level. For standard conditions, with  $C_0 = 1130$  fps,

$\rho_0 = 0.075$  lb/ft<sup>3</sup>, and  $\nu_0 = 185$  micropoises for  $T_0 = 70^\circ\text{F}$

$$\begin{aligned} R_0 &= 6.82 \times 10^6 D, \text{ with } D \text{ in feet} \\ \text{and } R &= 4.91 \times 10^6 D \frac{P_s}{P_0} \end{aligned} \quad (7.8)$$

Figure 7.44 contains a plot of Equation 7.8 and also a plot of local Mach number,  $u/C$ , obtained from the Rankine-Hugoniot equation

$$M^2 = \frac{25}{7} \frac{(P_s/P_0)^2}{(P_s/P_0 + 1)(P_s/P_0 + 7)} \quad (7.9)$$

On this same figure are included empirical curves of  $R$  versus  $M$  for the NOL and DTMB wind tunnels.

Converting the curves for shock-tube vibration frequency from a  $P_s$  to a Mach number plot through the use of Figure 7.44, the comparison may now be made between shock-tube and wind-tunnel vibration frequencies. Figure 7.45 contains this data from the ARF and BRL shock tubes and the DTMB and NOL wind tunnels. The 10-inch-diameter gages (Numbers 4 and 7) appear to vibrate at about their natural frequencies of 100 cps and 250 cps, respectively, both in the shock tube and the wind-tunnel environment.

Amplitudes of vibration were about five times as high in the shock tubes as in the wind tunnels. (The shock-tube readings were taken shortly after the diffraction-induced oscillations had died down.) This may only be due to the short duration of the shock-tube flow, however, rather than a fundamental difference between shock-wave and wind-tunnel flow.

Many tests were made in the shock tubes and wind tunnels with the sting at angles of attack to the flow other than 0 degrees. The sting effect is such that a small angle of attack induces a large indicated angle of force (calculated from the orthogonal components of force). These indicated angles are very sensitive to Mach number, Reynolds number, etc. The data obtained in the shock tubes and wind tunnels were widely scattered; the spherical force gage with a sting is suitable for indication of direction of blast flow only if dynamically calibrated.

For purposes of comparing drag coefficients, the wind-tunnel data are averaged in Figure 7.46 (no explanation is offered at present for

CONFIDENTIAL

152

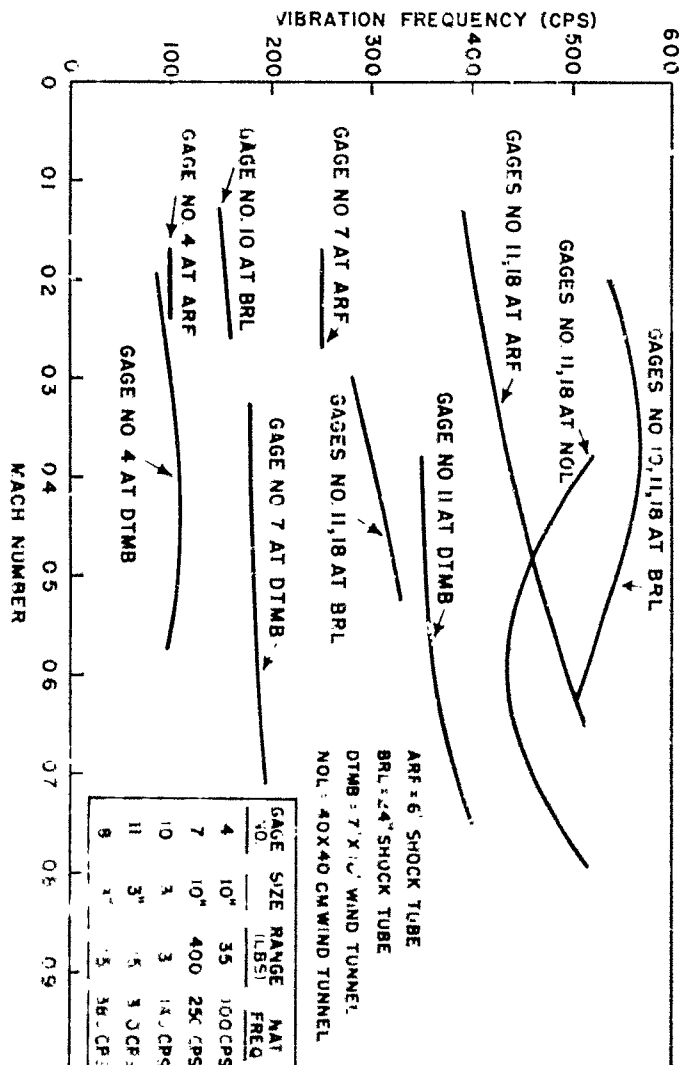
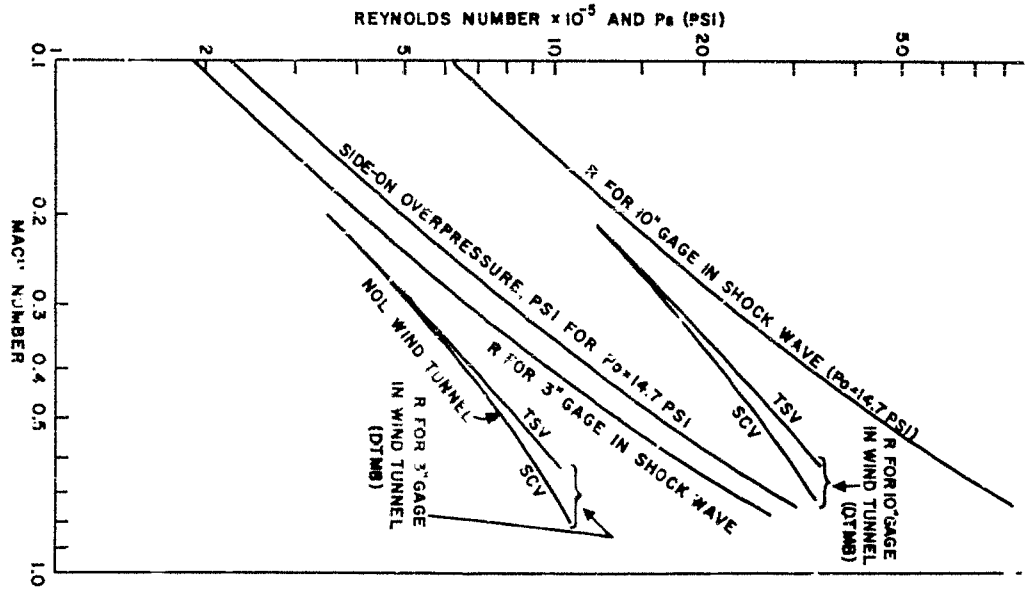


Figure 7.4: Relationship between  $P_0$  and  $M$  for various gage sizes and locations.

Figure 7.5: Vibration frequency records in shock tube and wind tunnel.

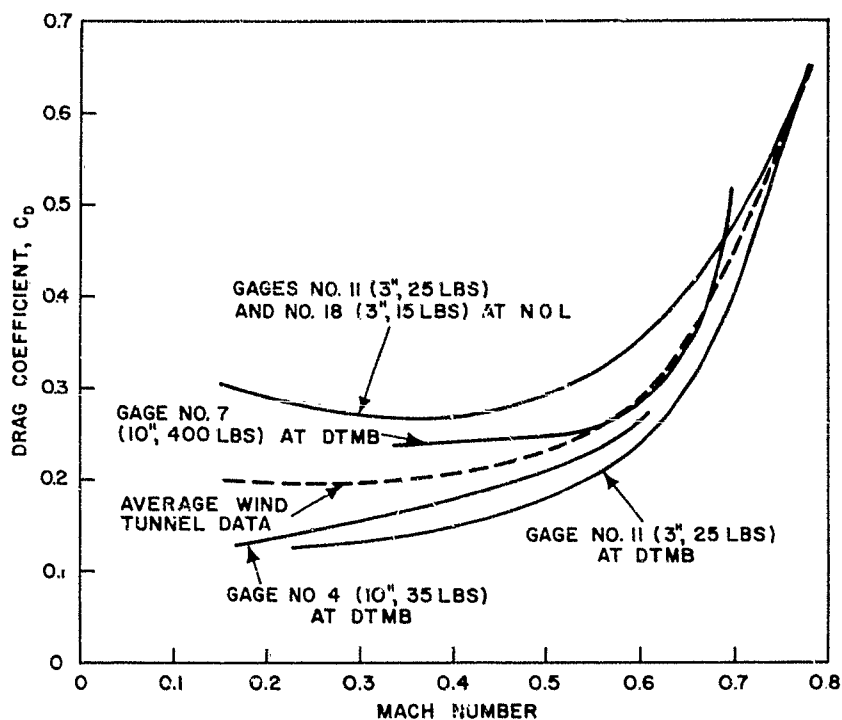


Figure 7.46 Comparison of Drag Coefficients Obtained in DTMB and NOL Wind Tunnels.

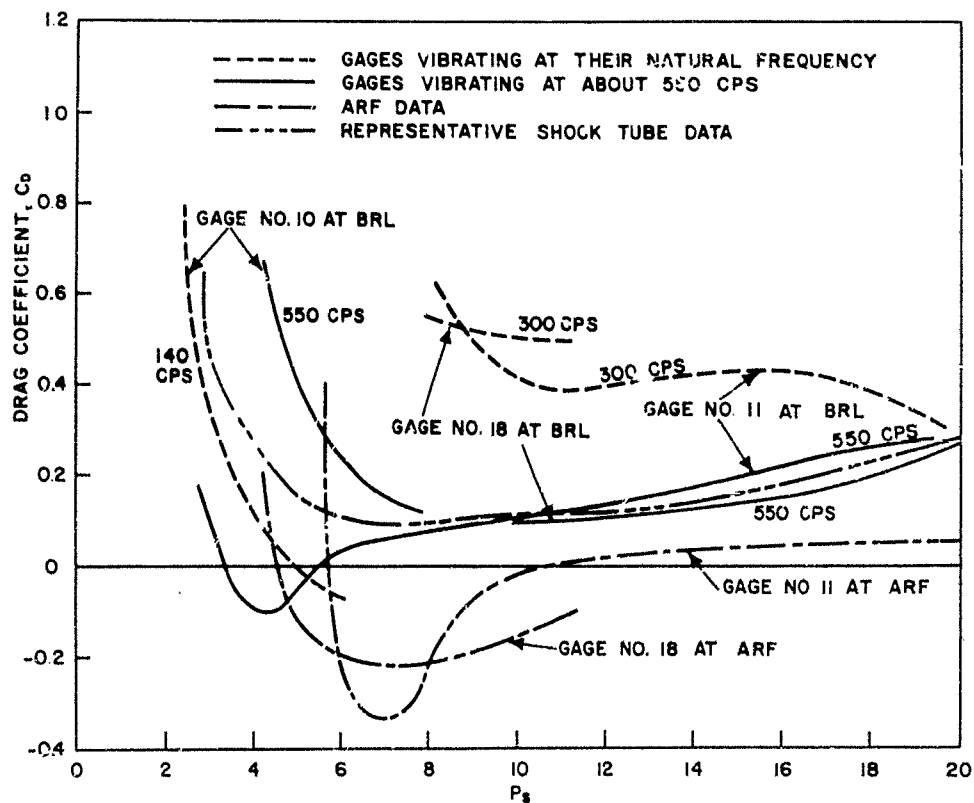


Figure 7.47 Comparison of Drag Coefficients Obtained in ARF and BRL Shock Tubes.



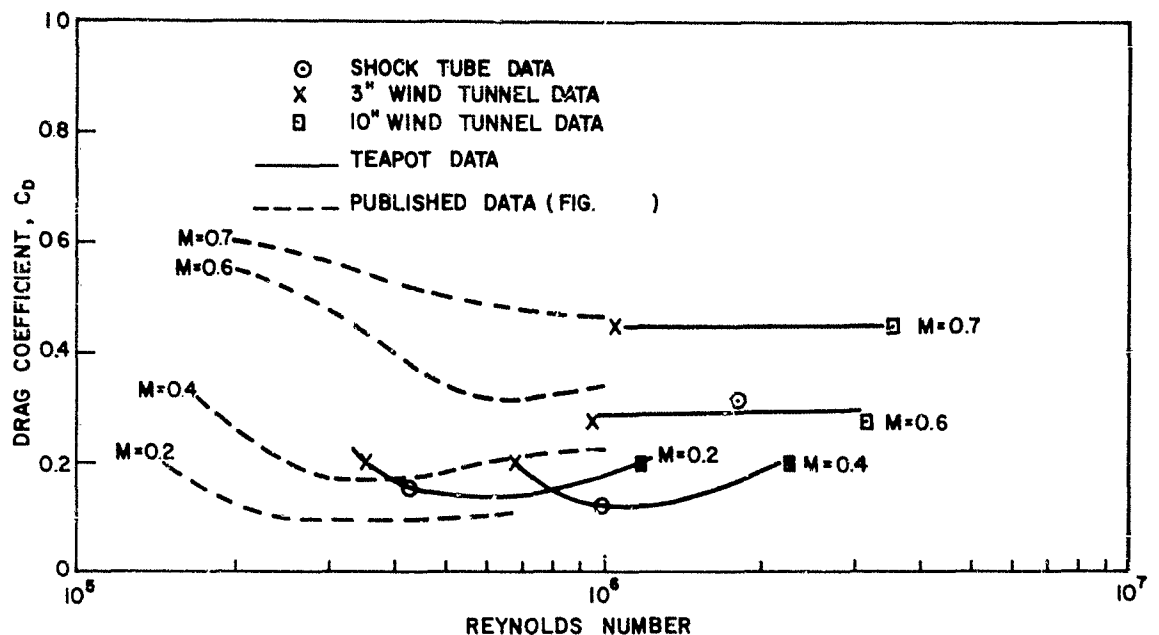


Figure 7.48 Comparison of Wind Tunnel and Shock Tube Drag Coefficients for Spheres.

the differences between DTMB and NOL wind-tunnel data), and the shock-tube data are averaged in Figure 7.47. In the case of the shock-tube data, only those at the 550-cps mode obtained at BRL are averaged, since the natural-frequency-mode data depend on the natural frequency of the individual gage, and the ARF shock-tube data are provisionally discarded as being either unreliable (too few readings at a point and conflicting pressure measurements) or a function of rate of decay of the peaked shock. These averaged curves are transposed to a common Mach-number and Reynolds-number basis through the use of Figure 7.44, thus allowing a final comparison as presented in Figure 7.48.

Considering the process by which the Teapot curves of Figure 7.48 were derived and the tremendous spread of the previously published data on drag coefficients of spheres (with and without stings), the agreement is truly remarkable. The tentative conclusion is drawn that wind-tunnel and shock-tube drag coefficients are the same, after some 75 transit times have elapsed. However, this time for establishment of the drag phase is not well established, and there is much scatter in the Teapot laboratory data. For these reasons, the Teapot laboratory program must be considered as a starting point in a program to establish a sound basis for engineering approximations of drag loading of structures.

## Chapter 8

# CONCLUSIONS AND RECOMMENDATIONS

### 8.1 CONCLUSIONS

The general objectives of the laboratory investigation have been fulfilled. But because of the cursory investigation of many of the problems, the results of this program should be considered of a preliminary nature. Drag coefficient versus time (or  $P_s$ ) for spheres exposed to clean shock waves are presented in Figures 7.9 through 7.13 and Figures 7.25 and 7.27; drag coefficients for spheres in steady wind-tunnel flow are presented in Figures 7.35, 7.43 and 7.46; and the comparison of shock-tube drag coefficients and wind-tunnel drag coefficients is made in Figure 7.48.

Although it was concluded that the wind-tunnel drag coefficients were comparable to the shock-tube drag coefficients, the time for establishment of steady drag in a shock wave appeared to vary from a very short time to about 75 transit times. Since 75 transit times represents a considerable duration when referred to a large structure (for a dome of 50-foot diameter, 75 transit times is about 3 seconds, much longer than the entire positive duration of Shot 12) and the loads during these 75 transit times are much higher than the steady-drag values, it is concluded that further laboratory effort is required to determine reliable limits of the transient drag phenomena.

### 8.2 RECOMMENDATIONS

Before embarking on an extensive course of laboratory investigations in the future, it is recommended that the laboratory tools be improved considerably. The force-gage performance can be improved through redesign, either to seal the shell completely or take pressure-time readings inside the shell or to admit  $P_s$  inside the shell. Further gage development is suggested along the lines of better damping and higher-frequency response.

The fields of investigation that appear to be of most immediate promise include: (1) effects on  $C_D$  of wave shape and duration, such as longer flat-topped shocks, varying rates of decay of peaked shocks, and shocks with slow rise times; (2) turbulence, either generated by wire meshes for its effect on  $C_D$ , or measured quantitatively, or both; (3) effects of dust on  $q$  gages and force gage models; (4) measurement of the diffraction loading on three-dimensional models to define with greater precision the effects of the transition from the diffraction phase to the drag phase; and (5) effects of target geometry.

It is expected that the results of any future field programs involving force measurements on drag targets will be of considerable scientific and military interest, provided the laboratory investigations are completed beforehand to provide a framework of basic information so that the isolated field measurements may be properly assessed.

## Appendix A

# PRESSURE-TIME MEASUREMENTS ON 3.2t STRUCTURE

### A.1 TEST CONDITIONS

The Naval Ordnance Laboratory, as participant in Program 3 (Shot 12 only), reinstrumented with pressure gages a steel-reinforced concrete structure used previously on the UPSHOT-KNOTHOLE Operation. This structure, a 6-by-6-by-12-foot cubicle, located 2,200 feet from ground zero in the desert area (and approximately 200 feet south of the blast line) was identified as 3.1t during Operation Upshot-Knothole and as 3.2t during Operation Teapot.

Twenty-four pressure-time gages were distributed flush with the front, top, side, and rear surfaces of the structure, as shown in Figure A.1. The instrumentation system used to obtain the measurements was the same as was used during Upshot-Knothole (Reference 29) and the recording and playback equipment is described in detail in References 29 and 39 and in general in Part 1 of this report. The NOL-modified Wiancko pressure gage was used again for the transducer unit. The characteristics of this gage are described in detail in Reference 40. Briefly, these characteristics can be summarized as follows:

1. Frequency Response. In normal, torsional movement (damped), approximately 900 cps; in extraneous cantilever motion, 250 to 800 cps.
2. Damping. Approximately 0.2 to 0.4 of critical to limit ringing and minimize creep; gage ringing lasts for approximately 4 msec.
3. Acceleration Sensitivity. A 10-g impact produces a 1-psi signal on a 20-psi gage, caused by cantilever action of the twisted-tube sensing element.
4. Temperature Sensitivity. Thermal energy entering directly into the twisted tube causes torsional movement of the tube and thus electrical signal. Where required, small aluminum shields are placed in front of the gage to prevent direct entry of thermal rays.
5. Static and Dynamic Calibration Accuracy. Within  $\pm 2$  percent of the applied pressure. The overall instrumentation has the characteristics of an underdamped, nonlinear system with the gage being the limiting unit. With the gages operating near nominal range, maximum error in pressure determination is no more than 5 percent. Time resolution of the system is approximately 0.2 msec and timing errors 0.05 percent.

The geometric relationship between the burst point and the eight gages on the front face of the structure was such as to permit direct thermal radiation to enter the Wiancko gage twisted-tube sensing elements. To prevent this direct entry of thermal rays, 2-by-2-inch aluminum-foil shields were placed 4 inches in front of those gages in

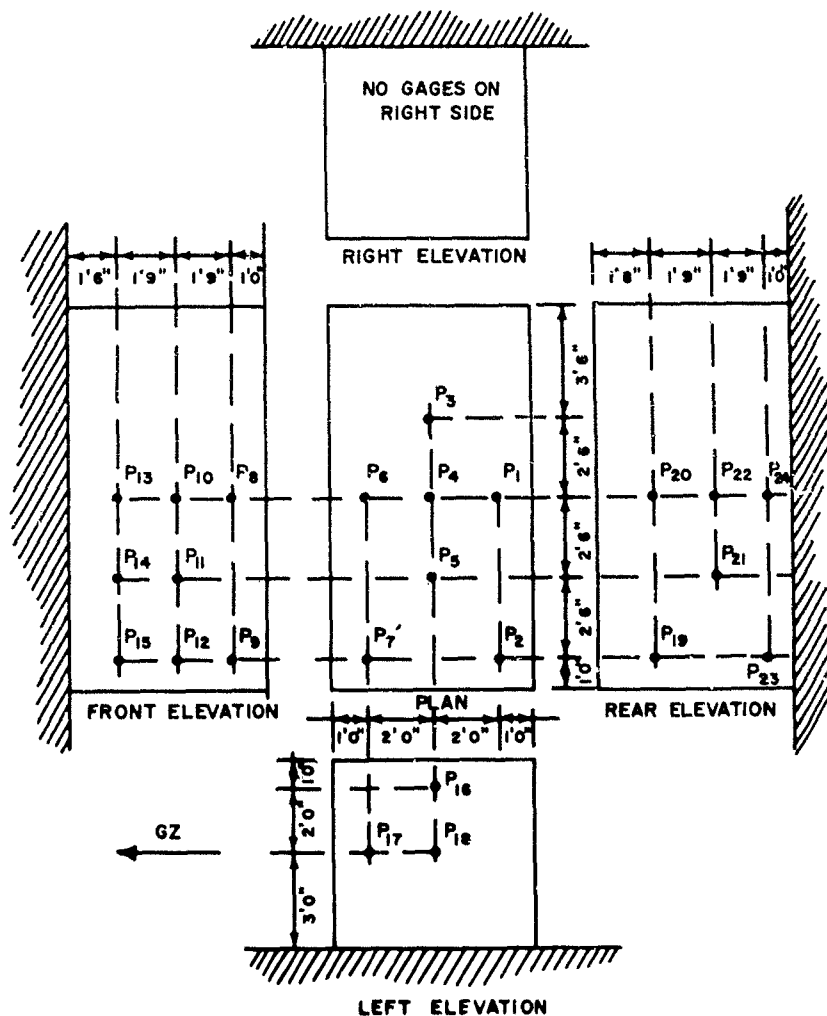


Figure A.1 Gage Locations on Structure 3.2t.

the line of sight between the burst point and the individual gages. The shields were so mounted and secured as to give minimum interference with the blast wave.

## A.2 RESULTS

The instrumentation functioned satisfactorily; all gage signals were recorded, and signal levels were near the rated range of the gages, so good reading accuracy was obtained. Unfortunately, six of the eight front-face gage records showed evidence of direct thermal

incidence on the gages; base-line shifts starting shortly after zero time occurred on these records. The high surface winds prevailing for hours between the time of positioning the aluminum shields and the time of the shot undoubtedly blew the majority of shields out of position. On these six records, by correcting for the base-line shifts, the details of wave shapes were readily and validly determined, although some error probably exists in the measurements of absolute magnitude.

A cursory comparison of these Teapot records with the records obtained on the same structure during Shot 10 of Upshot-Knothole showed similar wave shapes, even in details, for the various surfaces. Detailed analysis of the records was performed by Project 3.2. A preliminary set of pressure-time records (high-speed and low-speed playback), necessary static and dynamic calibration curves and instructions on record reading were turned over to Project 3.2 (the Armour Research Foundation on contract to the Wright Air Development Center).

CONFIDENTIAL

## Appendix B

# RESPONSE OF A DAMPED SINGLE - DEGREE SYSTEM TO AN IMPULSE FOLLOWED BY A STEP FUNCTION

Inductance force gages respond to diffraction loading as well as to drag loading, but they have natural frequencies too low to record properly the diffraction phase of the loading. Fortunately, for purposes of analysis, their frequencies are low enough that the diffraction period effectively constitutes an impulse; that is, the duration of loading is about one-quarter or less of the natural period of the gage (Reference 41). For example, the 3-inch gages have a diffraction phase lasting about 0.4 msec, whereas their natural periods ranged from about 1 1/2 msec to about 7 msec. The ratios of loading duration to natural periods therefore ranging from about 0.06 to 0.25. The following analysis shows the effect on a low-frequency system of a short-duration spike followed by a constant load, such as is represented in Figure B.1, with the following nomenclature:

- A Projected area of body in air stream
- $C_1$  Constant of integration
- $C_2$  Constant of integration
- $C_D$  Drag coefficient, defined as  $F/qA$
- F Force
- n Damping coefficient (ratio  $n/\omega$  = fraction of critical damping)
- $P_r$  Reflected shock overpressure
- $P_s$  Side-on overpressure
- $P_1$   $P_1^2 = \omega^2 - n^2$
- q Dynamic pressure =  $1/2 \rho u^2$
- t Time
- u Particle flow velocity in shock wave
- $V_0$  Initial velocity of model due to diffraction impulse
- y Deflection
- $\dot{y}$  Velocity
- $\ddot{y}_0$  Steady step-function acceleration, the idealized drag phase
- $\rho$  Air density
- $\omega$  Natural frequency of gage-model combination

For a damped system excited by the step function of amplitude  $\ddot{y}_0$ :

$$\frac{d^2 y}{dt^2} + 2n \frac{dy}{dt} + \omega^2 y = \ddot{y}_0 \quad (B.1)$$

$$y = \frac{\ddot{y}_0}{\omega^2} + e^{-nt} (C_1 \sin P_1 t + C_2 \cos P_1 t) \text{ where } P_1^2 = \omega^2 - n^2$$

$$\dot{y} = -ne^{-nt} (C_1 \sin P_1 t + C_2 \cos P_1 t) +$$

$$P_1 e^{-nt} (C_1 \cos P_1 t - C_2 \sin P_1 t)$$

At  $t = 0$ , the diffraction spike of vanishingly short duration (relative to the natural period,  $\frac{2\pi}{\omega}$ ) has the effect of a

Dirac pulse and may be represented as an initial velocity,  $V_0$ . Therefore, the initial conditions at  $t = 0$  may be stated as  $y = 0$  and  $\dot{y} = V_0$ ; whence

$$C_1 = \frac{1}{P_1} \{ V_0 - n \ddot{y}_0 / \omega^2 \}$$

$$C_2 = -\ddot{y}_0 / \omega^2$$

$$y = \frac{\ddot{y}_0}{\omega^2} + e^{-nt} \left\{ \frac{V_0 - n \ddot{y}_0 / \omega^2}{P_1} \sin P_1 t - \frac{\ddot{y}_0}{\omega^2} \cos P_1 t \right\}$$

$$\omega^2 \frac{y}{\ddot{y}_0} = 1 + e^{-nt} \left[ \left( \frac{\omega^2 V_0}{P_1 \ddot{y}_0} - \frac{n}{P_1} \right) \sin P_1 t - \cos P_1 t \right] \quad (B.2)$$

In order to see the shape of this response curve, let us estimate a value of  $\frac{\omega^2 V_0}{\ddot{y}_0}$ .

Assume  $P_g = 20$  psi, and  $C_D = 0.4$ . Calculated  $P_r$  and  $q$  are 59.5 psi and 8.13 psi, respectively. The impulse delivered to a 3-inch gage in two transit times (0.00044 sec) by a pulse of triangular shape would be

$$\frac{P_r A}{2} (0.00044) = \frac{59.5 \times 7.07}{2} (0.00044) = 0.093 \text{ lb-sec.}$$

Equating impulse and momentum for a gage with moving parts weighing 1 pound:

$$V_0 = \frac{0.093}{1/32.2} = 3.0 \text{ ft/sec.}$$

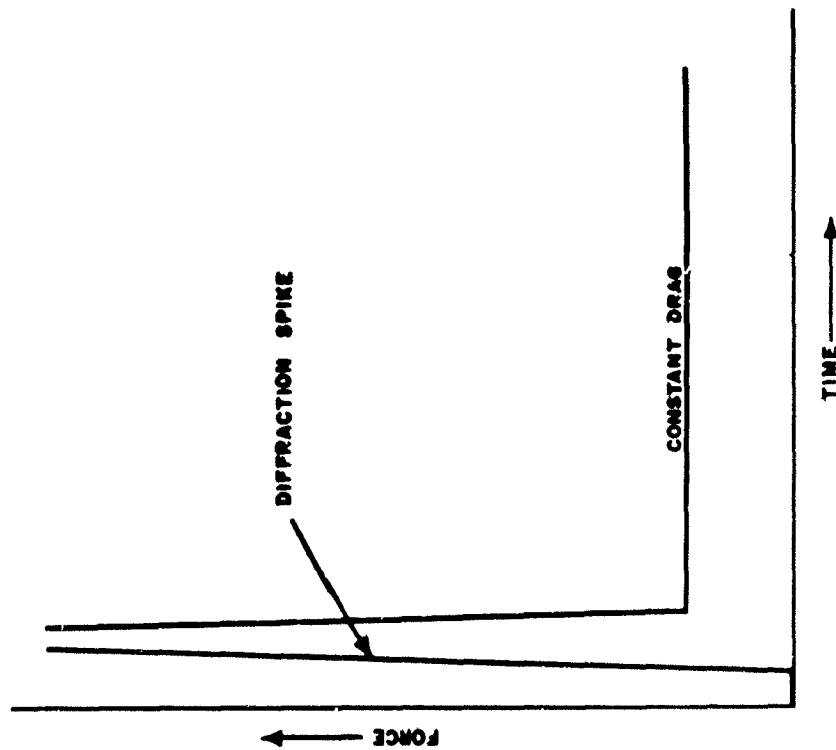


Figure B.1 Idealized Loading History for Low-Frequency Structure.

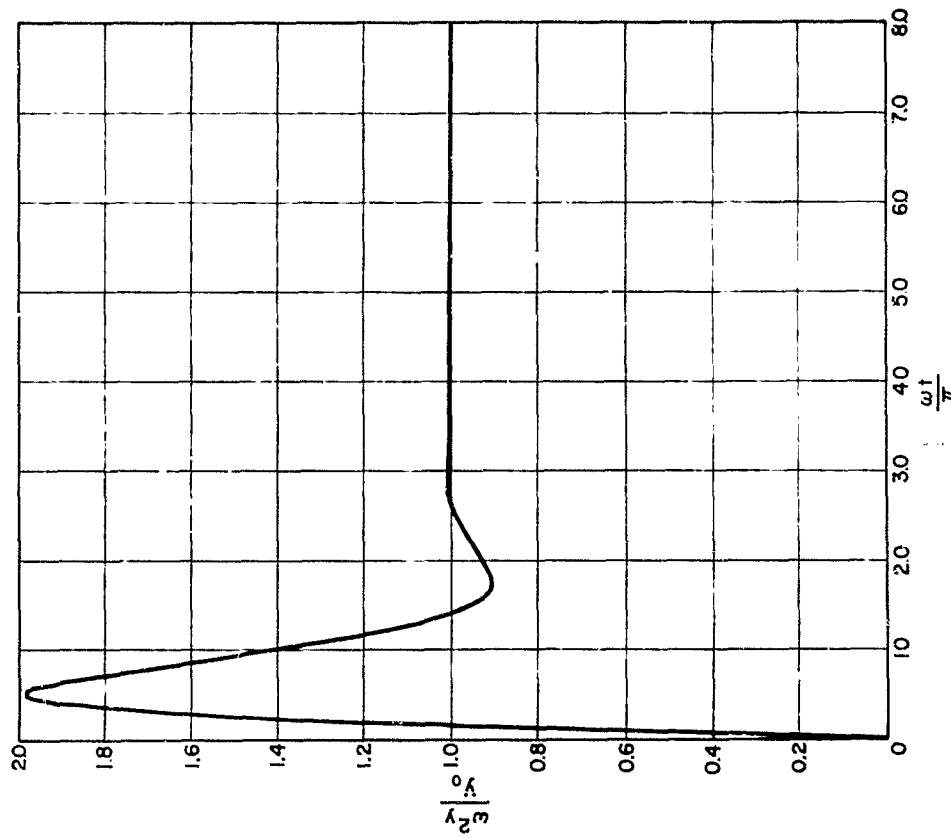


Figure B.2 Damped Single-Degree System Loaded by an Impulse and a Step Function ( $n/\omega = 0.6$ ,  $V_0/\beta_0 = 3$ ).



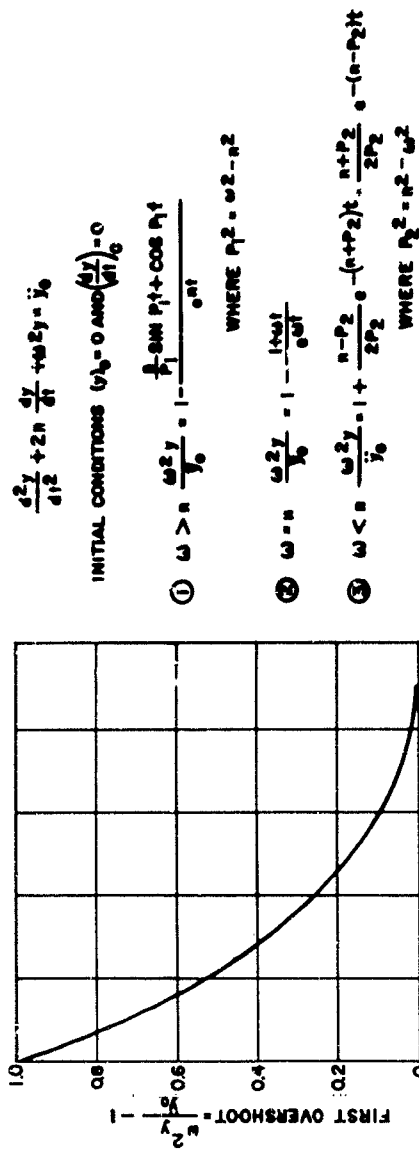
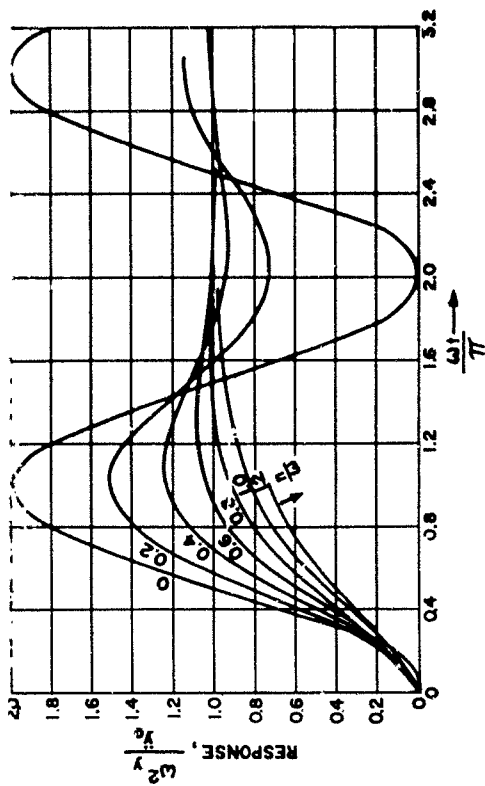


Figure B.3 Response of a Damped Single-Degree-of-Freedom System to a Step Function.

$$\frac{d^2y}{dt^2} + 2\eta \frac{dy}{dt} + \omega^2 y = \ddot{y}_0$$

INITIAL CONDITIONS  $(y)_0 = 0$  AND  $\left(\frac{dy}{dt}\right)_0 = V_0$

$$\frac{\omega^2 y}{V_0} = 1 + e^{-\eta t} \left[ \frac{\omega}{P_1} \left( \frac{\omega V_0}{y_0} - \frac{\eta}{\omega} \right) \sin P_1 t - \cos P_1 t \right]$$

$$\text{WHERE } P_1^2 = \omega^2 - \eta^2$$

RESPONSE FOR  $\frac{\eta}{\omega} = 0.6$ ,  $\frac{\omega V_0}{y_0} = 3$

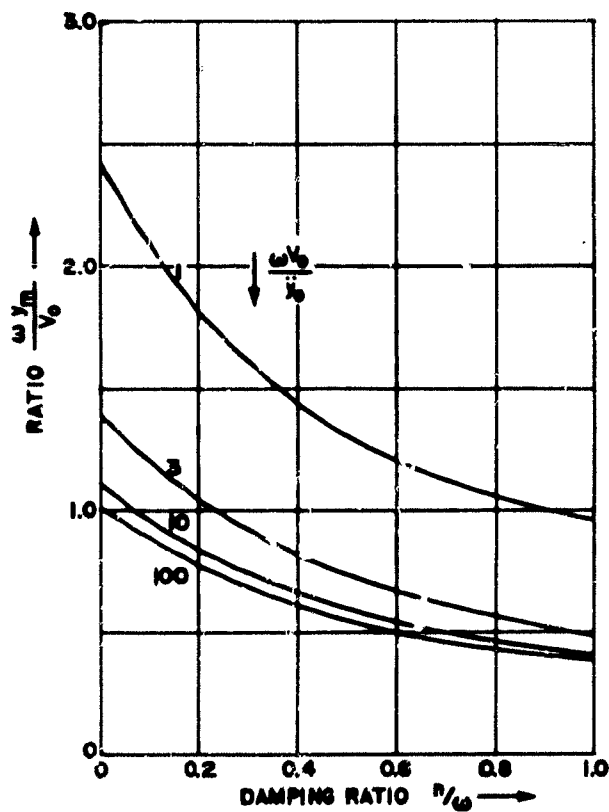
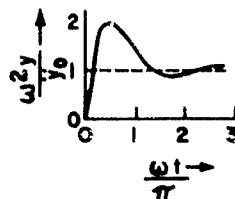


Figure B.4 Maximum Amplitude of a Damped Single-Degree System Loaded by an Impulse and a Step Function.

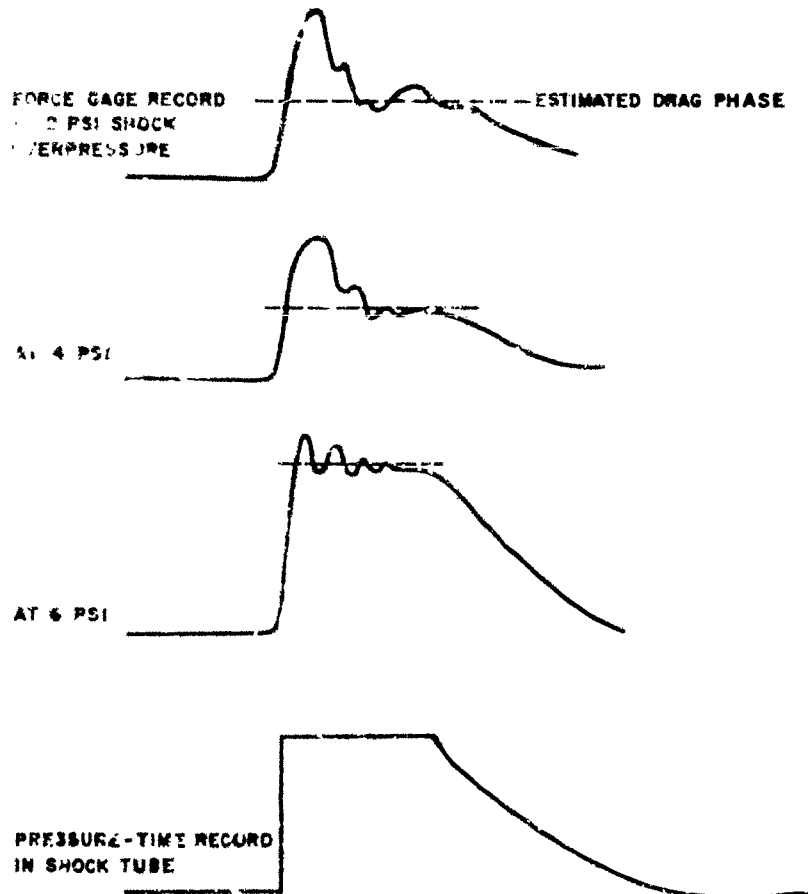


Figure B.5 Effect of Shock Overpressure on Relative Amplitude of Diffraction Spike at Drag Flat-Top.

Also,

$$\ddot{y}_0 = \frac{q_{C,A}}{1/32.2} = \frac{(8.13)(0.4)(7.07)}{1/32.2} = 741 \text{ ft/sec}^2$$

Therefore, if the natural frequency of the gage is 100 cps:

$$\frac{\omega \dot{y}_0}{\ddot{y}_0} = \frac{(2\pi \times 100)(3.0)}{741} = 2.5$$

Selecting 60 percent of critical damping,  $\frac{n}{\omega} = 0.6$ , and  $\frac{\omega \dot{y}_0}{\ddot{y}_0} = 3$ , one may plot  $\frac{\omega^2 y}{\ddot{y}_0}$  of Equation B.2 versus  $\frac{\omega t}{\pi}$ .

Figure B.2 presents this response curve. Figure B.3 indicates the effect of the suddenly applied drag load, without the diffraction spike. One may note by comparison with Figure B.2 that only about half the amplitude is attained for  $n/\omega = 0.6$  without the diffraction phase.

Figure B.4 shows how the maximum amplitude attained by the gage varies with  $n/\omega$  and  $\frac{\omega V_0}{\gamma}$ . The higher the gage frequency (up to the point that the gage frequency is high enough to "read" the diffraction spike, in which case the foregoing analysis is invalid), the higher is the diffraction response. This is also true of the recording system, and explains why the field records of Figures 3.8 through 3.14 show no diffraction spikes. (When these tape recordings are played back on higher frequency playback equipment, the spikes do show up; similar to the shock-tube records, which were obtained directly through oscilloscope pictures.)

Further qualitative verification of the above theoretical considerations is obtained by the series of shock-tube records of Figure B.5, which show the effect of increase of shock overpressure on relative amplitude of spike and flat top. Note that the spike is much higher than the flat top at lower pressures, decreasing relatively at higher pressures. This is due to the fact that  $P_r/q$  approaches infinity at zero overpressure and decreases with pressure; and the diffraction spike (or  $V_0$ ) depends on  $P_r$ , whereas the flat top (or  $\dot{\gamma}_0$ ) depends on  $q$ .

## REFERENCES

1. T. P. Tung, N. M. Newmark; A Review of Numerical Integration Methods for Dynamic Response of Structures; U. of Ill., Civil Eng. Studies No. 69, March 1954.

2. N. B. Brooks, N. M. Newmark; Development of Procedures for Rapid Computation of Dynamic Structural Response; U. of Ill., Struct. Res. Series No. 83, 1 July 1954.

3. W. J. Francy, N. M. Newmark; A Study of Blast Loading Transmitted to Building Frames; U. of Ill. No. 89, December 1954.

4. B. L. Tucker; Transient Drag and American Machine and Foundry Project MR 1013; Sandia Corp. Tech. Memo. 260-55-51.

5. N. M. Newmark; Effect of Long Positive Phase Blast Waves on Drag and Diffraction Type Targets; AFSWP-494, 21 August 1953.

6. F. G. Friedlander; The Diffraction of Sound Pulses; Proc. Roy. Soc. (A) Vol. 186, No. 1066, Pages 322 to 367, 24 September 1946.

7. L. Ting, H. F. Ludloff; Aerodynamics of Blasts; J. Aerc. Sci., Vol. 19, No. 5, Page 317, May 1952.

8. L. Ting; Diffraction and Reflection of Weak Shocks by Structures; J. Math. Phys., Vol. 32, No. 2-3, July-October 1953.

9. J. B. Keller; Multiple Shock Reflection in Corners; J. Ap. Phys., Vol. 25, No. 5, May 1954.

10. W. Bleakney; The Diffraction of Shock Waves Around Obstacles and Transient Loading of Structures; Princeton U., Tech. Rept. II-3, March 16, 1950.

11. G. Uhlenbeck; Diffraction of Shock Waves Around Various Obstacles; U. of Mich., Eng. Res. Inst., Proj. M720-4, March 21, 1950.

12. D. R. White, D. K. Weimer, W. Bleakney; The Diffraction of Shock Waves Around Obstacles and the Resulting Transient Loading of Structures; Princeton U. Tech. Rept. II-6, August 1950.

13. D. E. Brickl, W. Bleakney; The Diffraction of a Shock Wave Over a Three-Dimensional Object; Princeton U. Tech. Report. II-14, April 1953.

14. G. P. Beachler; Records of Air Shock Loading on a Three Dimensional Model; BRL Tech. Note 342, AFSWP-767, January 1954.

15. G. A. Coulter; Shielding Effect of Walls; BRL Tech. Note 582, April 1952.
16. R. E. Duff; The Interaction of Plane Shock Waves and Rough Surfaces; J. Ap. Phys., Vol. 23, No. 12, December 1952.
17. D. E. Conant; The Effect of Surface Roughness on the Diffraction of a Shock Wave Around Two-Dimensional Blocks; BRL Tech. Note 858, AFSWP-769, January 1954.
18. R. E. Duff, R. N. Hollyer; The Diffraction of Shock Waves Through Obstacles with Various Openings in their Front and Back Surfaces; U. of Mich., Eng. Res. Inst. Rept. 50-3, November 7, 1950.
19. M. L. Merritt; Some Tests of the Diffraction of Blast Waves; Sandia Corp., SC-1803 (TR), June 7, 1951.
20. J. Penzien; Experimental Investigation of the Blast Loading on an Idealized Structure; Sandia Corp., SC-2124(TR), December 7, 1951.
21. M. L. Merritt; Shielding from Blast Waves by Parallel Structures; Sandia Corp., AFSWP-224, October 28, 1952.
22. C. C. Hudson; Self-Shielding from Blast Waves by Structural Members; Sandia Corp., AFSWP-225, May 1953.
23. R. D. Jones; Blast Loading from a Scaled Explosion on a Scaled Greenhouse Structure, Sandia Corp.; AFSWP-227, July 1953.
24. M. L. Merritt; Effects of Surface Roughness on Blast Waves, Sandia Corp.; SC-1604(TR), October 30, 1950.
25. H. H. Bingham, D. K. Weimer, W. Griffith; The Cylinder and Semi-cylinder in Subsonic Flow; Princeton U., Dept. of Phys. Tech. Rept. II-13, July 1952.
26. J. R. Banister, R. J. Emrich; Preliminary Investigation of Dust Raised by Blast Waves; Sandia Corp., SC-3610(TR), January 3, 1955.
27. G. F. Carrier; The Transmission of Blast Through a Dust Filled Gas-Linearized Treatment; Part I - BRL Memo. Rept. No. 873, February 1955; Part II - BRL Memo. Rept. No. 872, February 1955.
28. J. R. Ballinger; Feasibility Study of Dynamic Net Force Sensors; Wind Tunnel Instrument Co., Inc., Project No. 76, February 1955.
29. Morris, et al; Air Blast Measurements; Operation Knothole, WT-710.
30. Morris, et al; Ground Acceleration Measurements; Operation Jangle, WT-388, June 1952.

31. J. R. Banister, C. D. Broyles; Preliminary Investigation of the Response of Pressure Gages to Dust Laden Air; Sandia Tech. Memo. 215-53-51, February 5, 1954.

32. A. May, W. R. Witt, Jr.; Free-Flight Determinations of the Drag Coefficients of Spheres; J. Aero. Sci., Vol. 20, No. 9, September 1953.

33. I. Langmuir, K. B. Blodgett; A Mathematical Investigation of Water Droplet Trajectories; Wright Field AAF Tech. Rept. 5416, 19 February 1946.

34. J. L. Dussourd; A Theoretical and Experimental Investigation of a Deceleration Probe for Measurement of Several Properties of a Droplet-Laden Air Stream; Aerothermopressor Proj., M. E. Dept., M.I.T., October 1954.

35. J. L. Dussourd, A. H. Shapiro; A Deceleration Probe for Measuring Stagnation Pressure and Velocity of a Particle-Laden Gas Stream; Aerothermopressor Proj., M. E. Dept., M.I.T., May 1955.

..... 36. G. K. Hartmann; The Force on Drag Targets in Dust Laden  
..... Blast; NOL TN-2647, 10 May 1954.

..... 37. Handbook of Chemistry and Physics; Thirtieth Edition, 1947,  
..... Page 1736.

..... 38. Morris. Petes; Pressure Measurements for Various Projects  
..... of Program 3; Operation Knothole, WT-739, 1954.

..... 39. Petes, Little, Dossey; Evaluation of Wiancko and Vibrotron  
..... Gages and Development of New Circuitry for Atomic Blast Measurements;  
..... WT-784, March-June, 1953.

..... 40. J. M. Frankland; Effects of Impact on Simple Elastic  
..... Structures; DTMB Rept. 481, April 1942.

## DISTRIBUTION

*Military Distribution Categories 5-21 and 5-60*

### ARMY ACTIVITIES

- 1 Asst. Dep. Chief of Staff for Military Operations, D/A, Washington 25, D.C. ATTN: Asst. Executive (RASM)
- 2 Chief of Research and Development, D/A, Washington 25, D.C. ATTN: Atomic Division
- 3 Chief of Ordnance, D/A, Washington 25, D.C. ATTN: CORDIX-AR
- 4 Chief Signal Officer, D/A, P&O Division, Washington 25, D.C. ATTN: SIGRD-8
- 5 The Surgeon General, D/A, Washington 25, D.C. ATTN: MEDNE
- 6-7 Chief Chemical Officer, D/A, Washington 25, D.C.
- 8 The Quartermaster General, D/A, Washington 25, D.C. ATTN: Research and Development
- 9-11 Chief of Engineers, D/A, Washington 25, D.C. ATTN: ENGB
- 12 Chief of Transportation, Military Planning and Intelligence Div., Washington 25, D.C.
- 13-15 Commanding General, Headquarters, U. S. Continental Army Command, Ft. Monroe, Va.
- 16 President, Board #1, Headquarters, Continental Army Command, Ft. Sill, Okla.
- 17 President, Board #2, Headquarters, Continental Army Command, Ft. Knox, Ky.
- 18 President, Board #3, Headquarters, Continental Army Command, Ft. Benning, Ga.
- 19 President, Board #4, Headquarters, Continental Army Command, Ft. Bliss, Tex.
- 20 Commanding General, U.S. Army Caribbean, Ft. Amador, C.Z. ATTN: Cal. Off.
- 21 Commander-in-Chief, European Command, APO 126, New York, N.Y.
- 22-23 Commanding General, U.S. Army Europe, APO 403, New York, N.Y. ATTN: OPOT Div., Combat Dev. Br.
- 24-25 Commandant, Command and General Staff College, Ft. Leavenworth, Kan. ATTN: ALLIS(AS)
- 26 Commandant, The Artillery and Missile School, Ft. Sill, Okla.
- 27 Secretary, The U.S. Army Air Defense School, Ft. Bliss, Texas. ATTN: Maj. Ergun V. Roth, Dept. of Tactics and Combined Arms
- 28 Commanding General, Army Medical Service School, Brooke Army Medical Center, Ft. Sam Houston, Tex.
- 29 Director, Special Weapons Development Office, Headquarters, COMARC, Ft. Bliss, Tex. ATTN: Capt. T. E. Skinner
- 30 Commandant, Walter Reed Army Institute of Research, Walter Reed Army Medical Center, Washington 25, D. C.
- 31 Superintendent, U.S. Military Academy, West Point, N. Y. ATTN: Prof. of Ordnance
- 32 Commandant, Chemical Corps School, Chemical Corps Training Command, Ft. McClellan, Ala.
- 33 Commanding General, U.S. Army Chemical Corps, Research and Development Command, Washington, D.C.
- 34-35 Commanding General, Aberdeen Proving Grounds, Md. ATTN: Director, Ballistics Research Laboratory
- 36 Commanding General, The Engineer Center, Ft. Belvoir, Va. ATTN: Asst. Commandant, Engineer School
- 37 Commanding Officer, Engineer Research and Development Laboratory, Ft. Belvoir, Va. ATTN: Chief, Technical Intelligence Branch
- 38 Commanding Officer, Picatinny Arsenal, Dover, N.J. ATTN: COMBATEX
- 39 Commanding Officer, Army Medical Research Laboratory, Ft. Knox, Ky.
- 40-41 Commanding Officer, Chemical Warfare Laboratories, Army Chemical Center, Md. ATTN: Tech. Library
- 42 Commanding Officer, Transportation R&D Station, Ft. Belvoir, Va.

- 43 Director, Technical Documents Center, Evans Signal Laboratory, Belmar, N.J.
- 44 Director, Waterways Experiment Station, P.O. Box 641, Vicksburg, Miss. ATTN: Library
- 45 Director, Armed Forces Institute of Pathology, Walter Reed Army Medical Center, 6800 16th Street, N.W., Washington 25, D.C.
- 46 Operations Research Office, Johns Hopkins University, 6935 Arlington Rd., Bethesda 14, Md.
- 47-48 Commanding General, Quartermaster Research and Development, Command, Quartermaster Research and Development Center, Natick, Mass. ATTN: CBH Liaison Officer
- 49 Commanding Officer, Diamond Ordnance Fuze Laboratories, Washington 25, D.C., ATTN: Coordinator, Atomic Weapons Effects Tests
- 50 Commanding General, Quartermaster Research and Engineering Command, U.S. Army, Natick, Mass.
- 51-55 Technical Information Service Extension, Oak Ridge, Tenn.

### NAVY ACTIVITIES

- 56-57 Chief of Naval Operations, D/N, Washington 25, D. C. ATTN: OP-36
- 58 Chief of Naval Operations, D/N, Washington 25, D.C. ATTN: OP-03EG
- 59 Chief, Bureau of Medicine and Surgery, D/N, Washington 25, D.C. ATTN: Special Weapons Defense Div.
- 60 Chief, Bureau of Ordnance, D/N, Washington 25, D.C.
- 61-62 Chief, Bureau of Ships, D/N, Washington 25, D.C. ATTN: Code 348
- 63 Chief, Bureau of Yards and Docks, D/N, Washington 25, D.C. ATTN: D-440
- 64 Chief, Bureau of Supplies and Accounts, D/N, Washington 25, D.C.
- 65-66 Chief, Bureau of Aeronautics, D/N, Washington 25, D.C.
- 67 Chief of Naval Research, Department of the Navy, Washington 25, D.C. ATTN: Code 811
- 68 Commander-in-Chief, U.S. Atlantic Fleet, U.S. Naval Base, Norfolk 11, Va.
- 69-72 Commandant, U.S. Marine Corps, Washington 25, D.C. ATTN: Code A03E
- 73 President, U.S. Naval War College, Newport, R.I.
- 74 Superintendent, U.S. Naval Postgraduate School, Monterey, Calif.
- 75 Commanding Officer, U.S. Naval Schools Command, U.S. Naval Station, Treasure Island, San Francisco, Calif.
- 76 Commanding Officer, U.S. Fleet Training Center, Naval Base, Norfolk 11, Va. ATTN: Special Weapons School
- 77-78 Special Weapons Unit, Pacific, U.S. Naval Air Station, North Island, San Diego 35, Calif.
- 79 Commanding Officer, Air Development Squadron 5, VX-5, China Lake, Calif.
- 80 Commanding Officer, U.S. Naval Damage Control Training Center, Naval Base, Philadelphia, Pa. ATTN: ABC Defense Course
- 81 Commander, U.S. Naval Ordnance Laboratory, Silver Spring 19, Md. ATTN: EE
- 82 Commander, U.S. Naval Ordnance Laboratory, Silver Spring 19, Md. ATTN: EH
- 83 Commander, U.S. Naval Ordnance Laboratory, Silver Spring 19, Md. ATTN: P
- 84 Commander, U.S. Naval Ordnance Test Station, Inyokern, China Lake, Calif.
- 85 Officer-in-Charge, U.S. Naval Civil Engineering Res. and Evaluation Lab., U.S. Naval Construction Battalion Center, Fort Belvoir, Calif. ATTN: Co. 753
- 86 Commanding Officer, U.S. Naval Medical Research Inst., National Naval Medical Center, Bethesda 14, Md.



~~CONFIDENTIAL~~

- 87 Director, Naval Air Experimental Station, Air  
Material Center, U.S. Naval Base, Philadelphia,  
Penn.  
88-92 Chief, Bureau of Aeronautics, D/N, Washington 25, D.C.  
ATTN: AER-AD-41/20  
93 Commanding Officer, Naval Air Special Weapons Facility,  
Kirtland AFB, Albuquerque, N. Mex.  
94 Director, U.S. Naval Research Laboratory, Washington  
25, D.C. ATTN: Mrs. Katherine H. Cass  
95 Commanding Officer and Director, U.S. Navy Electronics  
Laboratory, San Diego 50, Calif. ATTN: Code 4224  
96-97 Commanding Officer, U.S. Naval Radiological Defense  
Laboratory, San Francisco, Calif. ATTN: Technical  
Information Division  
98-99 Commanding Officer and Director, David W. Taylor Model  
Basin, Washington 7, D.C. ATTN: Library  
100 Commander, U.S. Naval Air Development Center, Johna-  
ville, Pa.  
101 Commander-in-Chief Pacific, Pearl Harbor, TH  
102 Commander, Norfolk Naval Shipyard, Portsmouth 8, Va.  
ATTN: Code 270  
103 Chief, Bureau of Ordnance, D/N, Washington 25, D.C.,  
ATTN: SP  
104-110 Technical Information Service Extension, Oak Ridge, Tenn.  
(Surplus)

AIR FORCE ACTIVITIES

- ..... 111 Asst. for Atomic Energy Headquarters, USAF, Washing-  
..... ton 25, D.C. ATTN: DCS/O  
..... 112 Director of Operations, Headquarters, USAF, Washington  
..... 25, D.C. ATTN: Operations Analysis  
..... 113 Director of Plans, Headquarters, USAF, Washington 25,  
..... D.C. ATTN: War Plans Div.  
..... 114 Director of Research and Development, DCS/D, Head-  
..... quarters, USAF, Washington 25, D.C. ATTN: Combat  
..... Components Div.  
..... 115-116 Director of Intelligence, Headquarters, USAF, Washing-  
..... ton 25, D.C. ATTN: AFON-IR2  
..... 117 The Surgeon General, Headquarters, USAF, Washington 25,  
..... D.C. ATTN: Bio. Def. Br., Pre. Med. Div.  
..... 118 Asst. Chief of Staff, Intelligence, Headquarters, U.S.  
..... Air Forces-Europe, APO 633, New York, N.Y. ATTN:  
..... Directorate of Air Targets  
..... 119 Commander, 49th Reconnaissance Technical Squadron  
..... (Augmented), APO 633, New York, N.Y.  
..... 120 Commander-in-Chief, Pacific Air Forces, APO 953, San  
..... Francisco, Calif. ATTN: PFCIE-MB, Base Recovery  
..... 121 Commander-in-Chief, Strategic Air Command, Offutt AFB,  
..... Omaha, Nebraska. ATTN: OAMS  
..... 122 Commander, Tactical Air Command, Langley AFB, Va.  
..... ATTN: Documents Security Branch  
..... 123 Commander, Air Defense Command, Nt AFB, Colo.  
124-125 Research Directorate, Headquarters, Air Force Special  
Weapons Center, Kirtland AFB, New Mexico. ATTN: Blast  
Effects Res.  
126-128 Assistant for Operations Analysis, DCS/Operations,  
ATTN: Missile Survival Study Group (Mr. Tuttle),  
Headquarters, USAF, Washington 25, D.C.  
129 Director of Installations, DCS/O, Headquarters, USAF,  
Washington 25, D.C. ATTN: AFON-E  
130 Commander, Air Research and Development Command, Andrews  
AFB, Washington 25, D.C. ATTN: RDEN  
131 Commander, Air Proving Ground Command, Eglin AFB, Fla.  
ATTN: Adj./Tech. Report Branch  
132-133 Director, Air University Library, Maxwell AFB, Ala.  
134-139 Commander, Air Training Command, Randolph AFB, Tex.  
140-141 Commandant, Air Force School of Aviation Medicine,  
Randolph AFB, Tex.

- 142-147 Commander, Wright Air Development Center, Wri-  
Patterson AFB, Dayton, Ohio. ATTN: WCOCI  
148-149 Commander, Air Force Cambridge Research Center  
Hanscom Field, Bedford, Mass. ATTN: CRQST-  
150-152 Commander, Air Force Special Weapons Center, 1  
AFB, N. Mex. ATTN: Library  
153 Commander, Lowry AFB, Denver, Colo. ATTN: Depo  
of Special Weapons Training  
154 Commander, 1009th Special Weapons Squadron, B  
quarters, USAF, Washington 25, D.C.  
155-156 The RAND Corporation, 1700 Main Street, Santa  
Calif. ATTN: Nuclear Energy Division  
157 Commander, Second Air Force, Barksdale AFB, La  
Operations Analysis Office  
158 Commander, Eighth Air Force, Westover AFB, Ma-  
Operations Analysis Office  
159 Commander, Fifteenth Air Force, March AFB, Ca  
ATTN: Operations Analysis Office  
160 Commander, Western Development Div. (ARDE), P  
Ingwood, Calif. ATTN: WDMIT, R. G. Weitz  
161-165 Technical Information Service Extension, Oak  
Tenn. (Surplus)

OTHER DEPARTMENT OF DEFENSE ACTIVITIES

- 166 Asst. Secretary of Defense, Research and Engi-  
D/D, Washington 25, D.C. ATTN: Tech. Library  
167 U.S. Documents Officer, Office of the U.S. in  
Military Representative, SBAIE, APO 55, New  
N.Y.  
168 Director, Weapons Systems Evaluation Group,  
2E1006, Pentagon, Washington 25, D.C.  
169 Chairman, Armed Services Explosives Safety Bo-  
Building T-7, Gravelly Point, Washington 25  
170 Commandant, Armed Forces Staff College, Nor-  
Va. ATTN: Secretary  
171 Commander, Field Command, Armed Forces Specia-  
Weapons Project, PO Box 5100, Albuquerque.  
172 Commander, Field Command, Armed Forces Specia-  
Weapons Project, PO Box 5100, Albuquerque,  
ATTN: Technical Training Group  
173-177 Commander, Field Command, Armed Forces Specia-  
Weapons Project, P.O. Box 5100, Albuquerque  
ATTN: Deputy Chief of Staff, Weapons Effect  
178-188 Chief, Armed Forces Special Weapons Project,  
25, D.C. ATTN: Documents Library Branch  
189 National Advisory Committee for Aeronautics,  
N.W., Washington 25, D.C. ATTN: R. V. Rhoads  
190-194 Technical Information Service Extension, Oak  
(Surplus)

ATOMIC ENERGY COMMISSION ACTIVITIES

- 195-197 U.S. Atomic Energy Commission, Classified To  
Library, Washington 25, D.C. ATTN: Mrs. J.  
(For DMA)  
198-199 Los Alamos Scientific Laboratory, Report Lib  
Box 1663, Los Alamos, N. Mex. ATTN: Helen  
200-204 Sandia Corporation, Classified Document Divi-  
Sandia Base, Albuquerque, N. Mex. ATTN: H.  
Smyth, Jr.  
205-207 University of California Radiation Laborato-  
208, Livermore, Calif. ATTN: Gladys  
208 Weapon Data Section, Technical Information  
tension, Oak Ridge, Tenn.  
209-220 Technical Information Service Extension, Oak  
(Surplus)

Best Available Copy

~~CONFIDENTIAL~~